

Absolute Magnetometry with ^3He : Cross Calibration with Protons in Water

by

Midhat Farooq

A dissertation submitted in partial fulfillment
of the requirements for the degree of
Doctor of Philosophy
(Physics)
in the University of Michigan
2019

Doctoral Committee:

Professor Timothy Chupp, Chair
Professor Dante Amidei
Professor Dave Kawall, University of Massachusetts
Professor Sarah Keane
Professor Scott Swanson

Midhat Farooq

midhatf@umich.edu

ORCID iD: 0000-0002-7629-205X

©Midhat Farooq 2019

*Dedicated to all women of color in STEM -
those who worked hard to pave the way,
those who tirelessly persist today,
and the bright minds of the future.*

Acknowledgments

I would like to thank my advisor, Tim Chupp, for providing the guidance and mentorship I needed to succeed and for his immense support of my extracurricular activities. I also want to thank my fellow group members, Natasha Sachdeva and Alec Tewsley-Booth, for being willing to help with experimental work and also for greatly contributing to my understanding of physics. I am grateful to my Argonne colleagues, Joe Grange, Ran Hong and especially Peter Winter, for welcoming me into their group and making it so easy to conduct research away from my home institution. David Flay and Dave Kawall have also been of great help throughout my time at Argonne, providing much needed guidance. I want to thank Jim Tice, Ken Wood, and Frank Skrzecz for always being willing to machine parts, Tim Cundiff and Gary Drake for teaching me all about electronics, and Matt Okunawo and Duane Lute for 3D printing the many pieces I requested. I want to acknowledge the physics staff who made the department feel like home, including Paul Thurmond, Joe Sheldon, Chris Bolang, Kristyn Sonnenberg, Kayla Keller, Elise Bodei, Lauren Segall, Grace Johnson, Steve Roper, Carol Rabuck, and especially Chrissy Zigulis, who gave me strength, confidence, and love. Friends in the community that I cannot imagine going through graduate school without are Aaron Ross, Angela Germaine, Cristina Schlesier, Ben Lawson, Anthony Charles, Alex and Evangeline Burgers, Cameron Nelson, and Jess Cote. I want to especially thank Veronica Policht and Natasha Sachdeva for being my family and the support I didn't know I needed. Everything I have achieved in life is a direct result of my mother's endless, selfless love and I want to thank both of my parents for always encouraging me to follow my passion. Lastly, I want to thank my sister Iqra and my partner Joe for their undeterred love and support even when I make it hard for them. Without you two in my life, any success would be meaningless.

Funding acknowledgment

This work was supported by NSF grants PHY-150602 and PHY-1812314 and the DOE SCGSR program.

Table of Contents

Dedication	ii
Acknowledgments	iii
List of Tables	vi
List of Figures	vii
List of Appendices	xi
Abstract	xii
Chapter 1: Introduction	1
Chapter 2: Background and Motivation	3
2.1 Muon g-2: Theory and Experiment	3
2.2 Magnetic Field Calibration and the ^3He Cross Check	8
Chapter 3: Theory: MEOP and NMR	13
3.1 Need for Hyperpolarization of ^3He	13
3.2 Metastability Exchange Optical Pumping	14
3.3 NMR: Nuclear Magnetic Resonance	20
Chapter 4: Low Field MEOP and NMR Studies	26
4.1 ^3He Sample Cells: Making, Cleaning, and Filling	26
4.2 Low-field MEOP: Experimental Setup	28
4.3 Experimental Apparatus and Electronics for NMR	36
4.4 Low Field NMR signal and studies	41

Chapter 5: High Field MEOP and NMR	46
5.1 Changes for High Field	46
5.2 NMR Studies with UW Electronics	57
5.3 NMR Studies with Umich Electronics	64
5.4 Umich Electronics for Proton NMR	74
Chapter 6: Absolute Measurement and Cross-calibration	75
6.1 Methods	75
6.2 Corrections Overview	83
6.3 BNL Corrections (Cylindrical Probe)	85
6.4 ^3He Corrections	90
6.5 Other Errors	99
6.6 Cross-Check and Error Propagation	101
6.7 Spherical Probe Cross Calibration	104
Chapter 7: Conclusion and Looking Forward	109
7.1 Summary	109
7.2 Suggestions for Future Improvements	110
7.3 Future Measurements Scope	112
Appendices	114
Bibliography	125

List of Tables

2.1	Standard model contributions and uncertainties to a_μ	4
2.2	List of experiments measuring a_μ and precision reached.	6
5.1	Laser voltage settings for ^3He absorption lines at 1.45 T.	49
6.1	Cylindrical BNL probe cross-calibration with ^3He probe: all corrections and uncertainties. The final error of 36 ppb results from adding the uncertainties in quadrature as described in Sec. 6.6 and is with respect to proton NMR frequency 61.7 MHz.	100
6.2	Spherical BNL probe cross-calibration with ^3He probe: all corrections and uncertainties. The final error of 37 ppb results from adding the uncertainties in quadrature as described in Sec. 6.6 and is with respect to proton NMR frequency 61.7 MHz.	108
A.1	^3He data from cylindrical probe ABA cross-calibration (continued on next page).	117
A.2	Cylindrical BNL probe data for ABA cross-calibration with ^3He probe. . . .	119
A.3	^3He data from spherical probe ABBA cross-calibration.	120
A.4	Spherical BNL probe data for ABBA cross-calibration with ^3He probe. . . .	121

List of Figures

3.1	The three steps of low field MEOP. Figures adapted from [1]	16
3.2	Absorption lines of ^3He from 2^3S to 2^3P	16
3.3	Low (a) and high (b) field absorption lines for ^3He MEOP. The relative intensities are only estimates and all lines are with respect to the low field C_1 line at 0 GHz.	19
4.1	^3He cells before and after pull off from string.	27
4.2	Spectrum of cell as measured by spectrometer before and after freeze out. . .	28
4.3	Electronics for striking ^3He discharge.	29
4.4	Transformers made to strike ^3He discharge. N=80 turns for grey or white wire, N=2 turns for red wire.	29
4.5	Measured ^3He absorption spectrum at low field with labels for each absorption line from Figure 3.2.	31
4.6	MEOP experimental setup diagram (a) and picture (b) showing: ^3He cell and discharge coils, optics for optical pumping, polarimeter, and Helmholtz coils.	32
4.7	LCR Calibration Curve produced with 632 nm HeNe laser.	34
4.8	CW NMR studies at low field. The error bars are due to voltage measurements of polarization signal, uncertainty of cell pressure, and polarimeter calibration.	37
4.9	Electronics diagram for low field NMR.	38
4.10	^3He NMR FID signal at low field.	42
4.11	Longer $T_2^* = 300$ ms measured after switching to twinax cable.	43
4.12	FID signals after varying polarization time: 5 seconds to 120 seconds.	44
4.13	^3He NMR FID signal amplitude decay as a function of time between polarization with MEOP and NMR measurement giving a measure of the T_1 relaxation time.	44
4.14	^3He NMR FID signal for different sample cells.	45
4.15	^3He NMR FID signal with and without a chair near the setup.	45
5.1	High field superconducting MRI magnet at Argonne National Lab.	47

5.2	Wavelength tuning of Keopsys laser at different external voltages.	48
5.3	3D printed probe mount for high-field magnetometry.	50
5.4	Locations of optics, saddle coil, and ^3He cell in 3D printed probe mount. . .	51
5.5	Before and after removing aluminum box.	52
5.6	Saddle Coil design and photo.	55
5.7	Circuit for tuning and impedance matching saddle coil.	55
5.8	UW NMR electronics diagram.	58
5.9	Averaged FID signal on oscilloscope measured with UW electronics.	59
5.10	FID amplitude study for different laser absorption lines.	60
5.11	Pressure dependence study. Note that the vertical scales are different.	62
5.12	Electronics diagram for high field NMR including Umich Pulse Controller (dashed box).	66
5.13	Umich NMR Pulse Controller timing diagram.	66
5.14	Induced voltage on a pick up coil due to field created by the saddle coil and Umich NMR pulse controller as a function of input voltage.	67
5.15	High Field FID with (a) UW and (b) Umich electronics. Note that the data in (b) were taken after the switch to a copper shield and replacement of the magnetic cable.	68
5.16	Set of 200 frequency measurements to check clock stability. The error bars are determined from the standard deviation of the measurements.	69
5.17	Frequency stability data for two different days. The error bars are determined from 68% confidence interval of the extracted frequencies from the Matlab fit.	70
5.18	Frequency stability data for short and long timescales. The error bars are determined from 68% confidence interval of the extracted frequencies from the Matlab fit.	70
5.19	Pressure dependent study of FID signal with Umich pulse controller. Note that these studies were performed with the same electronic gain settings and the two plots have different x- and y-scales. The digital noise in (a) is due to the ~ 1 mV resolution of the data acquisition system.	71
5.20	Amplitude decay study for 2 and 10 Torr cells. The error bars are determined from 68% confidence interval of the amplitude value from the Matlab fit. Note that the decay does not follow the model due to additional time waited between each set of 5 measurements, i.e. the T_1 decay is on a longer time scale than decay due to each pulse.	72

5.21	Amplitude decay of FID signal, corrected for NMR pulse angle 8° , as a function of time. Extracted $T_1 = 134$ min. The error bars are determined from 68% confidence interval of the amplitude value from the Matlab fit.	73
6.1	The 3D printed holder (ivory) is mounted onto the 1D stage. Both the ^3He and BNL probes are fixed inside the holder with screws (circled). The x, y, and z directions are also indicated, with the magnetic field along the z-axis. .	76
6.2	Scans of ^3He probe along z-axis with the z-gradient set to three current values. The point of intersection is where $\Delta B = 0$, indicating that the probe active volume is uniquely positioned in the magnet.	80
6.3	Position repeatability along z-axis	80
6.4	Caption	81
6.5	BNL probe measurements before and after linear drift correction. The blue x's mark the ^3He measurement times. The error bars of 0.2 Hz (not shown in (b)) are from the fit model dependence of the frequencies, as described in section 6.5.1.	87
6.6	UW NMR probe mounted on 3D stage and inserted into cross-calibration setup with active volume in BNL nominal position.	88
6.7	Perturbation due to materials shown as a function of y-position. 0 mm marks the position of the BNL probe active volume and gives the $\delta^{\text{other-mat}}$ correction. The error bars are due to frequency changes resulting from position uncertainty.	89
6.8	Magnetization dependent study (a) and corrections (b)	92
6.9	Shorter T_2^* measured with stem parallel to field than when it is perpendicular.	94
6.10	$P_2(\cos\theta)$ fit of stem rotation about field in (a) x-z and (b) y-z planes. Note that the frequency offset in (a) between the two x-positions is due to magnet drift and accommodated for by the error bars. The error bars in both (a) and (b) are due to the frequency spread from the uncertainty in positioning the angle of the stem. The y-scales are different for the two figures.	95
6.11	Frequency spread when cell rotated with stem held fixed. The error bars in both (a) and (b) are due to the frequency spread from the uncertainty in positioning the angle of the stem. Note the y-scales are different for the two figures.	97
6.12	Apparatus for measuring ^3He materials perturbations.	98
7.1	Cross-calibration corrections schematics.	111

A.1	High field FID data (plotted in blue), fit (red), and residuals (green).	115
A.2	BNL data fit using two methods. Note that there is 60 Hz noise which causes the shape of the residuals. The fit amplitude does not change.	115

List of Appendices

Appendix A: NMR Fitting and Tabulated Cross-Calibration Data	114
Appendix B: Calculations	122
B.1 Magnetization Dependence of ^3He Frequencies	122
B.2 Magnetic Field Inside a Spherical Shell	123

Abstract

The muon magnetic moment anomaly a_μ is a measure of how the g-factor of the muon differs from the Dirac equation value of 2. Contributions to a_μ from the Standard Model (SM) arise from QED, strong, and electroweak interactions. The current 3.3σ discrepancy (~ 2.5 ppm) between the measured value of a_μ and the SM prediction could be a strong signal of BSM (beyond Standard Model) physics. This experimental value was measured at Brookhaven National Lab (BNL) with an uncertainty of 0.54 ppm. The measurement relied on absolute calibration of the magnetic field, which was measured with a system of proton NMR probes through a calibration chain referenced to an absolute probe with pure water. The uncertainty of the absolute calibration was quoted as 50 ppb due mainly to temperature dependent effects, perturbations due to materials, and the diamagnetic shielding factor. In this dissertation work, we cross-calibrate both BNL absolute calibration probes with an independent magnetometer based on hyperpolarized ^3He gas and perform pulsed NMR on the samples for frequency extraction, which is proportional to the magnetic field. Studies in both low fields (~ 0.003 Tesla) and high fields (1.45 Tesla) are reported. The cross-calibration campaign and corrections made to measure the field to the water and ^3He standards are described. The results of the cross-calibrations are 0.92 ± 2.23 Hz for the cylindrical BNL probe and 1.24 ± 2.29 Hz for the spherical probe with ~ 37 ppb uncertainty for each. The ~ 2.3 Hz error for both is dominated by uncertainties from systematic corrections and 37 ppb is with respect to proton NMR frequency in 1.45 T.

Chapter 1

Introduction

The goal of high energy physics is to explain the fundamental processes that underlie the macroscopic phenomena that we observe all around us every day. The Standard Model of particle physics is the most rigorous as well as experimentally validated theory that has been successful at nearly achieving this goal. However, the Standard Model remains incomplete. General Relativity, the widely accepted theory of gravity, is inconsistent with the Standard Model. The model also does not account for 95% of the universe which is made of dark matter and dark energy, two phenomena scientists are still attempting to understand. And lastly, the Standard Model does not have a mechanism for explaining the matter-antimatter asymmetry, i.e. why the universe mostly consists of matter.

As the theory lacks the information needed to extend the model, any new discoveries must come from experiments. One example of a fundamental parameter of nature which probes beyond Standard Model physics is a property of particles known as the magnetic moment anomaly, which arises from quantum interactions not predicted by classical physics. Historically, the anomaly value was predicted to be 0. However, in 1933, the proton anomaly was experimentally measured to be nonzero, and the Standard Model later explained why.

Another particle of interest exhibiting this nonzero anomaly is the muon, which is much like the electron but about 200 times heavier. Currently, both the experimental side and the

theory have found the muon magnetic moment anomaly value to very high precision, but the values disagree at a plausible level ($< 5\sigma$). Due to the possibility of exciting new physics being the cause of this discrepancy, efforts to achieve better precision remain active on both sides so a better comparison can be made. An alternative to repeating the experiment which increases confidence in the measurement is to check the experimental uncertainties. One such cross-check is the subject of this dissertation.

The most recent experimental value was measured at Brookhaven National Lab, which involved measuring two quantities very precisely to determine the anomaly. One of these quantities was the strength of the magnetic field experienced by the muons used in the experiment, which was measured to 170 parts per billion. A contributing factor to this uncertainty came from a water-based system which measured the magnetic field to 50 parts per billion. In the following dissertation, we verify this error by cross-checking the water-based devices employed in the BNL experiment with an independent device based on Helium-3 gas to 36 parts per billion.

We begin Chapter 2 with background information on the history of the Standard Model value of the anomaly as well as the experiments which measured it with increasing precision. We also provide motivation for using Helium-3 gas to perform the cross-check. Chapter 3 gives an overview of two techniques employed in the dissertation work to use Helium-3 gas as a magnetometer, i.e. a device which measures magnetic fields. The first technique is called MEOP, which was discovered in 1963 and is now widely used to hyperpolarize Helium-3 gas. The second technique, NMR, is employed broadly across the fields of physics, chemistry, and biology to measure magnetic fields. In chapters 4 and 5, we discuss the functionality of the Helium-3 magnetometer at low magnetic fields (Chapter 4) and high magnetic fields (Chapter 5). Finally, in Chapter 6, we provide the details of the cross-calibration of the BNL water-based magnetometers with the Helium-3 magnetometer. Lastly, we list results and conclude the dissertation with possible improvements for future endeavors with the Helium-3 magnetometer.

Chapter 2

Background and Motivation

2.1 Muon g-2: Theory and Experiment

2.1.1 Theory

The magnetic moment μ of a particle is proportional to its intrinsic spin \vec{S} . Specifically, for charged leptons (electrons, muons, and taus) of spin 1/2, the magnetic moment is given by:

$$\mu_l = \frac{g_l}{2} \frac{e\hbar}{2m_l}, \quad (2.1)$$

where e is the electronic charge, \hbar is Planck's constant, m_l is the mass of the respective lepton, and the factor g_l is more commonly written in terms of the magnetic moment anomaly a_l :

$$g_l = 2(1 + a_l) \quad (2.2)$$

From Dirac's theory, $g_l = 2$ for any spin-1/2 particle with charge $\pm e$, so the magnetic moment anomaly is expected to be $a_l = (g_l - 2)/2 = 0$. However the value was historically found to be nonzero first experimentally, and then theoretically. The theoretical standard model (SM) of particle physics predicts several radiative corrections to a_l due to the coupling of

the muon to virtual fields:

$$a_l = a^{QED} + a^{Weak} + a^{Had} \quad (2.3)$$

These corrections are detailed in [2].

The first term in equation 2.3, known as the Schwinger term, comes from the lowest order (LO) Quantum Electrodynamics (QED) process arising from interaction with a virtual photon. This is the largest correction and has been calculated to five loops giving $a_\mu \approx 1.16 \times 10^{-3}$ [3] [4]. The electroweak correction is due to diagrams with heavy bosons, such as W^\pm and the Z boson, and has been calculated to two loops [5], [6], [7–10]. The most recent calculation also includes interactions with the Higgs boson [11]. The remaining contributions to a_μ are all hadronic, calculated from Quantum Chromodynamics (QCD). These are the LO and HO (highest order) vacuum polarization (VP) contributions and a higher order light-by-light correction [12, 13], [14], [15]. Of these, the LO VP term dominates the QCD contribution to a_μ and two separate calculations exist. All the standard model corrections are summarized in table 2.1 from [2].

Any corrections Beyond the Standard Model (BSM) would be proportional to m_l^2 , making a_μ more sensitive to new physics than a_e by a factor of $m_\mu^2/m_e^2 \approx 4.3 \times 10^4$. While the electron magnetic moment anomaly is known extremely well to 0.6 parts per billion (ppb) [17], the most recent muon magnetic moment anomaly was measured to 0.54 ppm and differs from the SM value by 3.3σ [18]. Both the potential for a_μ to reveal new physics

Source	Contribution (10^{-11})	Uncertainty	Refs
QED - 5 loop	116 584 718.951	0.007, 0.077	[3, 4]
Electroweak	154	1	[5–11, 16]
Hadronic VP (LO)	6923	42	[12, 13]
Hadronic VP (LO)	6949	43	[14]
Hadronic VP (HO)	-98.4	0.7	[14]
Hadronic LBL	105	26	[15]
Total SM	116 591 802	49	
Total SM	116 591 828	50	

Table 2.1: Standard model contributions and uncertainties to a_μ .

and the discrepancy with the standard model are highly compelling for further calculations and experimental measurements. This also motivates efforts of increased scrutiny in any systematic uncertainties of the measured values, such as this dissertation work.

2.1.2 History of Experiments

The first few measurements of a_μ were conducted before 1960 and are described in [19]. Following these, a series of three experiments took place at CERN. The details are given in [18] and [19], and we provide a brief summary here. The first CERN experiment used a 6 meter long magnet with a known field gradient across the muon beam path. A polarized beam of muons was created using pion decay and a detector at the end of the beam path measured the polarization of the muons exiting the magnet. Since a_μ is nonzero, the muon's spin and momentum precess at different rates in the presence of a magnetic field. Measuring the polarization difference between the muons entering and exiting the magnet hence measured the change in precession. The result a_μ was reported to 4300 ppm (parts per million) [20], [21]. The second CERN experiment [22] employed a magnetic ring in which an injected proton beam hit a target to produce pions which decayed into muons. A magnetic field gradient provided vertical focusing of the muon beam. The detection of the positrons decayed from the muons yielded the muon precession frequency giving a_μ to 270 ppm.

The final CERN experiment made many improvements over the previous two. It employed a magnetic storage ring for the muons similar to the second experiment, but the injection and focusing were different. Instead of proton beam injection, the target was placed outside the ring and the pion beam was injected into the magnet, which reduced much of the background and provided increased muon storage. The experiment also used electric quadrupoles for the vertical focusing of the muon beam eliminating magnetic gradients and hence improving the uniformity of the field. This experiment was conducted for both μ^+ and μ^- and measured a_μ to 10 ppm for each polarity [23].

The most recent measurement of a_μ was conducted at Brookhaven National Lab (BNL) by

Experiment	Years	Precision (ppm)	Ref.
CERN I	1961	4300	[20], [21]
CERN II	1962-1968	270	[22]
CERN III	1974-1976	10	[23]
BNL	1997-2001	0.54	[18]
Fermilab	Ongoing	0.140	[24]

Table 2.2: List of experiments measuring a_μ and precision reached.

the E821 experimental collaboration and used the same general approach as CERN-III [18].

The improvements made included:

- a superconducting magnetic storage ring with higher field uniformity,
- an "indeflector" magnet capable of directly injecting muons in bunches every 33 ms, which reduced background and increased storage further,
- a "kicker" magnet to stabilize muon orbit and position,
- electrostatic quadrupoles with twice the strength of those used in CERN-III, and
- a circular storage volume (annular ring) as opposed to the square shape in CERN-III which reduced error in determining the magnetic field experienced by muons.

After a total of four runs with μ^+ and a fifth run with μ^- , BNL E821 reported a measurement of a_μ to 0.54 ppm [18]. We summarize the CERN and BNL results in table 2.2 just as was done in the BNL final result paper.

Currently, there is an ongoing effort at Fermi National Accelerator Laboratory by the E989 collaboration to improve the BNL measurement by a factor of 4 and measure a_μ to 140 ppb [24]. The BNL storage ring was transported to Fermilab for this effort in 2013 and the results from the first run will be unblinded this summer (2019). While this dissertation work was performed using a test magnet employed for E989, since we only report the cross-calibration of BNL magnetic field probes, a detailed description of the E989 experiment is outside the scope of this work. We instead give an overview of the BNL experiment (E821) in the next section.

2.1.3 BNL Experiment Method

Muons injected into a magnetic storage ring have a cyclotron frequency $\vec{\omega}_C = -q\vec{B}/m\gamma$, where q and m are the charge and mass of the muon, respectively, \vec{B} is the magnetic field, and γ is the Lorentz factor related to the velocity of the muon. Additionally, the muon spin precesses in the magnetic field with the frequency:

$$\vec{\omega}_S = \frac{-gq\vec{B}}{2m} - (1 - \gamma)\frac{q\vec{B}}{\gamma m} \quad (2.4)$$

Taking the difference of the two quantities gives:

$$\vec{\omega}_a = \vec{\omega}_C - \vec{\omega}_S = -\left(\frac{g-2}{2}\right)\frac{q\vec{B}}{m} = -a_\mu\frac{q\vec{B}}{m}, \quad (2.5)$$

where $\vec{\omega}_a$ is known as the anomalous precession frequency as it is directly related to a_μ . Due to the presence of the electric field \vec{E} from the electrostatic quadrupoles that provide focusing of the beam, there is an additional term introduced:

$$\vec{\omega}_a = -\frac{q}{m}\left[a_\mu\vec{B} - \left(a_\mu - \frac{1}{\gamma^2 - 1}\right)\frac{\vec{\beta}\times\vec{E}}{c}\right] \quad (2.6)$$

However, at the specific γ value of 29.3, the $\vec{\beta}\times\vec{E}$ term drops out and the equation for a_μ reduces to 2.5. By preparing muons with this γ at what is known as the magic momentum 3.094 GeV/c, the experimenters can ensure that the quadrupole field \vec{E} only causes the intended focusing effect. Then, as can be seen from equation 2.5, the muon magnetic moment anomaly a_μ can be determined by measuring the muon precession frequency $\vec{\omega}_a$ and the magnetic field \vec{B} of the storage volume.

The BNL experiment directly measured ω_a by detection of emitted positrons e^+ from the μ^+ decay. Due to parity violation in the weak interaction, the decay positron emission is preferentially in the direction of the muon spin, i.e. when the angle between the positron trajectory and the muon spin is 0° or 180° . More specifically, the energy of the positrons

is directly proportional to the cosine of this angle. Hence, by measuring this angular distribution of the emitted positrons over time, the precession of the muons ω_a can be measured. Detectors known as calorimeters were placed just outside the inner radius of the storage ring to measure the precession frequency for the BNL E821 experiment.

The magnetic field measurement used several Nuclear Magnetic Resonance (NMR) probes inside and outside the ring (see Chapter 3.3 for an overview of NMR). These probes were in general very precise, but their measured value included perturbations, such as shifts from susceptibilities of materials needed for probe construction. Due to this, an absolute reference was needed. The probes were calibrated absolutely to the precession frequency ω_p of free protons in the magnetic field. This frequency was then convoluted with the distribution volume of the muons to yield a new quantity $\tilde{\omega}_p$ which gave the field seen by the muons. The calibration chain which resulted in the ω_p measurement is described in the next section.

2.2 Magnetic Field Calibration and the ^3He Cross Check

2.2.1 Calibration Chain

As probes could not be placed in the storage region while muons were present, 378 NMR probes were instead mounted above and below the storage volume around the ring. Since these probes were not moved during data taking, they were referred to as fixed probes. At the beginning of the experiment, the fixed probes contained cylindrical water samples on which NMR was performed to constantly monitor the magnetic field when data was being taken. However, in between different runs of the experiment, the water samples were replaced with petroleum jelly for some of the fixed probes as petroleum produces similar signals to water and the measurements do not depend as highly on temperature. Petroleum also does not evaporate, which was part of the issue with the water samples. Lastly, the NMR relaxation times of petroleum are shorter than water (about 10 ms vs. 100s of ms), which yields a higher rate of measurement.

A group of 17 probes (identical in design to the fixed probes), were mounted in a trolley that could be pulled around the ring inside the storage volume. The probes were arranged in concentric circles covering up to 7 cm of the 9 cm total diameter of the storage region cross-section. The trolley scanned the ring every few days at random times, taking magnetic field measurements at about 6000 points around the ring [19]. During data collection with muons in the storage ring, the trolley was parked in an area adjacent to the storage volume out of the beam path. The trolley measurements (conducted when no data was being taken) and fixed probe measurements (conducted during both data-taking and non-data taking periods) were interpolated to generate a field map of the storage region experienced by the muons. This is how the trolley calibration was transferred to the fixed probes.

Next, the trolley probes were calibrated using a plunging probe which was finally calibrated with an absolute probe, which corrects the measured field value by a water sample to that of a free proton, hence the term 'absolute.' A plunging station was constructed near the storage region with a more homogenous field for the purpose of calibration. An absolute probe with a spherical water sample was used to cross-calibrate the plunging probe in the plunging station. The plunging probe could then be placed in the same positions as the trolley probes in vacuum and was used to transfer the absolute probe calibration to the trolley probes. Since the last link of the calibration chain was the absolute probe, all the probes were calibrated to the free proton field measurement.

Additionally, another absolute probe with a cylindrical water sample was used for a cross-check. The subject of this dissertation was to employ a probe with a sample different from water-based NMR, ^3He gas, to cross-calibrate both of the BNL absolute probes, the cylindrical probe and the spherical probe.

2.2.2 The ^3He Cross-Check

The absolute probes used in the BNL experiment measured the proton NMR frequency to 50 ppb [18]. While higher precision was not necessarily desired, it was essential to cross-

calibrate the probes against an independent probe since the absolute calibration error in the experiment could have contributed to the discrepancy between the BNL result and the predicted SM value. We employed a Helium-3 gas based magnetometer to cross-calibrate both BNL absolute probes, which offers several advantages over water:

- hyperpolarized gas could produce higher signal-to-noise,
- the low susceptibility of the gas at low pressure leads to small shape dependent corrections,
- the diamagnetic shielding factor has a small uncertainty (0.1 ppb),
- the diamagnetic shielding factor has a small temperature dependence.

Additionally, multiple ^3He samples can be employed with different systematic corrections. For example, since the NMR signal from ^3He is dependent on the pressure of the gas and the polarization in the sample, different samples with varying gas pressures and polarizations could be used. These physical quantities could behave as knobs that control the systematic uncertainties of each probe. Correcting multiple probes with different systematic errors would increase the level of confidence in the measurement.

2.2.3 Calibration Overview

From equation 2.5, the precession frequency can be written in terms of the magnetic moment anomaly:

$$\omega_a = \frac{e}{m_\mu} B a_\mu \tag{2.7}$$

The quantity measured in the experiment is not B , but the proton frequency ω_p (or the ^3He frequency ω_3) which yields the magnetic field value: $\omega_s = 2(\mu_s/\hbar)B$, where the subscript s denotes the standard used for calibration (protons or ^3He nuclei). Solving this equation for B and plugging the result into 2.7, we can write the anomaly in terms of known constants

and the two measured values ω_a and ω_s :

$$a_\mu = 2 \frac{m_\mu \mu_s \omega_a}{e \hbar \omega_s} \quad (2.8)$$

Since the ratio of the muon mass to the electron mass is known to 22 ppb [25], μ_μ/μ_e has a lower uncertainty than the muon mass by itself (25 ppb). Substituting $e\hbar = 4\mu_e m_e/g_e$ from equation 2.1, we find:

$$a_\mu = \frac{g_e \omega_a \mu_s m_\mu}{2 \omega_s \mu_e m_e} \quad (2.9)$$

where g_e is the electron g-factor related to the electron magnetic moment anomaly, and μ_e is the electron magnetic moment. Since e and \hbar have been measured to 6.1 and 12 ppb, respectively, the new equation greatly reduces the uncertainty on a_μ ($g_e \sim 1$ ppt, $\mu_p \sim 7$ ppb, $\mu_3 \sim 13$ ppb, $\mu_e \sim 6.2$ ppb, $m_\mu/m_e \sim 22$ ppb, [25]). The equation thus gives the muon magnetic moment anomaly in terms of constants measured to high precision and the two measured quantities in the experiment ω_a and ω_s ($= \omega_p$ or ω_3).

Here ω_s is the precession frequency of a free proton or ^3He nucleus (helion) in a magnetic field. Since the absolute probes first measure the frequency of the shielded protons in water or the shielded helion nuclei in the helium-3 atom, the measurement must be corrected to the unshielded value using the diamagnetic shielding factor for each (σ_p , σ_3). However, we can eliminate this step by not correcting to the free proton or free helion frequency, and instead express a_μ in terms of the shielded frequency measurement:

$$a_\mu = \frac{g_e \omega_a \mu'_s m_\mu}{2 \omega'_s \mu_e m_e} \quad (2.10)$$

This is highly beneficial because while both μ'_p and μ'_3 are known to 13 ppb, their ratio μ'_3/μ'_p has been measured to 4.3 ppb. Since we are only interested in comparing the measurements between the ^3He and water probes for the cross-check, we can cross-calibrate to much higher precision by using the ratio of the shielded values.

2.2.4 Review of ^3He γ measurements

We provide a brief overview of the history of measured magnetic moments (directly related to the gyromagnetic ratio γ) of ^3He . In 1969, Williams and Hughes [26] measured the ratio of the shielded ^3He magnetic moment to protons in shielded hydrogen gas: $-\mu'_3/\mu'_p(H_2) = 0.76178685 \pm 1$ ppm. They also reported the ratio corrected for the shielding factors as: $-\mu_3/\mu_p = 0.76181237 \pm 0.6$ ppm. In 1993, Flowers et al. [27] measured the ratio of the shielded ^3He magnetic moment to the shielded protons in water: $-\mu'_3/\mu'_p(H_2O) = 0.7617861313(33)$ (uncertainty 4.3 ppb). Most recently, in 2012, Neronov et al [28] provided a measurement of the shielded ^3He magnetic moment with respect to shielding of protons in hydrogen (H_2), similar to the Williams and Hughes measurements: $-\mu'_3/\mu'_p(H_2) = 0.761786594(2)$. Correcting for the shielding factors, they provide the unshielded ratio: $-\mu_3/\mu_p = 0.761812217(3)$.

While the uncertainty of this last measurement, 3.9 ppb, is lower than that of the Flowers result, 4.3 ppb, we use the latter result for the cross-calibrations performed in this dissertation work. This result gives us the added benefit of eliminating the step of correcting our ^3He and water probe frequency measurements by the shielding factors, which would introduce further errors. Hence the only error present in our cross-calibration due to the different probe samples is 4.3 ppb.

Chapter 3

Theory: MEOP and NMR

This chapter covers the theory behind the ^3He magnetometer operation. We start with motivation for why ^3He gas must be hyperpolarized to be used as a magnetometer. We then describe the principles of Metastability Exchange Optical Pumping (MEOP) which is used to hyperpolarize the gas. Finally, we give an overview of Nuclear Magnetic Resonance, which is the technique used to extract a magnetic field value from the polarized ^3He sample.

3.1 Need for Hyperpolarization of ^3He

All current precision magnetometers utilize NMR (Nuclear Magnetic Resonance), which is performed on magnetized samples. The magnetization is proportional to the density ρ , spin polarization P , and the magnetic moment μ of the sample: $M = \rho P \mu$. For a sample with given density and magnetic moment, higher polarization yields a larger NMR signal. Therefore any sample used with NMR must have a large polarization.

In the presence of a magnetic field B , spin-1/2 particles align either with or against the field. If we define B along the z-axis, the polarization in a sample is given by:

$$P_z = \frac{N_\uparrow - N_\downarrow}{N_\uparrow + N_\downarrow}, \quad (3.1)$$

where N_{\uparrow} are the number of nuclei aligned with the field (in the $m = +1/2$ magnetic sublevel) with energy $E_{\uparrow} = -\mu B$ and N_{\downarrow} is the number of nuclei against the field (in the $m = -1/2$ sublevel) with energy $E_{\downarrow} = \mu B$, with the total number of nuclei $N = N_{\uparrow} + N_{\downarrow}$. According to the Boltzmann distribution at temperature T , the fraction of population in each state is:

$$\frac{N_{\uparrow}}{N} = \frac{e^{\frac{+\mu B}{k_B T}}}{e^{\frac{-\mu B}{k_B T}} + e^{\frac{\mu B}{k_B T}}} \quad \text{and} \quad \frac{N_{\downarrow}}{N} = \frac{e^{\frac{-\mu B}{k_B T}}}{e^{\frac{-\mu B}{k_B T}} + e^{\frac{\mu B}{k_B T}}},$$

where k_B is Boltzmann's constant. The polarization is then given by

$$P_z = \frac{N e^{\frac{\mu B}{k_B T}} - N e^{\frac{-\mu B}{k_B T}}}{N e^{\frac{\mu B}{k_B T}} + N e^{\frac{-\mu B}{k_B T}}} = \frac{e^{\frac{2\mu B}{k_B T}} - 1}{e^{\frac{2\mu B}{k_B T}} + 1} \approx \frac{\mu B}{k_B T} \approx \frac{\gamma \hbar B}{2k_B T} \quad (3.2)$$

where γ is the gyromagnetic ratio of the sample and \hbar is Planck's constant. At room temperature and for the same field B , ^3He has a lower polarization, P , than water by a small factor of 1.3 given by the ratio of γ_{water} to γ_3 . However, conventional water samples are low pressure with a density 6 orders of magnitude greater than typical ^3He gas samples used at low pressure (e.g. 2 Torr). Hence the magnetization, $M = \rho P \mu$, of water samples with P given by the Boltzmann distribution is large enough for NMR. However, low pressure ^3He , due to the much smaller density, must be hyperpolarized first to achieve a high enough magnetization for NMR.

3.2 Metastability Exchange Optical Pumping

Hyperpolarization of spin-1/2 gases can be achieved using two techniques: Spin-Exchange Optical Pumping (SEOP) or Metastability Exchange Optical Pumping (MEOP). SEOP [29], [30] is generally performed on high pressure gas with an alkali metal. The metal is first polarized with optical pumping and the polarization gets transferred to the ground state of the gas via spin-exchange collisions. Polarization times with SEOP are long (hours) and the level of polarization achieved is usually low. MEOP is more applicable for low pressure gas,

such as the samples used in this work (2-40 Torr ^3He). Using MEOP is also more beneficial because the polarization times are much shorter (minutes) and the resulting polarization is higher than with SEOP. Another advantage of MEOP over SEOP is that pure ^3He gas samples can be used without chemical shifts that would be introduced by the alkali metals needed for SEOP.

3.2.1 MEOP at Low Field

The detailed theory of MEOP is outlined in references [31], [32], [33], and [34]. We give a brief overview here.

The ground state of ^3He has total electronic angular momentum $J = L + S = 0$ and since the nuclear spin is $I = 1/2$, the total angular momentum $F = J + I = 1/2$. In a magnetic field, this ground state has two sublevels $m_F = +1/2, -1/2$. The goal of MEOP is to induce a nuclear polarization in the gas so that the population of one sublevel is considerably higher than the other. The transition from the ground state 1^1S_0 to the first excited state 2^3S_1 of ^3He is optically forbidden due to selection rules ($\Delta l = 0$), and the energy difference is also inaccessible with lasers (19.8 eV). Hence the ground state atoms cannot be optically pumped into any excited states. Instead, the first step of MEOP is to strike a high radio frequency discharge in the gas sample, through which the ground state atoms are excited to higher levels and then radiatively decay to 2^3S_1 as shown in Figure 3.1a. These atoms cannot spontaneously decay to the ground state due to the optically forbidden transition, so the first excited state, 2^3S_1 , is a metastable state.

This state has nonzero total electronic angular momentum, which combined with the $I = 1/2$ nuclear spin yields two hyperfine sublevels $F = 1/2$ and $F = 3/2$ with six magnetic sublevels. Similarly, the next excited state 2^3P has five hyperfine sublevels 2^3P_0 ($F=1/2$), 2^3P_1 ($F=1/2, 3/2$), 2^3P_2 ($F=3/2, 5/2$), with 18 magnetic sublevels. The energy difference between these states at low and high field are calculated in detail by Courtade, et al [35]. We have adapted one figure (Figure 3.2) from the paper for the purposes of this work showing

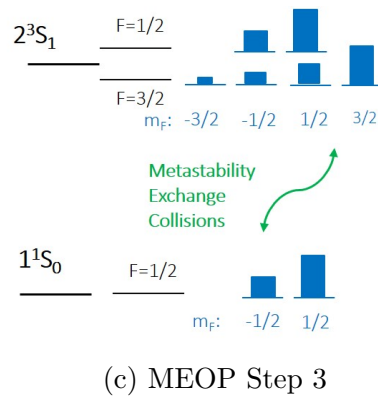
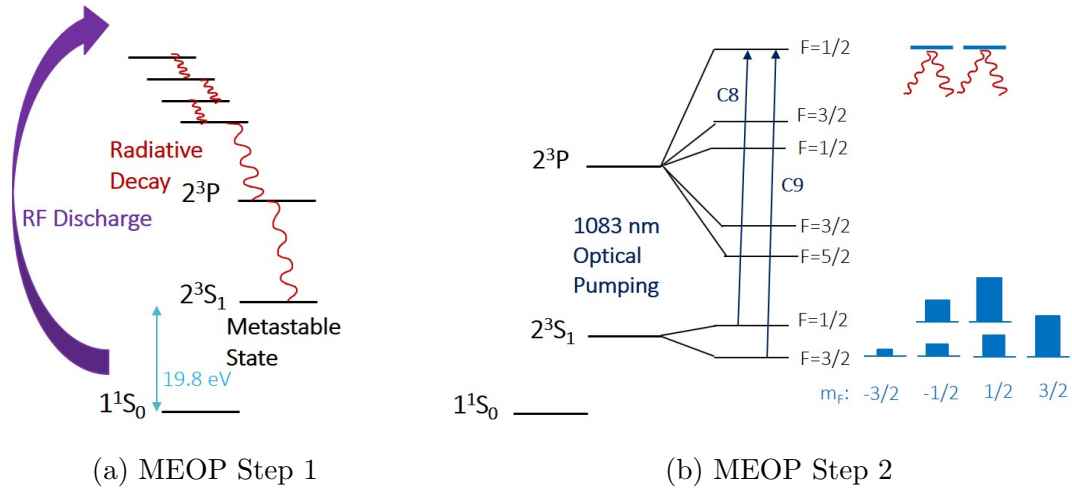


Figure 3.1: The three steps of low field MEOP. Figures adapted from [1]

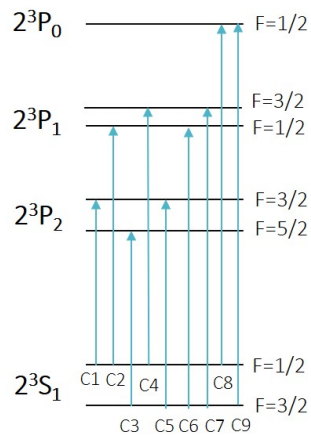
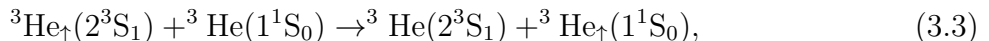


Figure 3.2: Absorption lines of ^3He from 2^3S to 2^3P

all the 2^3S and 2^3P transitions. After the discharge initializes the atoms to the first excited state in the first step of MEOP, the second step is to use 1083 nm light to optically pump from the 2^3S_1 state to 2^3P via the C_8 or C_9 transitions shown in Figure 3.2.

In the presence of a magnetic field, a circularly polarized incident beam, for example σ_+ on C_8 , will optically pump the 2^3S_1 atoms with $F=1/2$, $m_F = -1/2$ into the sublevel of 2^3P_0 with $F=1/2$, $m_F = 1/2$, which then decay to any of the six sublevels of 2^3S_1 , as seen in Figure 3.1b. As the optical pumping beam constantly depopulates the $m_F = -1/2$ sublevels, there is a larger polarization of atoms in the $F=1/2$, $m_F = 1/2$ sublevel than the $m_F = -1/2$ sublevel. This induces a nuclear polarization in the first excited state, which concludes the second step of MEOP.

The third and final step of MEOP occurs when the polarized ^3He atoms ($^3\text{He}_\uparrow$) transfer their nuclear polarization to the ground state atoms via metastability collisions:



where the arrows indicate the nuclear polarization transferred from excited-state to ground-state atoms (Figure 3.1c). This final step creates an overall nuclear polarization in the ground state, hyperpolarizing the gas.

When these polarized ground state atoms are again excited by the rf discharge, the 668 nm emitted light in the radiative decay (3^1D_2 to 2^1P_1) that follows is circularly polarized [36], [37]. The degree of circular polarization of this emission is directly proportional to the degree of nuclear polarization of the gas, with the proportionality constant given by a pressure dependent factor from [38]. Hence measuring the degree of circular polarization of 668 nm light gives the nuclear polarization of the gas in the low field regime of a few Gauss.

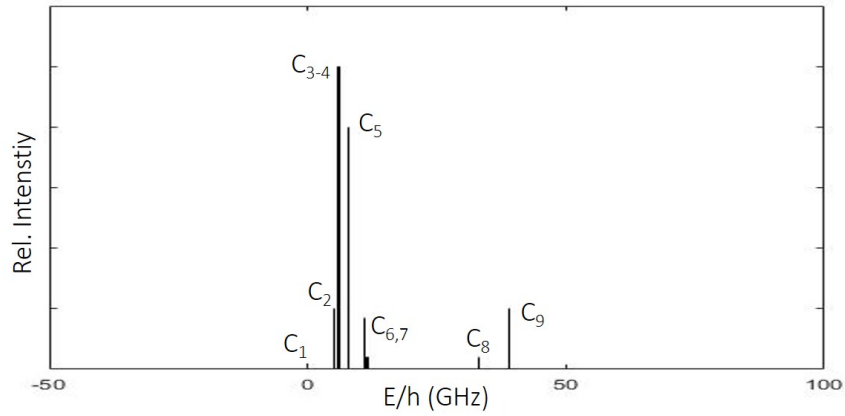
3.2.2 MEOP at High Field

The previous section applies to low field (few Gauss) MEOP. For the high field regime (>0.1 Tesla), the effects of the field on MEOP are studied and theoretical calculations are detailed in [35], while results from experiments at 1.5 T are given in [39]. The main change that occurs at high field is the change in energy sublevel separations. As the Zeeman splitting increases with the field, the energy levels of ^3He are modified. Specifically at 1.5 T, the Zeeman splittings are larger than the hyperfine, which leads to a few different effects.

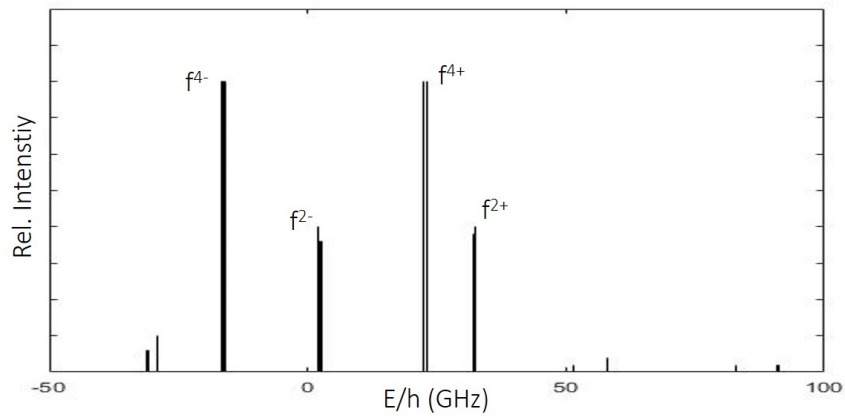
The first is that the absorption spectrum of the gas changes with the different sublevel splittings, which spread over 150 GHz at 1.5 T as compared to 40 GHz at low field [1], [39], [40]. The optical pumping beam for MEOP must therefore be tuned to resonance on the new transition lines, known as $f^{2+/-}$ and $f^{4+/-}$, where the + and - indicate right and left circular polarization of light, respectively. Figures 3.3a and 3.3b adapted from [1] show the low field and high field absorption lines including $f^{2+/-}$ and $f^{4+/-}$. Since the Zeeman splittings are larger than the hyperfine, the optical pumping beam does not have to have as pure a circular polarization as in the case for low field.

Another effect due to the energy level changes is that the electronic and nuclear polarizations are coupled weakly (hyperfine coupling is weak), which makes it harder to achieve nuclear polarization in the gas with MEOP potentially requiring longer polarization build up times. However, this can be compensated for with a higher power optical pumping beam. On the other hand, due to the same weak hyperfine coupling, less polarization is lost in the light from the discharge (the same 668 nm light used to measure nuclear polarization at low field) so the net nuclear polarization of the gas, once achieved, is more easily retained. This also implies that the polarization of emitted light can no longer be used to measure the nuclear polarization.

In summary, to use MEOP at high field, a high power laser tunable over a broader change of energies ($\sim 200\text{GHz}$), including resonances on $f^{2+/-}$ and $f^{4+/-}$, is needed. Abboud et al [39] measure polarizations up to 80% in samples of 1-60 Torr in a 1.5 T field. While we do



(a) Low field (few Gauss) absorption lines of ^3He adapted from [1].



(b) High field (1.5 T) absorption lines of ^3He adapted from [1].

Figure 3.3: Low (a) and high (b) field absorption lines for ^3He MEOP. The relative intensities are only estimates and all lines are with respect to the low field C_1 line at 0 GHz.

not measure the degree of nuclear polarization in our samples at high field, we do successfully hyperpolarize our cells via MEOP and use them with NMR (Chapter 5).

3.3 NMR: Nuclear Magnetic Resonance

We describe the main principles of Nuclear Magnetic Resonance based on the theory detailed by Abragam [41] and Slichter [42] using a semiclassical picture. While NMR is conventionally performed on samples with magnetization $M = \rho P \mu$, we describe the formalism for one magnetic moment μ , which can be generalized to a sample with many nuclei.

For a nucleus with angular momentum \vec{I} and magnetic moment $\vec{\mu}$,

$$\vec{\mu} = \gamma \vec{I}, \quad (3.4)$$

where γ is the gyromagnetic ratio. In a magnetic field \vec{B} , the magnetic moment experiences a torque $\vec{\mu} \times \vec{B}$ which from Newton's second law is equal to the rate of change of the angular momentum:

$$\vec{\tau} = \vec{\mu} \times \vec{B} = \frac{d\vec{I}}{dt} \quad (3.5)$$

Plugging equation 3.4 into this, we find the equation of motion for $\vec{\mu}$:

$$\vec{\mu} \times \gamma \vec{B} = \frac{d\vec{\mu}}{dt} \quad (3.6)$$

At this point, the NMR formalism utilizes the technique of switching to a rotating frame. Following [41], we label the lab frame S and define a new frame S' which rotates at an angular velocity $\vec{\omega}$ with respect to S . The time derivative of a vector \vec{A} in the S' frame, $\delta\vec{A}/\delta t$, will then be related to the time derivative in the lab frame, $d\vec{A}/dt$, by:

$$\frac{d\vec{A}}{dt} = \frac{\delta\vec{A}}{\delta t} + \vec{\omega} \times \vec{A} \quad \rightarrow \quad \frac{\delta\vec{A}}{\delta t} = \frac{d\vec{A}}{dt} + \vec{A} \times \vec{\omega} \quad (3.7)$$

from laws of relative motion. Applying this to equation 3.6 yields the equation of motion for $\vec{\mu}$ in the rotating frame:

$$\frac{\delta\vec{\mu}}{\delta t} = \vec{\mu} \times (\gamma\vec{B} + \vec{\omega}) = \vec{\mu} \times \gamma(\vec{B} + \frac{\vec{\omega}}{\gamma}) \quad (3.8)$$

Comparing this to 3.6 shows that this equation of motion is that of $\vec{\mu}$ in an effective magnetic field $\vec{B}_{eff} = \vec{B} + \vec{\omega}/\gamma$ in the rotating frame. If we define the magnetic field in the lab frame to be static along z: $\vec{B} = B_0\hat{z}$, the effective field \vec{B}_{eff} is 0 when $\vec{\omega} = -\gamma B_0\hat{z}$. This is known as the Larmor frequency at which the equation of motion of $\vec{\mu}$ in S' reduces to $\delta\vec{\mu}/\delta t = 0$, indicating that the the magnetic moment does not move in the rotating frame. Hence, $\vec{\mu}$ precesses at the Larmor frequency $\vec{\omega}$ in the lab frame in the presence of the magnetic field $\vec{B} = B_0\hat{z}$. The power of NMR as an experimental technique is that \vec{B} can be measured by measuring the Larmor frequency of a sample of nuclei with a known γ .

3.3.1 Pulsed NMR

We now extend the formalism of the previous section to include a time-varying field in addition to B_0 to demonstrate the concept of pulsed NMR as is done in [41]. Let $\vec{B}_0 = B_0\hat{z}$ be a static field with the associated Larmor frequency $\omega_0 = -\gamma B_0$. We define another field $\vec{B}_1(t)$ to be perpendicular to \vec{B}_0 and rotating with angular velocity ω in the lab frame:

$$\vec{B}_1(t) = [\cos(\omega t)\hat{x} + \sin(\omega t)\hat{y}]B_1 \quad (3.9)$$

Then, in the S' frame which rotates with ω , \vec{B}_1 lies along \hat{x}' . The effective field in the rotating frame is then:

$$\vec{B}_{eff} = (B_0 + \frac{\omega}{\gamma})\hat{z}' + B_1\hat{x}', \quad (3.10)$$

where the \hat{z}' term results from rotating B_0 to S' just as was done in equation 3.8.

If we define $\omega_1 = -\gamma B_1$ as the Larmor frequency associated with B_1 (where B_1 is always

be positive), the magnitude of the effective field will be given by:

$$\begin{aligned} B_{eff} &= [(B_0 + \frac{\omega}{\gamma})^2 + B_1^2]^{1/2} \\ &= [(-\omega_0 + \omega)^2 + \omega_1^2]^{1/2} \frac{1}{|\gamma|} \end{aligned}$$

Notice that comparing the new effective field to the previous section, we find that $\omega_{eff} = -\gamma B_{eff}$ represents the Larmor field associated with B_{eff} in the rotating frame. The precession of the magnetic moment $\vec{\mu}$ in the lab frame is a combination of this rotation and ω , the angular velocity between the lab and rotating frame.

The angle θ between the effective field \vec{B}_{eff} and \vec{B}_0 can be calculated using:

$$\tan(\theta) = \frac{\omega_1}{\omega_0 - \omega}, \quad \sin(\theta) = \frac{\omega_1}{\omega_{eff}}, \quad \cos(\theta) = \frac{\omega_0 - \omega}{\omega_{eff}} \quad (3.11)$$

While this angle is static, the angle between the magnetic moment and B_0 in the lab frame changes as a function of time and is given by

$$\cos(\alpha) = \cos^2(\theta) + \sin^2(\theta)\cos(\omega_{eff}t) \quad (3.12)$$

assuming that the magnetic moment and B_0 are both aligned with \hat{z} in the lab frame at time $t=0$ [41].

In practice, the magnitude of B_1 is much smaller than B_0 , which gives rise to resonance: α is small unless $\omega - \omega_0$ is small (comparable to ω_1). In other words, the magnetic moment remains aligned with B_0 along the z-axis, unless ω , the frequency of the field B_1 is close to ω_0 , the Larmor frequency of B_0 . This means that by turning on a field B_1 with a frequency close to ω_0 for some time t , it is possible to controllably rotate the magnetic moment out of the z-axis to some angle α , at which point the magnetic moment precesses in a cone about the z-axis. When this rotation angle is 90° , the $B_1(t)$ field is called a $\pi/2$ pulse which must

have a duration of:

$$t_{1/2} = \frac{\pi}{2} \frac{1}{\gamma B_1} \quad (3.13)$$

After such a $\pi/2$ pulse is used to rotate the precession into the transverse plane, a pick up coil can be used to pick up the induction current from this precession. The signal of the coil is known as the Free Induction Decay (FID), since the precession decays due to relaxation mechanisms (see next section). The FID signal can be analyzed to extract the frequency ω_0 , hence providing a measure of the B_0 magnetic field. This process is known as pulsed NMR.

Lastly, we must clarify that in practice, the B_1 field is linear instead of rotating about the B_0 field axis. However, a linear field such as $2\cos(\omega t)$ can be separated into two components, one rotating at ω and another rotating in the opposite direction with $-\omega$. Due to the resonance condition, only the ω component of the field effects the rotation, as the $-\omega$ component is off resonance and its effect is negligible (known as the Bloch-Seigert Shift) [41].

3.3.2 Relaxation

For a collection of magnetic moments in a sample of density ρ , polarization P , and magnetization $M = \rho P \mu$, an NMR pulse rotates the net magnetization, $M_0 = M_z$, initially aligned with the B_0 field (along z-axis). The rotated magnetization then precesses about the magnetic field B_0 just as was described in the previous section for one magnetic moment μ . There are several relaxation processes that can cause \vec{M} to rotate back to equilibrium. For the case of water, the transverse magnetizations M_x and M_y decay, while the longitudinal magnetization, M_z , aligns back with the B_0 field to the equilibrium value M_0 given by the Boltzmann distribution. However, for ^3He gas, the relaxation processes effectively eliminate the longitudinal magnetization since the magnetization at equilibrium is small for the low density gas. Note that the initial magnetization M_0 in ^3He is produced by hyperpolarization of the sample via MEOP.

The relaxation of the magnetization $M = M_x \hat{x} + M_y \hat{y} + M_z \hat{z}$ in the lab frame is given

by the phenomenological Bloch equation(s) [41]:

$$\frac{d\vec{M}}{dt} = \vec{M} \times \gamma \vec{B} - \frac{M_x \hat{x} + M_y \hat{y}}{T_2} - \frac{M_z - M_0}{T_1} \hat{z}, \quad (3.14)$$

where T_1 is the longitudinal relaxation time for M_z to return to equilibrium, and T_2 is the transverse relaxation time over which M_x and M_y decay. The mechanisms causing this relaxation are described in [32], [30], [43], and [44].

The longitudinal relaxation time, T_1 , can be caused by the moments losing energy to their surroundings, or the “lattice,” which is why T_1 is also known as the “spin-lattice” relaxation time. Additionally, collisions of the nuclei with the wall of the container can cause depolarization which contributes to the longitudinal relaxation. Due to this, T_1 is also called the “wall” relaxation time. Lastly, gradients in the transverse components of the field B_x and B_y can cause rotations of the magnetic moments in random directions, causing the longitudinal magnetization to decay. These three effects combined determine the T_1 time of the sample. For a low pressure gas in a spherical container of radius R , [44] and [45] give:

$$\frac{1}{T_1} = \frac{8R^2\gamma^2}{175D} [\vec{\nabla} B_x^2 + \vec{\nabla} B_y^2], \quad (3.15)$$

where D is the diffusion coefficient of the gas and is inversely proportional to the pressure of the sample. Typical T_1 times are in the few hours range. The dipole-dipole interaction of the ^3He nuclei can also cause relaxation of the polarization, which is about ~ 700 hours for atmospheric pressures of the gas. This effect can contribute to T_1 but is not dominant (time scale much longer) than the three effects described above.

T_2 , the transverse relaxation time, is caused by interactions of the moments with each other, and is hence called the “spin-spin” relaxation time. Any gradients in the field lead to the nuclei seeing a different magnetic field in different parts of the sample, which can cause the nuclei to precess out of phase with one another. This causes the transverse magnetization to decay. In the motional narrowing regime where the gas is at low pressure and placed in

a high magnetic field, the observed tranverse relaxation time is known as T_2^* and is given by [44], [45]:

$$\frac{1}{T_2^*} = \frac{4\gamma^2 R^2}{175D} (\vec{\nabla} B_x^2 + \vec{\nabla} B_y^2 + 2\vec{\nabla} B_z^2) = \frac{1}{2T_1} + \frac{8R^2}{175D} (\vec{\nabla} B_z^2) \quad (3.16)$$

As pressure increases, the nuclei diffuse faster and hence can sample the different field gradients in different positions within the container. This leads to a pressure broadening effect which can result in an increased T_2^* [45].

Chapter 4

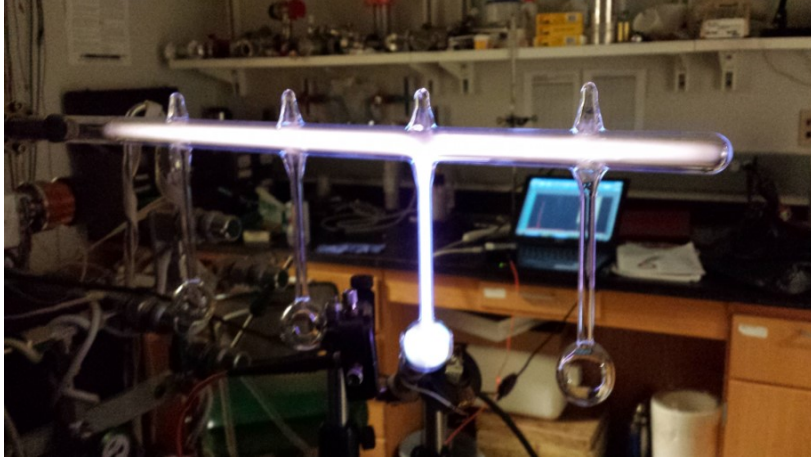
Low Field MEOP and NMR Studies

The theory of low field MEOP and NMR are described in Chapter 3, where we also provide references [1], [31], [33], [34]. In this chapter, we provide the details of the low field experimental setup and procedure followed by ^3He probe studies in low field.

4.1 ^3He Sample Cells: Making, Cleaning, and Filling

The sample cells used in this work were made of borosilicate glass (Pyrex) by University of Michigan's in-house glass blower, Roy Wentz. Four cells were blown into approximately 2 cm diameter spherical bulbs attached to 'stems' of 4 mm OD, 3 mm ID glass tubes 10 cm long. The opposite side of these stems were attached to a 10 mm OD tube, with the stems spaced by about 6-7 cm in a manifold as shown in Fig. 4.1a. The 10 cm tube also had short 4 mm tubes mounted directly across from each cell and stem for cleaning the cells. These tubes were initially open tubes, but were closed off with a glass-blowing torch after the cleaning process, described below, was completed. An unavoidable small part of the stem remained attached to each cell due to the pull off.

We cleaned the cells with a rigorous cleaning process using a solution called piranha – a mixture of 70% sulfuric acid and 30% hydrogen peroxide. The cells were first rinsed with methanol and deionized (DI) water 3 times each and then filled with piranha, which was



(a) Four ^3He glass cells mounted on the vacuum and gas filling system. One of the cells is glowing due to the RF discharge.



(b) Single ^3He cell and stem after pull off. The loop of wire is one of the two coils connected to the transformer used to strike the discharge.

Figure 4.1: ^3He cells before and after pull off from string.

stored in the cells for ~ 15 -20 hours as this was the major cleaning step for removing all organic matter from the glass. The piranha was then carefully poured out and the cells were again rinsed with DI water 3 times, followed by 3 rinses with high purity methanol, and 3 more rinses with DI water.

After the cleaning process, the cells were baked in an oven at 100°C temperature for ~ 12 hours to remove any remaining residue. We then mounted the cells onto a vacuum system to pump them out using 2-3/4" conflat flanges and wrapped heat tape around them to provide heat for the process (100 - 200°C). The cells were pumped down to 10^{-8} Torr over a period of 1.5 days and then filled with pure ^3He gas. Before pulling off each individual cell from the group, we checked the purity of the gas. This was done by striking a high radio-frequency (RF) discharge in the gas (which is also the first step of MEOP) and studying the glow from this discharge with a spectrometer (Ocean Optics USB4500). The discharge glow can be seen in Figure 4.1. We checked the gas purity by studying the wavelength of each line in the discharge emission spectrum.

We found through this test that some Xenon had leaked into the cells from our gas filling system (see Figure 4.2a), as confirmed by comparing the observed emission lines to xenon spectral lines from the National Institute of Standards and Technology (NIST) database [46].

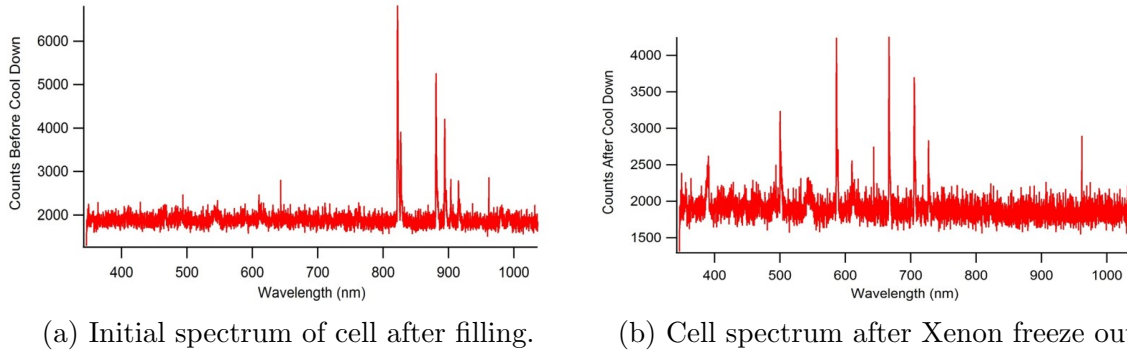


Figure 4.2: Spectrum of cell as measured by spectrometer before and after freeze out.

This was not surprising since the filling system was also used to fill cells with a mixture of ^3He and enriched ^{129}Xe for another experiment in our research group [47]. We were able to freeze out the xenon by holding a cup of liquid nitrogen around one of the cells, leaving only pure helium gas in the remaining cells. The purity was again checked by looking at the emission spectrum of the discharge with a spectrometer (Figure 4.2b) and comparing it to typical Helium emission lines from NIST [46]. Note that these helium lines were suppressed when the xenon gas was present in Figure 4.2a.

Once the purity of the gas was confirmed, we pulled off each cell in our lab using glass-blowing methods, and they were ready to be polarized with MEOP. Each cell was about 1 inch in diameter and consisted of a 0.25 inch stem due to the pull off from the tube as shown in Figure 4.1b.

4.2 Low-field MEOP: Experimental Setup

4.2.1 RF Discharge and Optical Pumping

As explained in Section 3.2, the first step of MEOP requires exciting the ^3He gas with a radio-frequency (RF) discharge. We generated the signal using a function generator, Sanford Research Systems (SRS) Model DS345, in the MHz frequency range and sent it through an amplifier (ENI RF Power Amplifier, Model A150, 40 W, 50 dB [48]) to increase the amplitude

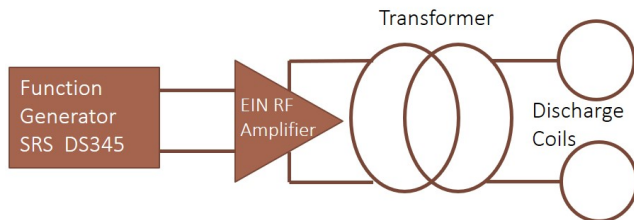


Figure 4.3: Electronics for striking ^3He discharge.

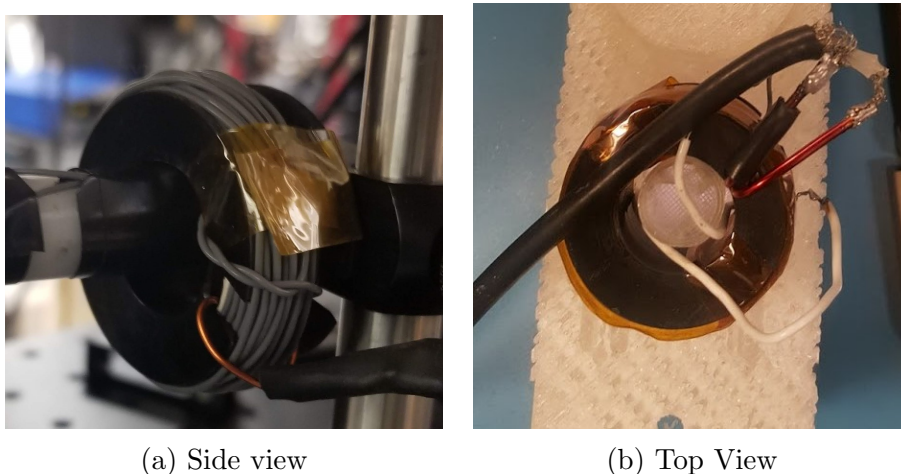


Figure 4.4: Transformers made to strike ^3He discharge. $N=80$ turns for grey or white wire, $N=2$ turns for red wire.

of the rf wave. The cable then split into two 0.5 inch diameter coils that were wrapped around the ^3He cell (see Figure 4.1b). We found that the amplifier gain was not high enough to strike a discharge, partially due to the coils having a different resonant frequency than the amplifier output. To address this issue, we made several iterations of transformers to match the resonant frequency of the amplifier as well as to amplify the signal further. Figure 4.3 shows the diagram for the final electronics used to strike the ^3He discharge including the transformer.

The final transformer design consisted of two sets of wrapped wires, one 22 AWG wire with 2 turns (primary) and another 18 AWG magnet wire with 80 turns (secondary), giving a voltage gain of about 40. Two of our home-built transformers are shown in Figures 4.4a and 4.4b; each steps up the voltage, decreasing the circuit current in the process. The resonant frequency of the circuit ranged from 4 to 6 MHz depending on the transformer and cell.

Since the cell loads the coils, the impedance and hence the resonant frequency both depend on the cell. The initial function generator amplitude of 200-350 mV was amplified with the EIN rf amplifier to 20-40 Volts, stepped up through the transformer and finally delivered to the cell through the circular coils.

After successfully striking a discharge in the sealed cells, we carried out studies of its glow spectrum with the spectrometer as described in the previous section to further confirm purity after the cells were sealed. We also studied the absorption spectrum of the gas using a single-wavelength laser at 1083 nm, the resonant wavelength between 2S and 2P levels of ^3He gas, and the relevant transition for MEOP (see section 3.2 for MEOP theory). The laser was a 50 mW Distributed Bragg Reflector diode (SDL-6700) with power provided by a Thorlabs LDC500 current controller. The wavelength of the laser could be tuned by 2 nm by changing the temperature of its grating reflector using Thorlabs TEC 2000. The absorption spectrum was studied with the discharge on since the discharge initializes the electrons into the 2S state, from which they are excited by the laser. As the laser wavelength was tuned, we observed the absorption dips by measuring the power of the beam transmitted through the cell incident on a detector - either a photodiode (Thorlabs PDA100A) connected to a voltmeter or a power meter (Coherent LabMax Top). Figure 4.5 shows the measured absorption spectrum which agreed well with a typical ^3He energy spectrum from [1], [33]. The comparison was used to label each absorption dip from Figure 3.2, specifically the C8 and C9 lines relevant for MEOP.

For MEOP, specifically for the optical pumping step, a magnetic field must be present. As shown in Figure 4.6, we placed the cell in the center of 14 cm diameter Helmholtz coils, providing a magnetic field of $B_0 \approx 7.5$ Gauss, as measured by a Hall probe. The 1083 nm laser beam propagated parallel to B_0 and was tuned either to the C8 or the C9 absorption line. The beam was expanded to about 1 inch diameter using a lens, to cover the cell. Since the goal was to optically pump the atoms into a magnetic sublevel, the resonant light needed to be circularly polarized, either left or right. This was accomplished with a linear polarizer

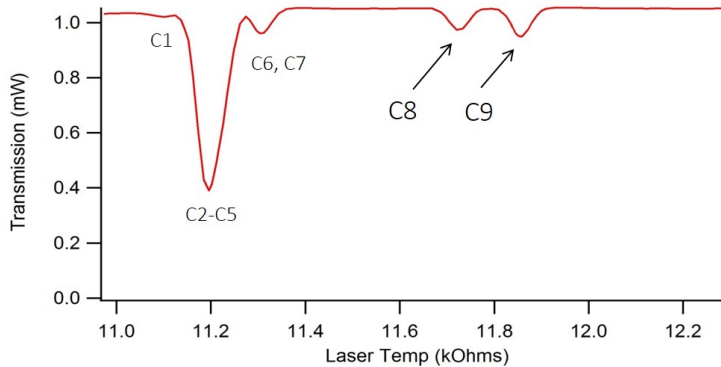
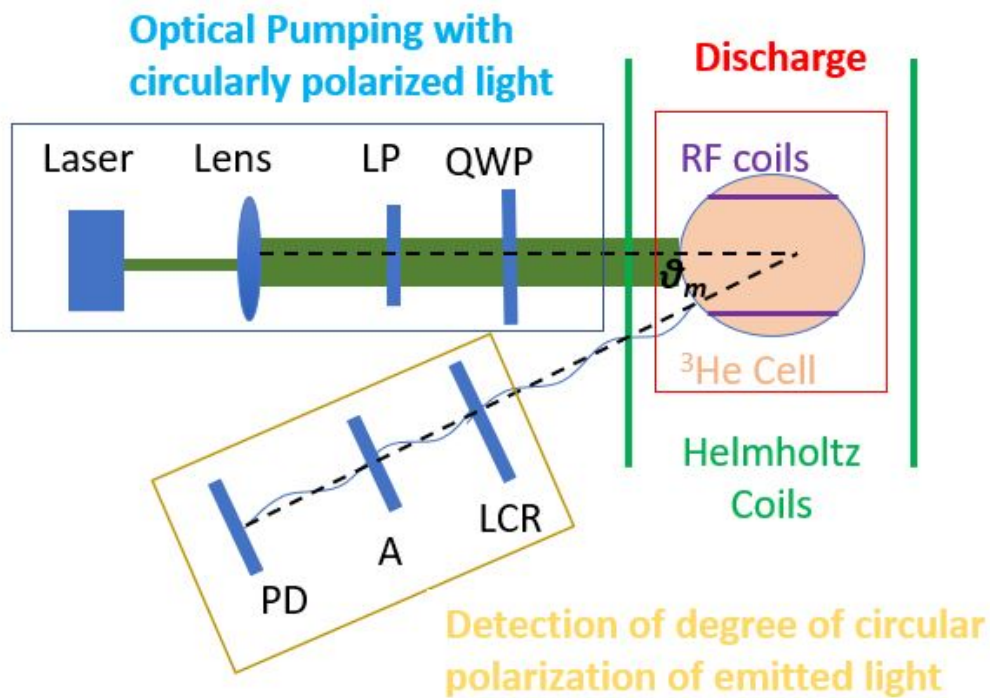


Figure 4.5: Measured ^3He absorption spectrum at low field with labels for each absorption line from Figure 3.2.

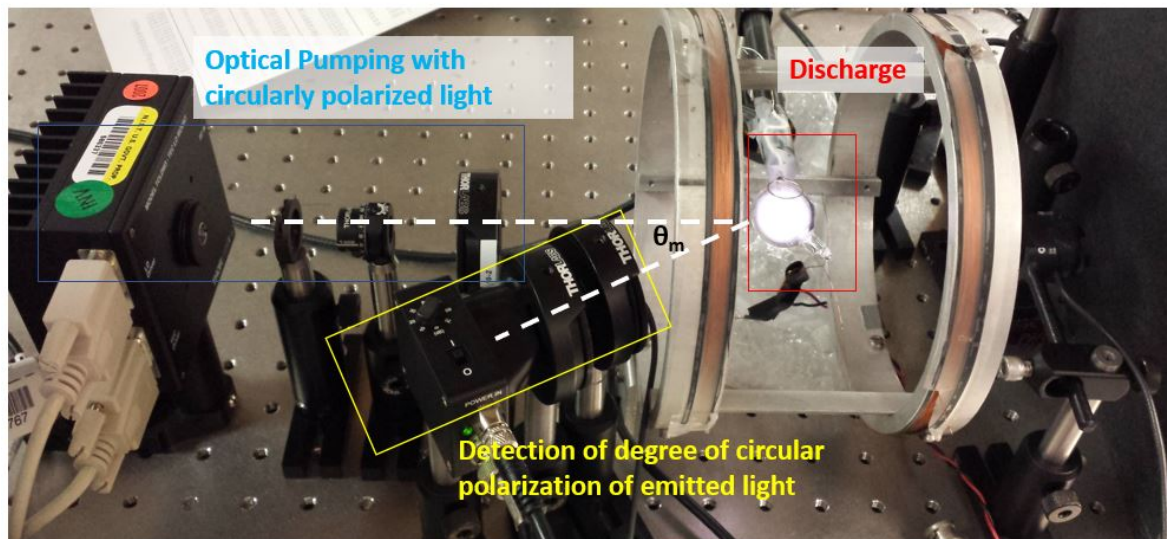
(LP) and a quarter wave plate (QWP) (Figure 4.6). The absorption step for MEOP could be checked with the transmission of an unpolarized beam through the sample cell and turning the B_0 field on and off. We saw the transmission power increase when the field was turned on as expected. The gas absorbed less light with the magnetic field on since the nuclei aligned with or against the field, instead of aligning with any random stray field present in the room, and hence absorbed only the σ_+ or σ_- component of the beam.

4.2.2 Polarimeter Design and Calibration

Once the laser hyperpolarized the gas via MEOP, the nuclear polarization could be determined by measuring the circular polarization of 668 nm light emitted in the discharge, as explained in Section 3.2 and reference [37]. We measured the circular polarization of this light with a polarimeter (based on [37]) consisting of a liquid crystal retarder (LCR), an analyzing linear polarizer (A), and a photodiode detector (PD), as shown in Figure 4.6. The LCR (Thorlabs model LCC11125-A) contains nematic liquid crystals which change their orientation based on an applied AC voltage, and this determines the retardance of the plate. By tuning the applied AC voltage with the Thorlabs controller (LCC25) connected to the LCR, we could tune the LCR to behave as a $\lambda/4$ or $3\lambda/4$ plate. Hence, a linearly polarized beam incident on the LCR would become left or right circularly polarized, while a circularly



(a) Diagram of experimental setup for MEOP.



(b) Picture of experimental setup for MEOP.

Figure 4.6: MEOP experimental setup diagram (a) and picture (b) showing: ^3He cell and discharge coils, optics for optical pumping, polarimeter, and Helmholtz coils.

polarized beam would become linearly polarized, at the correct applied voltage.

In order to determine these specific voltages, we calibrated the LCR by sending an already circularly polarized beam through the polarimeter. We used a 632 nm HeNe laser to be close to the wavelength of interest, 668 nm from ^3He emission, as the tuning voltages have a wavelength dependence. Later, this laser was replaced with a 10 mW diode laser at 670 nm (Thorlabs HL6748MG) for a more accurate calibration with current provided by a Thorlabs LDC500 controller. To perform the calibration, the light from the calibration laser was circularly polarized to nearly 100% by propagation through a linear polarizer (LP) and a quarter wave plate (QWP), and then incident on the polarimeter. Within the polarimeter, the beam was transmitted through the LCR, the analyzer, and was finally incident on a photodiode which measured the transmitted power. To eliminate signal from background light and other lines of the ^3He discharge, we also used an interference filter (F), Thorlabs FL670-10, to specifically select 670 +/- 2 nm light, in the setup right before the photodiode. Measuring this power as a function of the LCR voltage produced the calibration curve of the LCR, shown in Figure (4.7), which gave the relationship between applied voltage and plate retardance. Note that the minimum power for $\lambda/4$ was > 0 V due to unavoidable background light.

Since the LCR's slow axis and the analyzer's axis were set at a 45° angle from each other, the voltage values for the minimum and maximum points on this curve corresponded to $\lambda/4$ and $3\lambda/4$ wave plate settings, respectively. This is because for example in the case that a right circularly polarized beam was incident on the LCR tuned to $\lambda/4$, the polarization would change to linear in the vertical direction, and the beam would be completely blocked by the horizontal analyzer that followed. Similarly the beam passing through $3\lambda/4$ LCR would become horizontally polarized, giving a maximum power measurement on the photodiode after passing through the horizontal analyzer.

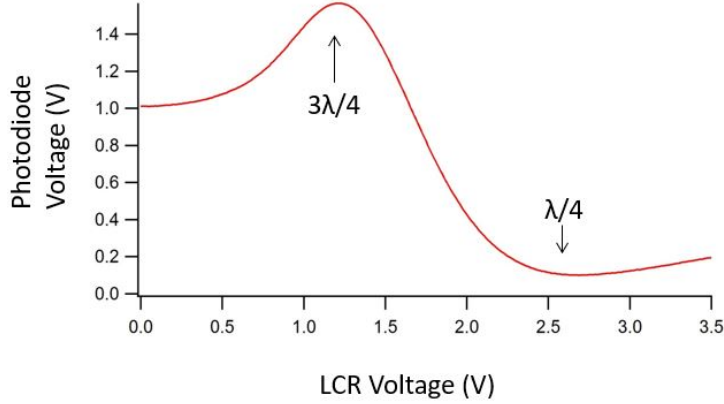


Figure 4.7: LCR Calibration Curve produced with 632 nm HeNe laser.

4.2.3 Measurement of Nuclear Polarization

Once the LCR was calibrated, we could use the polarimeter for ^3He . As shown in figure 4.6, we detected the 668-nm light from the discharge glow with the polarimeter placed at an angle θ_m from the incident optical pumping beam. For this measurement, the LCR voltage was modulated between $\lambda/4$ and $3\lambda/4$ at a frequency of 20.1 Hz controlled by an external function generator – SRS (Sanford Research Systems) Model DS345. Hence, the power measured by the polarimeter would oscillate between reading a maximum power and 0 V for a 100% circularly polarized beam. For a beam with some degree of polarization less than 100%, the difference in the two power measurements would then provide a measure of the degree of circular polarization.

The detector voltage was read out by an oscilloscope (Tektronix TDS 2024C) or a Lockin amplifier (SRS SR830), both of which used the 20.1 Hz function generator output for triggering/syncing. The ratio of the amplitude of the oscillating signal ($\Delta V = V_{max} - V_{min}$) detected at this reference frequency to the total signal with the background subtracted gave a relative measure of the degree of circular polarization of incident light. To get the absolute degree of this circular polarization, we divided this ratio by a calibration factor, determined

by making the same measurement ($\Delta V/V_{total}$) with the calibration laser:

$$P_{circ} = \frac{\Delta V_{^3He}}{V_{total,^3He} - V_b} \frac{V_{total,calib} - V_b}{\Delta V_{calib}} 100\%, \quad (4.1)$$

where $\Delta V_{^3He}$ and ΔV_{calib} are the voltage differences between the maximum and minimum transmitted power for ^3He and the calibration laser, respectively, V_{total} denotes the total measured voltage for each, and V_b is the voltage measured for the background light in the room. At this point, we also made a correction of $\cos(\theta_m)$ to account for the angle of the polarimeter from the incident beam, and multiplied by the pressure correction factor from [38] to calculate the nuclear polarization in the sample:

$$P_3 = P_{circ} \frac{f_p}{\cos(\theta_m)} \quad (4.2)$$

Here, P_3 is the nuclear polarization in ^3He and f_p is the pressure correction factor. Using this setup with $\theta_m \approx 45^\circ$ and $f_p = 10.1$ from [38] for 2 Torr gas, typical measured values were $\Delta V_{^3He} = 4$ mV, $V_{total,^3He} - V_b = 180$ mV, and $(V_{total,calib} - V_b)/\Delta V_{calib} = 0.95$. Plugging these into the above equation yielded measured nuclear polarization in the cells to be $\sim 32\%$.

4.2.4 Verification Tests

In order to verify that the observed signal resulted from the nuclear polarization of the gas, and not caused by something else, we performed the following tests:

- Detuned the laser wavelength off resonance (away from C_8 and C_9),
- Changed the polarization of the optical pumping beam (circular polarization to unpolarized beam),
- Turned off the laser entirely, and
- Turned off the magnetic field,

In each case, we saw the polarization signal disappear, except when a small residual polarization was seen after the magnetic field was turned off. In the case of laser detuning, beam polarization change, and beam turn off, we expected the signal to vanish as the gas sample was no longer being hyperpolarized. For the magnetic field test, a small remaining polarization was not surprising as this could have been caused by stray fields in the room. Additionally, we applied a quenching field by using an oscillating magnetic field (B_1) near the ^3He resonance frequency of 25.3 kHz, which would mix the populations of the magnetic sublevels and destroy the polarization. Indeed turning on this field, we saw the polarimeter signal reduce to 0.

4.3 Experimental Apparatus and Electronics for NMR

After the gas in the cell was hyperpolarized via MEOP, and the polarization was confirmed and measured with the polarimeter, the NMR technique could be employed to measure the magnetic field B_0 of the Helmholtz coils in which the cell sat. In other words, we could start using ^3He gas as a magnetometer at low field.

4.3.1 CW NMR

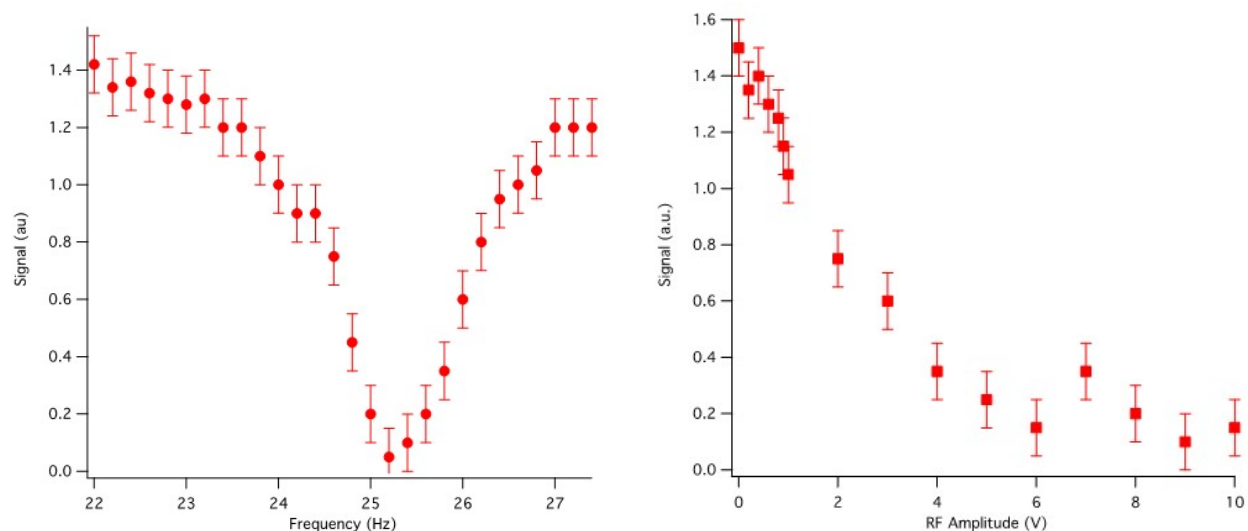
Using the Hall probe measurement of the field $B_0=7.8$ G defined along the z-direction and the ^3He gyromagnetic ratio = 3.24 kHz/G [25], the resonance (Larmor) frequency (see Section 3.3) was estimated to be $\omega/(2\pi) = f = \gamma B = 25.3$ kHz. We also measured this value with an RF coil orthogonal to B_0 to create an oscillating $B_1(t)$ field in the transverse plane along the y-axis (vertical in the lab), just as was done in the previous section. As the frequency of this field was tuned with a function generator (SRS DS345), the polarization signal from the gas decreased and reached a minimum at the resonant frequency. This is because at this point, the rotating field mixed the magnetic sublevel populations in the 2^3P state, hence destroying the polarization. Figure 4.8a shows the data yielding a resonant frequency of 25.2

kHz, which agreed well with our calculation.

We performed another check of this frequency measurement by monitoring the power of the transmitted optical pumping beam, which increased at the resonant frequency. This indicated that less light was being absorbed by the sample due to state mixing, verifying the Larmor frequency value. Lastly, we slowly increased the amplitude of $B_1(t)$ at the resonant frequency, and the polarization signal decreased (Figure 4.8b) as expected, since the increasing field strength caused a larger effect on the polarization.

4.3.2 Pulsed NMR

Before implementing pulsed NMR, we improved the setup by replacing the small set of Helmholtz coils (7 cm radius) which created B_0 with a larger set of coils (25 cm radius). The assumption here was that the larger coils would produce a more uniform field while the smaller coils gave rise to larger field gradients, which would greatly reduce the length of the NMR FID signal (T_2^*) as discussed in Section 3.3. A current of 27.9 A was applied with a Kepco power supply to larger HH coils and produced a field of 25.8 ± 0.2 G as measured



(a) Polarization signal amplitude reaches a minimum at the resonant frequency. (b) Polarization signal amplitude decreases when field strength is increased at resonance.

Figure 4.8: CW NMR studies at low field. The error bars are due to voltage measurements of polarization signal, uncertainty of cell pressure, and polarimeter calibration.

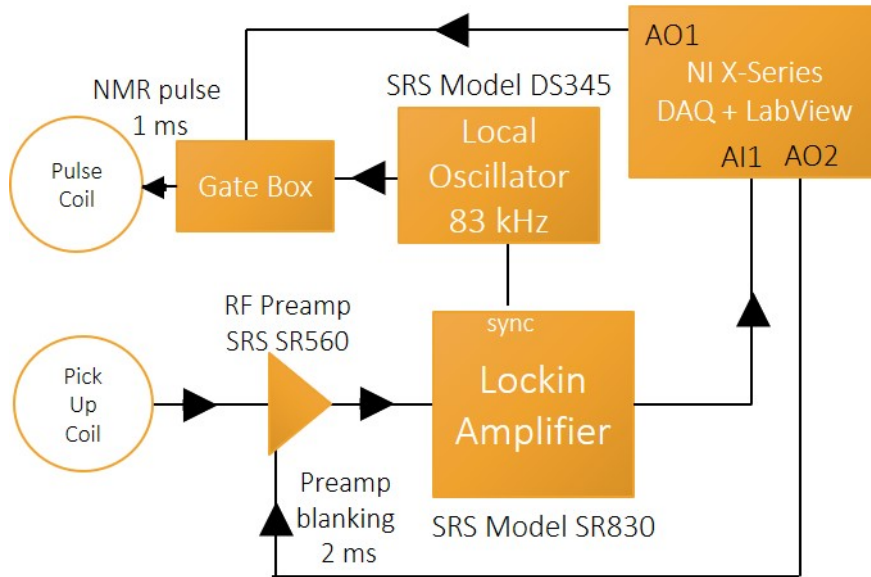


Figure 4.9: Electronics diagram for low field NMR.

by a Hall probe. Hence the Larmor frequency used for NMR with these coils was 83.6 kHz.

The electronics diagram for pulsed NMR setup is shown in Figure 4.9. Two RF coils were used, one for excitation (pulse coil) with 3 turns and a 1.5 cm radius, and another 180-turn coil with a 1.75 cm radius for picking up the signal. Both coils were placed approximately perpendicular to each other with their axes aligned in the x- and y-directions so both were orthogonal to the magnetic field produced by the Helmholtz coils (z-direction). A 0.7 cm thick cylindrical aluminum shield was placed around the entire setup (^3He cell, discharge coils, and NMR coils) to reduce electrical noise, as discussed below. The NMR pulse sent to the pulse coil was gated by a CMOS switch (labeled Gate Box in diagram) controlled by an analog output on a National Instruments (NI) X-Series USB 6363 data acquisition (DAQ) box controlled by an NI LabVIEW program. The switch determined the width of the NMR pulse (1 ms), while the 83.6 kHz frequency was provided by a function generator (SRS DS345) – the local oscillator (LO) – with a 10 V amplitude.

The NMR precession created in the sample was then picked up by the secondary coil as an induction current and the resulting voltage was sent to a preamplifier (SRS SR560), which served as a bandpass filter to remove noise between 10 kHz and 1 MHz and amplified

the signal with a gain of 1000. This signal was read by a lock in amplifier (SRS SR830) with a 1 ms time constant and an additional gain of 100, which used the frequency from the local oscillator as a reference, and acting as a mixer and a bandpass filter, mixed it with the signal frequency. The mixed down signal was input to the NI DAQ analog input channel. After a 2 ms blanking pulse sent to the pramp with an NI output channel to avoid overloading the device, the signal was read and saved by the LabVIEW program for ~ 50 ms. This was the final configuration developed for the low-field pulsed NMR shown in Figure 4.9. A number of investigations and improvements, described below, led to this setup, including implementation of the blanking pulse and addition of the aluminum shield.

To ensure our electronics and experimental setup were well-suited to read the signal we searched for, we first estimated the size of the NMR signal making some basic assumptions. The ^3He nuclei precessing at the frequency $\omega = 2\pi(83.6 \text{ kHz})$ would produce a magnetic field B_3 proportional to the magnetization in the sample:

$$\vec{B}_3(t) = \frac{\mu_0}{4\pi} M \sin(\omega t + \phi) \quad (4.3)$$

The magnetization would be given by:

$$M = P_3 [^3\text{He}] \mu_3 \quad (4.4)$$

where P_3 is the polarization of the gas (measured at $\sim 30\%$), $[^3\text{He}]$ is the density calculated using the ideal gas law ($PV = NkT$) at 2 Torr pressure and room temperature for the 1 cubic inch cell volume, and μ_3 is the permeability of the gas, calculated by multiplying the known permeability of water by the ratio of the gyromagnetic ratios [27], and another factor to correct to Torr ($760 \text{ Torr} = 1 \text{ atm}$): $\mu_3 = \mu_{\text{water}}(\gamma_3/\gamma_{\text{water}})/760$.

The flux created by this field would produce an EMF ε in the pick up coil with area $A = \pi r^2$ ($r = 1.75 \text{ cm}$) as determined by Faraday's law: $\varepsilon = -d\Phi/dt = -AdB/dt$. Hence, the

maximum ε would be:

$$\varepsilon_{max} = \frac{\mu_0}{4\pi} M\omega A = \frac{\mu_0}{4\pi} P_3[{}^3He] \mu_3 \omega \pi r^2 \quad (4.5)$$

The final result is attained after multiplying by three more factors:

- N , the number of turns of the coil, which is calculated using the inductance $L = \mu_0 N^2 A/l$, where A and l are the inner core area (radius=1.5cm) and length (0.8 cm) of the coil, respectively, and L can be determined using the relationship of the resonance frequency to the inductance of the coil: $\omega_0 = 1/\sqrt{LC}$, where $C = 10\text{nF}$. The calculation yields $N = 174$ turns.
- the Q of coil. This is measured by first determining the resonant frequency of the coil, f_0 , then tuning the frequency until the signal amplitude is $\sqrt{2}$ times the amplitude at f_0 , which occurs at two frequencies, one lower and one higher than f_0 . We then use the difference of these two frequencies ($\Delta f_{\sqrt{2}}$) to calculate $Q = f_0/\Delta f_{\sqrt{2}} = 19.6$.
- the filling factor f , which is a measure of the efficiency of the coil, i.e. the percent of the B_3 field created by the nuclei that is picked up by the coil. We estimated $f \approx 0.2$.

Putting this all together gave the final estimate for the amplitude of the NMR signal with 30% gas polarization: $0.26 \mu\text{V}$.

We found that the electrical noise in the setup was much higher than this number. To study this noise in more detail, we hooked up the NMR system to a spectrum analyzer (SRS Model SR760) and observed the frequency resolved spectrum of this noise. In addition to expected 60 Hz noise, we observed a broad peak at 83.5 kHz with an amplitude of $500 \mu\text{V}/\sqrt{Hz}$, as well as background noise levels greater than $100 \mu\text{V}/\sqrt{Hz}$ present at all frequencies. We attributed the 83.5 kHz noise peak to ringing of the pick up coil due to the excitation pulse being close to coil resonance. To eliminate the background noise, we placed a cylindrical aluminum shield (0.5 cm thick) around the sample cell and NMR coils, and changed the grounding scheme by grounding the shield and signal cable instead of the

pick up coil electronics box as was done previously. This resulted in the background noise reducing to $10 \mu\text{V}/\sqrt{\text{Hz}}$. However, the 83.5 kHz noise peak remained. This, of course, was expected due to the resonance of the coil.

Another issue in the electronics was that the preamplifier between the pick up coil and lockin was overloading when attempting to read the signal, likely due to the excitation pulse leaking into the pickup. To solve this issue we implemented a blanking pulse so that the preamp would start reading data 1 ms after the excitation pulse (also 1 ms long) ended. The same LabVIEW program and NI DAQ box in Figure 4.9 were used to control the length and timing of this pulse sent to the preamplifier. Lastly, the preamp was set to measure in low-noise mode, with a high-pass filter of 10 kHz, a low-pass filter of 1 MHz, and a gain of 1000. Once these changes were implemented, we observed NMR signals with amplitudes in the range of 0.5-1 V. Taking the preamp gain (1000) and lockin gain (100) into account, the signal created by ^3He nuclei precession was $\sim 0.1 \mu\text{V}$, which is 2-3x smaller than our predicted value, probably due to a combination of effects including the estimated filling factor.

4.4 Low Field NMR signal and studies

The NMR signal was measured and stored using LabVIEW and analyzed in Matlab. The Free Induction Decay signal was modeled as a decaying sinusoidal wave, with a decay constant T_2^* . The function used to fit the data in Matlab was:

$$V(t) = A + B\cos(\omega t + \phi)\exp(-t/T_2^*) \quad (4.6)$$

where A is an offset, B is the signal amplitude, $\omega = 2\pi f$ is the mixed down frequency, ϕ is the phase, and T_2^* is the transverse relaxation time discussed in Section 3.3. All five of these parameters were extracted from the fit in Matlab, which used the average amplitude of data from a noise run for the weighting. See Appendix A for a discussion of the fit model. Figure 4.10 shows a sample FID signal fit to the above equation, with the fit frequency measured

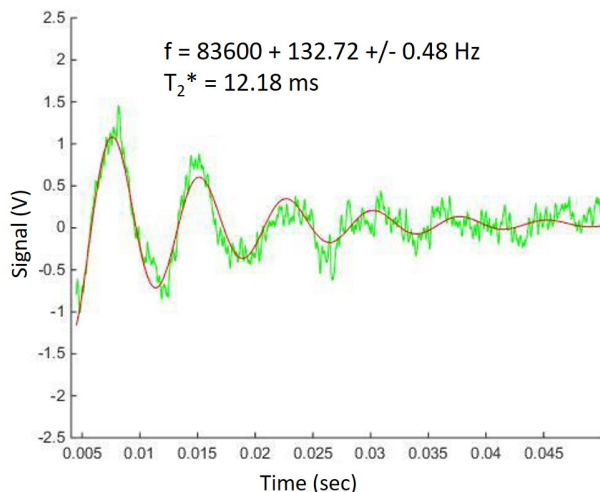


Figure 4.10: ^3He NMR FID signal at low field.

to 5 ppm ($f = f_{LO} + f_{mix} = 83600 + 132.72 \pm 0.48$ Hz). The average T_2^* of the signal was about 10 ms.

4.4.1 Studies of signal

The following studies were completed to gain a better understanding of the signal and determine the experimental procedure limits that produced the signal:

- The polarization time for MEOP was varied to identify the minimum time needed to produce an NMR signal via MEOP. A signal was seen for as short as a 5-second polarization time for this qualitative study (Figure 4.12).
- The time between turning the discharge off and firing the NMR excitation pulse was varied. Since the discharge being turned off marks the end of the polarization process, after which the polarization decays, this study gave a measure of T_1 , or how long the NMR signal lasts once the sample is polarized. The signal amplitude was plotted as a function of the time between polarization and NMR (Figure 4.13), and fit to an exponential ($\propto e^{-1/T_1}$), yielding a T_1 of 30 ± 5 seconds.
- MEOP and NMR were performed on two different cells. The cell with the longer

stem had a shorter T_2^* and a slightly larger frequency (Figure 4.14). This matched expectations as we predicted that the nuclei in the stem as well as the glass stem itself (due to diamagnetism of glass) created a dipole field, increasing the measured frequency. Note depending on the orientation of the stem, the frequency could also decrease. The stem as a dipole model is discussed further in Chapter 6. We also expected the longer stem to create higher gradients yielding a shorter T_2^* .

- Significant variations of signal size, frequency and T_2^* were observed due to changes of the field and gradient in the room. For example during one signal study, we noticed a shorter T_2^* (~ 7.8 ms vs. ~ 10.4 ms) and a 20 Hz shift in the frequency (Figure 4.15). After some inspection, we realized that a metal chair had been brought near the set up. While this was an accidental discovery, it showed the incredible sensitivity of the ^3He magnetometer.

Lastly, we replaced the coax cable connected to the pick up coil in the setup with a twinax cable. After this change was implemented, we observed increased T_2^* time of the signal from 10 ms to 300 ms. While data was not recorded for these measurements, a screenshot of the FID read by the LabVIEW program is shown in Figure 4.11.

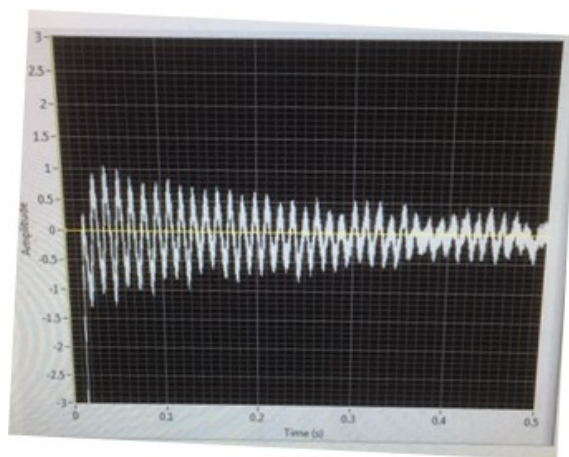


Figure 4.11: Longer $T_2^* = 300$ ms measured after switching to twinax cable.

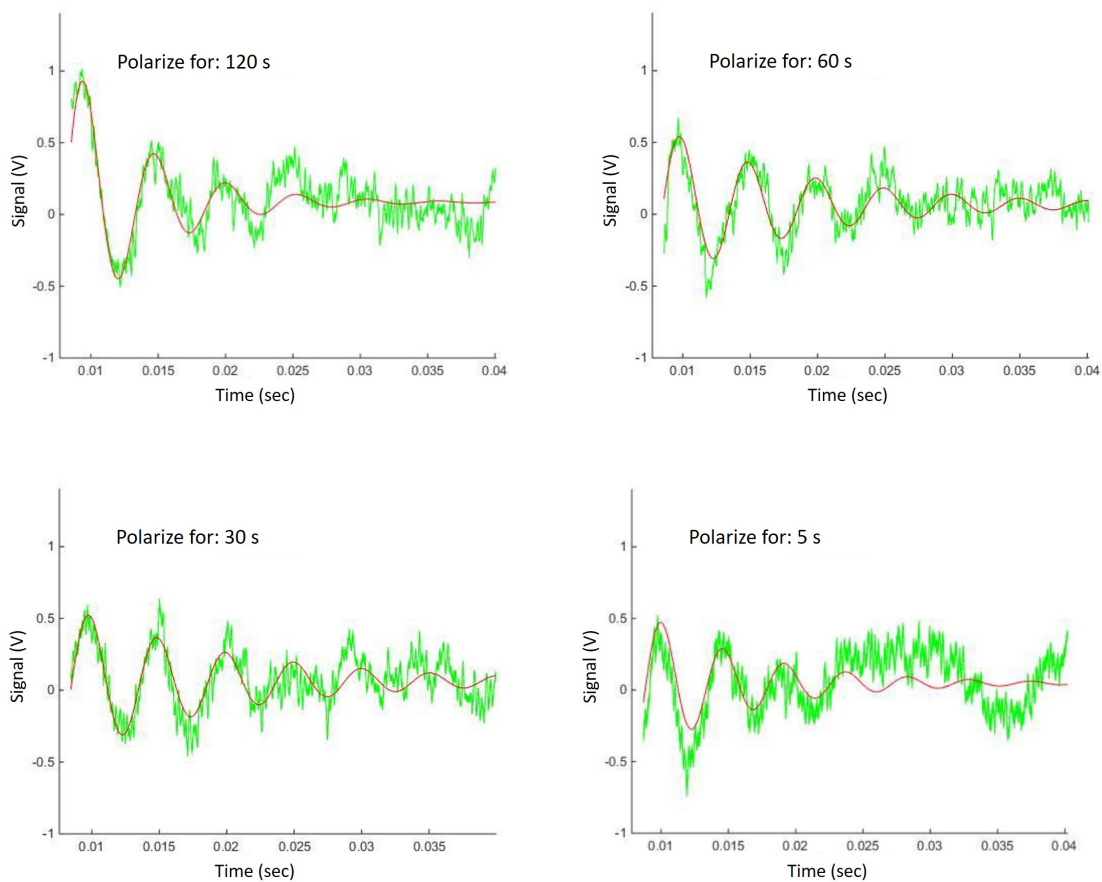


Figure 4.12: FID signals after varying polarization time: 5 seconds to 120 seconds.

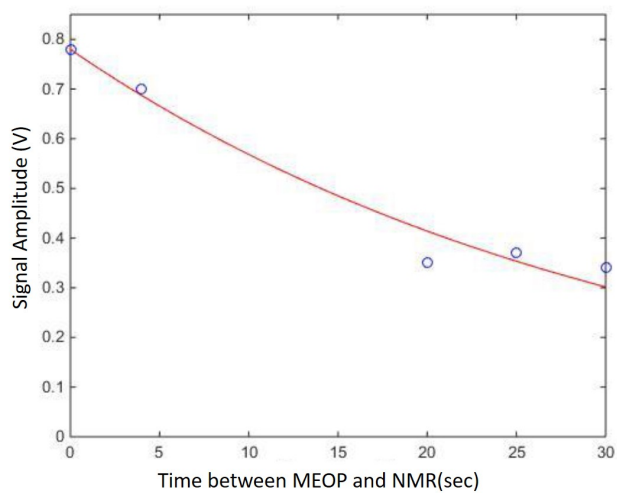


Figure 4.13: ^3He NMR FID signal amplitude decay as a function of time between polarization with MEOP and NMR measurement giving a measure of the T_1 relaxation time.

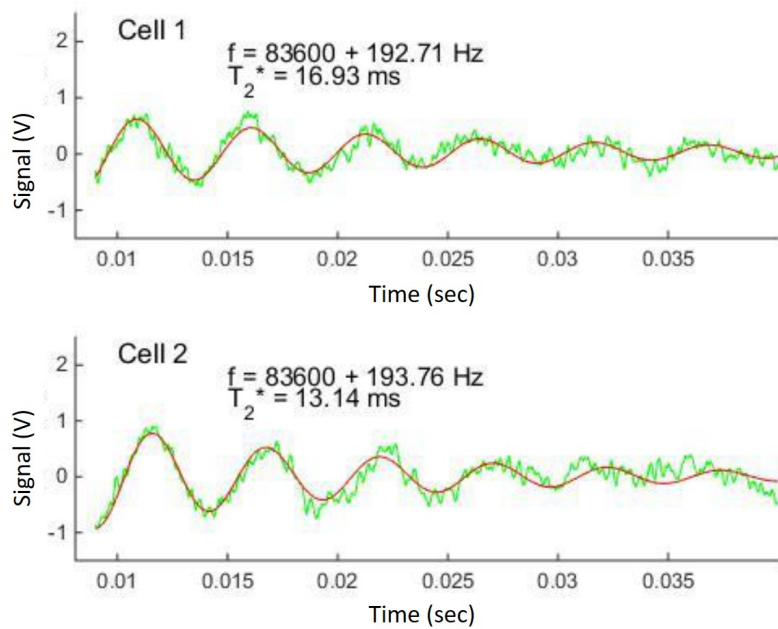


Figure 4.14: ^3He NMR FID signal for different sample cells.

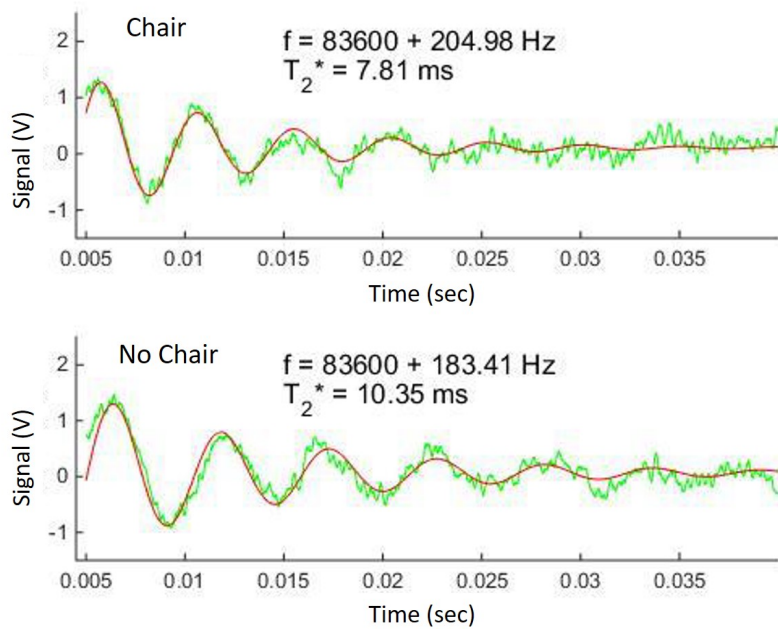


Figure 4.15: ^3He NMR FID signal with and without a chair near the setup.

Chapter 5

High Field MEOP and NMR

The theory of high field MEOP and NMR are described in Chapter 3, where we also provide references of comprehensive high field MEOP studies [1], [39], [40], [35]. In this chapter, we provide the details of the high field experimental setup and procedure followed by ^3He probe studies in high field.

5.1 Changes for High Field

We moved the ^3He magnetometer from the University of Michigan's low field Helmholtz coils to a high field magnet facility at Argonne National Lab. In addition to the magnet, we also incorporated a higher power laser and modified the probe materials to be more suitable at high fields.

5.1.1 Magnet

A superconducting MRI magnet shown in Figure 5.1 was recycled from a medical facility and brought to Argonne National Lab to test and calibrate various magnetic field probes for the Fermilab muon g-2 experiment (E989). The magnet has a 68 cm cylindrical bore and is capable of producing a magnetic field between 1-4 Tesla along the axis of the cylinder



Figure 5.1: High field superconducting MRI magnet at Argonne National Lab.

controlled by the current in the superconducting coils (400-500 Amps). The magnetic field strength used was 1.45 T, the same as the E989 magnet, for all high field magnetometry performed at Argonne and described in this work. The Argonne team iteratively distributed small sheets of iron near the inner bore of the magnet to maximize field homogeneity passively. Additionally, the magnet contains “active” coils, which could be turned on and off on a short time scale (few seconds). The currents through these coils actively create linear and higher order gradients within the magnetic field in all three directions and can be used to improve field homogeneity to ~ 9 ppb/mm. Since the magnet is superconducting, the temporal stability is also very good, with field drifts of < 10 ppb/hr achieved.

5.1.2 High Power Laser

As described in section 3.2.2, the weaker hyperfine coupling of the ^3He energy sublevels at high fields (> 0.1 T) makes it harder to achieve nuclear polarization in the sample, which must be compensated for with a higher power laser. As the Zeeman splitting of the energy levels also increases, the laser must be tunable over a wider energy range. We thus acquired a Keopsys laser (CYFL-GIGA-02-LP-1083-WT1-FM1-ST1-OM1-B206-F1) [49] specifically built for our setup with the following features:

- Power emission between 100 mW to 2 W,
- Central wavelength at 1083 nm,

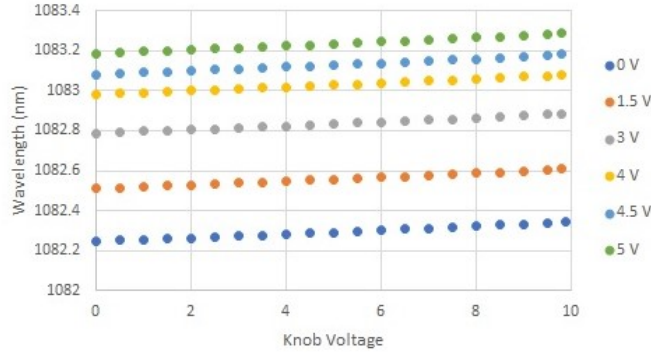


Figure 5.2: Wavelength tuning of Keopsys laser at different external voltages.

- Spectral linewidth 2 GHz
- Tunable over entire ^3He absorption spectrum (200 GHz),
- A single-mode fiber for beam output (linearly polarized),
- 5 meter long output fiber, so that the laser electronics could be placed outside the high magnetic field range,
- Fiber output with ceramic ferrule, instead of metal parts (to minimize material effects on magnetic field measurement), except for a small 2-mm thick metal clip.

The laser wavelength could be controlled with an external power supply for coarse adjustments and a knob on the laser for finer adjustments. Figure 5.2 shows the range of wavelengths measured by applying different external voltages and tuning the laser knob. These scans were taken by measuring the wavelength with a wavemeter (HighFinesse GmbH WSU [50]) at University of Michigan.

The laser was then transported to Argonne National Lab, and due to safety requirements, the fiber and beam were always enclosed in a mount (see section 5.1.3) during operation. We found the ^3He absorption lines relevant for MEOP at 1.45 T by measuring the absorption of the laser through the cell with the discharge on. As the laser wavelength was scanned by changing the external applied voltage and knob voltage, the power of the transmitted beam was measured either directly on a Thorlabs Detector (FDS10X10) or using a multimode

Absorption Line	Ext. Voltage	Knob Setting
f_2^-	4.05 V	6.68
f_4^-	4.05 (or 4.3) V	8.78 (or 4.00)
f_4^+	4.3 V	3.84
f_2^+	4.3 V	1.50

Table 5.1: Laser voltage settings for ^3He absorption lines at 1.45 T.

fiber with a ceramic ferrule (Thorlabs PM780-HP Custom, 5 m). Both of these devices were connected to a voltmeter which displayed voltages proportional to the power of light incident on the detector or fiber. The four measured absorption dips were labeled f_2^- , f_4^- , f_4^+ , and f_2^+ based on comparison with the ^3He absorption spectrum from [1] shown in figure 3.3b. Table 5.1 gives the laser voltage settings for each absorption line found through these scans.

5.1.3 3D Printed Mount

We designed a mount to be 3D printed with polylactic acid (PLA) plastic using SOLIDWORKS software [51]. The motivation for 3D printing was to use low-susceptibility materials to construct the ^3He magnetometer to minimize field perturbations and have control of small design elements with specific shapes. The ~ 4 mm resolution of the 3D printed pieces is hard to achieve with machined parts, which can also accumulate ferromagnetic residue from the machine tools. The mount was a rectangular prism with a 5 x 5 cm cross section, and a length of 16 cm, printed as two halves which fit nicely into each other as one contains slots and the other contains wedges (see Figure 5.3a).

The mount contained specific slots for all of the optics needed for MEOP - the laser fiber ferrule, the absorption fiber ferrule, linear polarizer, and quarter wave plate, as well as the sample cell, discharge coils, and the NMR coil as shown in Figure 5.4. The laser fiber was inserted into a hole located at the center of a circular disk made with nylotron, and this disk was inserted into the left-most slot in the mount, 1.5 cm from the left-most edge. The fiber ferrule reached about 0.5 cm beyond the nylotron disk. About 2.6 cm from the laser fiber was another slot intended for the linear polarizer (LP). However, we determined that the

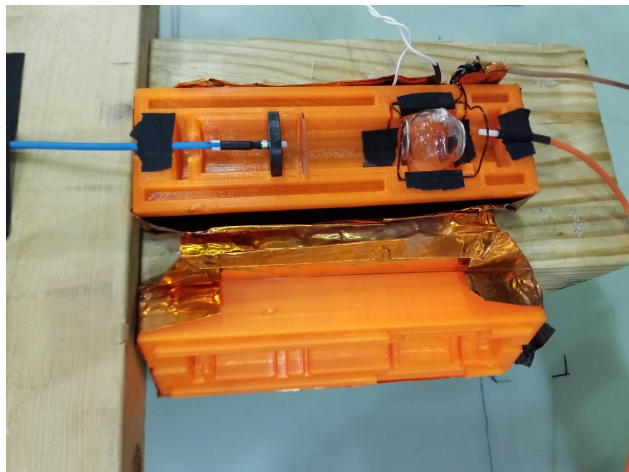
linear polarizer was unnecessary once the polarization axis of the fiber was found since the output beam was already linearly polarized. The quarter wave plate (QWP) was mounted in a slot 0.75 cm away from the intended LP position.

The center of the ^3He cell was located about 9.1 cm from the laser fiber. Figure 5.3b shows the fiber mounted closer to the cell (6cm away) in the linear polarizer slot, because the placement of the fiber had not been finalized at the time this picture was taken. The additional distance between the fiber and cell allowed for the beam to expand to about a 2 cm diameter, covering more of the 2.5 cm height of the cell. Around the central location of the cell, the top half mount had slots cut out for the discharge coils to be inserted and placed around the cell 1.4 cm apart.

There were several iterations of the probe mount, and the final design shown in Figure 5.5 also included slots on the top and bottom halves of the mount for the NMR saddle-shaped coil (see section 5.1.5) located 3.65 cm from the quarter wave plate. Lastly, on the side of the mount opposite to the laser fiber was a slot for the absorption fiber (or photo detector for earlier versions of the mount). Both the absorption fiber and the NMR coil were inserted into the slots of the mount and held fixed with 1 cm pieces of masking tape. The slot next



(a) 3D printed mount for ^3He probe: top and bottom halves.



(b) 3D printed mount with MEOP optics, cell, NMR coil, and discharge coils inserted.

Figure 5.3: 3D printed probe mount for high-field magnetometry.

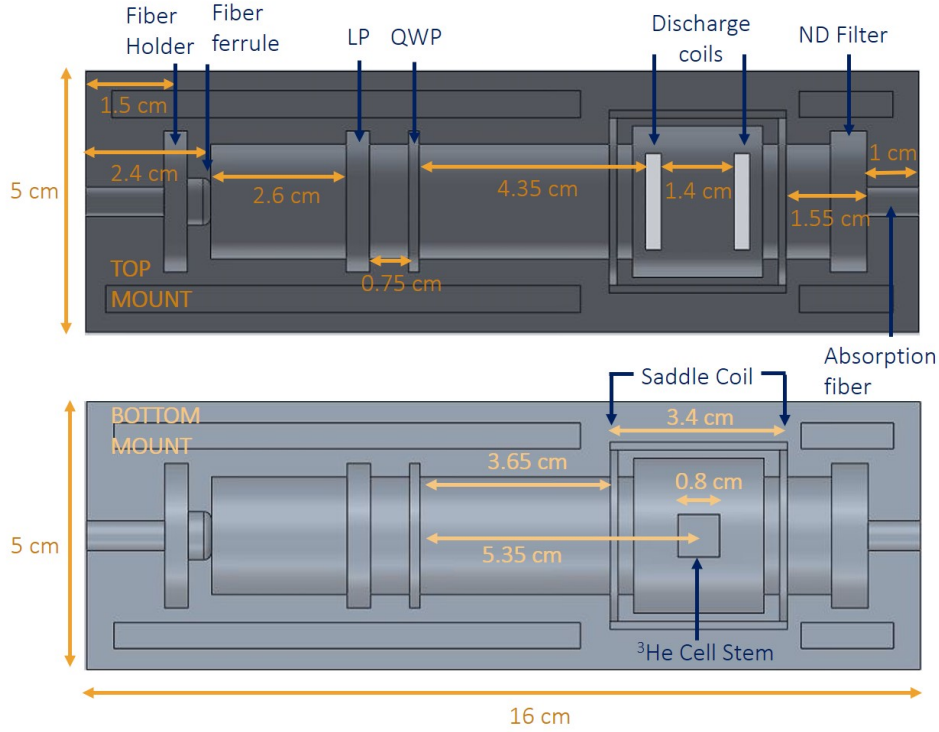


Figure 5.4: Locations of optics, saddle coil, and ^3He cell in 3D printed probe mount.

to the absorption fiber was intended for a neutral density filter in case the light from the ^3He discharge needed to be blocked out in favor of the laser. However, the absorption fiber signal from the laser light was much higher than noise, and the filter was not needed.

5.1.4 Discharge Coils and Shielding

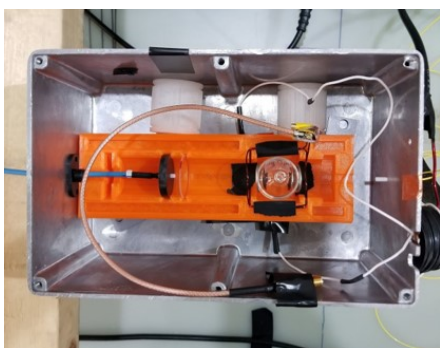
Due to safety regulations at Argonne National Lab, the transformer and the discharge coils had to be placed in a metal box to attenuate radio frequency (RF) radiation emission. We initially used a 18.3 cm x 8.1 cm x 11.9 cm rectangular aluminum box (see Figure 5.5a) and inserted the entire ^3He setup, including the 3D printed mount and transformer, into the box. However, in an effort to use less materials, specifically to eliminate aluminum in the apparatus, we lengthened the wires from the transformer to the discharge coils by about 10 cm, and placed the transformer in a smaller aluminum box (~ 6.4 cm x 5.8 cm x 3.5 cm). This allowed the shielded transformer to be placed 10 cm away from the ^3He cell and hence the

effect (or perturbation) on the magnetic field measurements was reduced. We then wrapped a 0.08 mm thick copper shield around the 3D printed ^3He mount for protection from RF radiation and to eliminate electrical noise for NMR measurements (see Figure 5.5b).

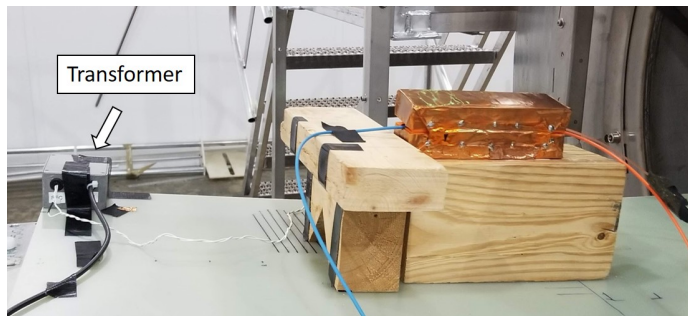
We also found when testing MEOP in the magnet that only one orientation of the discharge coils reliably struck a discharge in the cell. When the coil axes were parallel to the magnetic field, the discharge turned on, however when the coils were placed perpendicular to the field, they were often unsuccessful at striking a discharge. When the same tests were performed in the fringe field of the magnet, the discharge turned on independent of the coil orientation. We slid the cell from the fringe field to the higher field area of the magnet and observed that the discharge turned off when the coil axes were perpendicular to the field axis and remained on when they were parallel. Hence the discharge coils were mounted with the plane of the coils perpendicular to z (coil axes parallel to \vec{B}) for all high field measurements discussed in this work.

5.1.5 NMR Coil: Saddle Coil

A circular coil with area A , N turns, and length l has inductance $L = \mu_0 N^2 A/l$. If a capacitance C is added, the LC circuit frequency is given by $\omega_0 = 1/\sqrt{LC}$. Combining the



(a) ^3He Probe in metal box.



(b) Probe with copper shield after transformer is moved away (shown on left).

Figure 5.5: Before and after removing aluminum box.

two we have:

$$\omega_0^2 = \frac{l}{\mu_0 N^2 AC}. \quad (5.1)$$

This shows that the frequency of an NMR coil is inversely proportional to the number of turns. Moving from low field to high field, the NMR frequency of ^3He nuclei changes by 3 orders of magnitude ($(2\pi)83$ kHz to $(2\pi)47$ MHz). Since our low field coil had less than 200 turns, the high field NMR coil could only be allowed to have 1 or 2 turns to compensate for the 3 orders of magnitude change in field.

On the other hand, from Section 5.1.5, the FID signal voltage picked up by such a coil is given by:

$$\varepsilon_{max} = \frac{\mu_0}{4\pi} M\omega ANQf, \quad (5.2)$$

implying that the signal is directly proportional to the number of turns in the coil. While the smaller N potentially reduces the signal size, the signal amplitude is also proportional to the NMR frequency ω which increases by 3 orders of magnitude as previously mentioned. While these effects almost cancel out, we aimed to increase all factors contributing to the signal size (and the signal-to-noise ratio SNR). Specifically, we focused on the filling factor f of the coil which is a measure of its efficiency, determined from the proportion of the NMR signal picked up by the coil to the total signal generated by the precessing nuclei ($f = \int_{sample} B_1^2 dV / \int_{all-space} B_1^2 dV$).

At low field, we used a circular coil placed 1 cm away from the ^3He cell, so the coil picked up the nuclei precession from only one side of the cell, which lowered its filling factor. If we had placed the coil right around the cell, the filling factor would be much larger. This discrepancy was taken into account when the signal size was estimated for low field in the previous chapter. To maximize this filling factor for high field, any circular NMR coil would thus have to be placed directly around the cell. To do this we would have to align the coil axis perpendicular to the magnetic field as is needed for NMR with the coil itself placed in the x-z or y-z plane. In either case the coil would block the optical pumping beam and

MEOP would not be possible. To avoid this issue, we instead used a saddle shaped coil as is common for NMR applications, for example see [52]. Figure 5.6 shows the drawing and photo of a prototype coil, which consisted of four 1.1 cm radius arcs connected by four 3.4 cm long straight wires. When current (direction indicated with orange arrows) runs through the coil, the field due to the arcs cancel and the field due to the straight wires add up (field direction indicated with blue arrows).

Since there are four wires, two on each side, with the flow of current opposite on each side, we see from the right hand rule that the field created is either up or down (down in the case of the current flow shown in 5.6a) in the center of the coil and orthogonal to the horizontal wires. Hence the field is generated from the 2 sets of 2 wires making this a 2-turn coil. Figure 5.6b shows an actual photo of a prototype saddle coil which was first constructed for testing with 16 AWG wire. We later used a different coil designed with the same basic principle but using 20 AWG magnet wire (CNC Tech model MW35-C HV) and non-magnetic capacitors.

The saddle coil was placed around the ^3He cell so that the straight wires were oriented along the z-direction on either side of the cell, producing the oscillating field $\vec{B}_1(t)$ from the NMR pulse in the + or - y direction. The arcs on either side of the cell were oriented in the y-z plane, and since the wires curve up and down, they allowed space for the optical pumping beam. Hence polarization via MEOP remained possible while the filling factor was maximized since the coil wires were placed on both sides of the cell. The same geometry allowed the horizontal wires of the coil to pick up the induction current from the field created by ^3He nuclei precession following the NMR pulse as the nuclei precession was in the x-y plane (orthogonal to the B-field along the z-axis).

As discussed earlier, the saddle coil frequency must be tuned to 47 MHz in order to be used for ^3He NMR. We measured the inductance of the coil with an inductance meter. For a coil with 3.4 cm long straight wires, and 2 cm radius arcs, the inductance was measured to be $0.36 \pm 0.1 \mu\text{H}$. The circuit used for tuning the coil is shown in Figure 5.7, where we treat the coil with some inductance L and resistance R , and place it in parallel with



(a) Saddle coil drawing: current direction indicated with orange arrows, magnetic field direction in blue. (b) Photo of first saddle coil with tuning capacitors soldered on.

Figure 5.6: Saddle Coil design and photo.

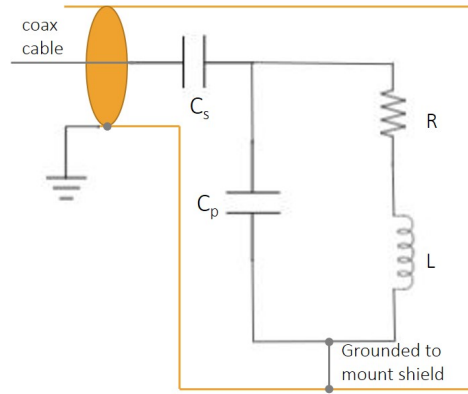


Figure 5.7: Circuit for tuning and impedance matching saddle coil.

a capacitor C_p , which determines the resonance frequency. This circuit, which we call the tuning circuit, is then connected in series with a capacitor C_s for impedance matching. In order to determine the capacitance needed for resonance at 47 MHz, we analyze the circuit and impedance match [53].

Using $Z_R = R$, $Z_L = iX_L = i\omega L$ and $Z_C = -i/(\omega C) = -iX_C$, we compute the impedance of the tuning circuit with L , R and C_p :

$$Z_{1,(R-L)} = R + iX_L, \quad Z_{2,(C_p)} = -iX_{C_p} \quad (5.3)$$

$$Z_{tuning} = \frac{Z_1 Z_2}{Z_1 + Z_2} = \frac{R X_{C_p}^2}{R^2 + (X_L - X_{C_p})^2} - i \frac{R^2 X_{C_p} + X_L X_{C_p} (X_L - X_{C_p})}{R^2 + (X_L - X_{C_p})^2} \quad (5.4)$$

Plugging in the impedances, we find:

$$Z_{tuning} = \frac{R}{(R\omega C_p)^2 + (\omega^2 L C_p - 1)^2} - i\omega \frac{L - \omega^2 L^2 C_p - R^2 C_p}{(R\omega C_p)^2 + (\omega^2 L C_p - 1)^2} \quad (5.5)$$

From here, we must apply two conditions:

1. Impose that the total impedance $Z_{tot} = Z_{tuning} + Z_{C_s}$ has no imaginary component by requiring that the impedance of the series capacitor is equal and opposite to the imaginary part of Z_{tot} : $Im(Z_p) = -X_{C_s} = 1/(\omega C_s)$. This gives a value for C_s
2. Impose that the total impedance is 50 Ohms \rightarrow Set the real part of Z_{tot} to 50 and solve for the zeros of the resulting quadratic equation. This gives a value for C_p

Plugging these equations into Matlab, we find that for a 0.4 μ H inductance coil with an estimated resistance of $R = 0.5\Omega$, we need: $C_p = 26$ pF and $C_s = 2.8$ pF. In practice we must use variable capacitors so we can tune the frequency of the coil with C_p and match to 50Ω by tuning C_s . We used two trimmer capacitors from Knowles electronics tunable from 0.6-12 pF range, one as C_s and the other in parallel with a 22 pF capacitor (also manufactured by Knowles) so the tunable range was 22.6-32 pF. All three capacitors were lead-free and non-magnetic so that their effect on the magnetic field measurement was minimized. This circuit was grounded to the copper shield placed around the ^3He probe as indicated in Figure 5.7.

Once the circuit was built, we used an Agilent network analyzer (model E5061 B ENA series) to tune the coil to 47.01 +/- 0.01 MHz, with impedance of 50 +/- 2 Ω using the tuning function on each capacitor.

5.2 NMR Studies with UW Electronics

5.2.1 UW NMR Electronics

All initial NMR studies were conducted using electronics from University of Washington designed for proton based NMR probes. We switched out a 61 MHz bandpass filter used for proton NMR and replaced it with a filter at 47 MHz (mini-circuits BPF-B48+) to make the electronics usable for ^3He . The UW electronics consisted of two boxes, a NIM box and a multiplexer, with the following functionality (also diagrammed in Figure 5.8):

- the NIM box:
 1. creates the NMR output pulse using a reference and sends it to the multiplexer based on an input trigger signal, and
 2. digitizes the incoming FID signal from the multiplexer after mixing it down with the reference frequency

- the multiplexer:
 1. selects the probe channel (The device is capable of switching between multiple channels and can be used to control multiple NMR probes. For the purposes of this work, only one channel was needed for the ^3He probe),
 2. sends the output NMR pulse from the NIM box to the probe, and
 3. reads the incoming signal from the probe and sends it to the NIM box

We used the UW electronics in conjunction with two function generators and an oscilloscope. One function generator (SRS DS345) was used to send a TTL pulse to the NIM box to trigger the NMR pulse and controlled the timing so the NMR pulses were gated at 1.037 Hz. Another function generator, the local oscillator, (SRS SG382) set at 47.0141 MHz was used as the reference for the NIM box which created the NMR pulse at this frequency. The width of this pulse was controlled with a knob on the NIM box, tunable between 2-15 μs .

The NMR coil in the ^3He probe was connected to a channel on the multiplexer, and the incoming signal was sent to the NIM box, which mixed it down with the reference frequency and digitized it. The NIM box was connected to an oscilloscope (Tetronix MDO3024) which read the digitized signal using the TTL pulse function generator for triggering. We were able to detect the very first NMR signals with ^3He at high field with this setup (Figure 5.8). However, there were two issues that had to be resolved before a signal was detected. The first was that the pulse widths achievable with the UW electronics corresponded to a maximum of 3.7° pulse angle (measurement described below), and the second was that the noise was larger than the signal size. We addressed both of these issues by averaging over many pulses on the oscilloscope, so that the NMR pulse angles added up to a larger angle, and the random noise averaged to 0. Additionally, in order to prevent dephasing of the nuclei precession from one pulse to the next, the LO frequency used was only a few hundred Hz away from the ^3He NMR frequency (LO = 47.0141 MHz). This led to the first successful detection of the NMR signal at 1.45 T.

Once the signal was detected, we improved the setup by using a LabVIEW program in conjunction with a National Instruments X-series 6363 Data Acquisition (DAQ) box. This eliminated the use of the TTL pulse function generator, as the LabVIEW program could create TTL pulses with more control over timing - the program can send a predetermined

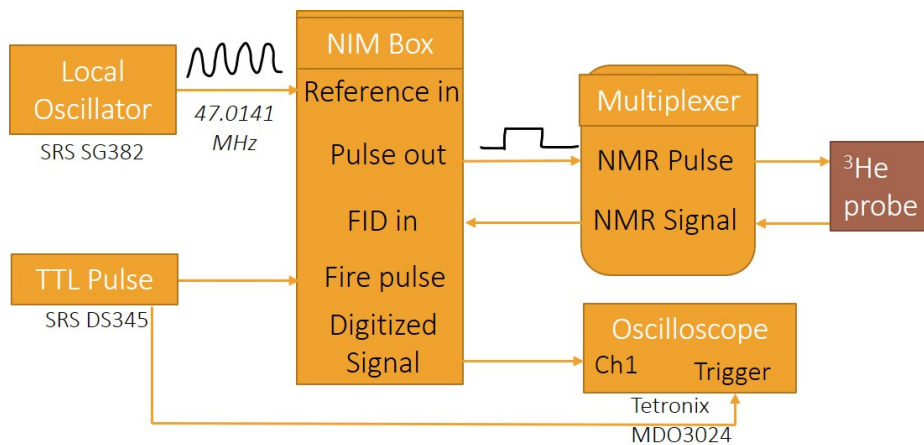


Figure 5.8: UW NMR electronics diagram.

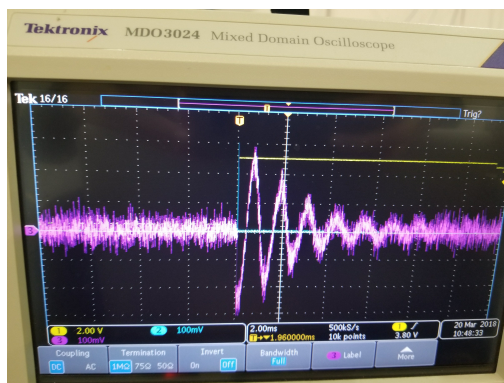


Figure 5.9: Averaged FID signal on oscilloscope measured with UW electronics.

number of pulses t seconds apart. All data shown in this section was recorded with an oscilloscope as shown in Figure 5.9 and transferred to a computer using a flash drive. See Appendix A for a discussion of the fit model used to extract the frequency, amplitude, and T_2^* of the FIDs.

5.2.2 NMR Data and Studies

All data collected with the UW electronics utilized the following settings:

- reference frequency: 47.0141 MHz
- pulse width: $15 \mu\text{s}$
- number of pulses: 16
- time between pulses: 0.96 sec
- saddle coil tuned to 47.01 ± 0.01 MHz, $50 \pm 0.4 \Omega$ impedance

MEOP settings:

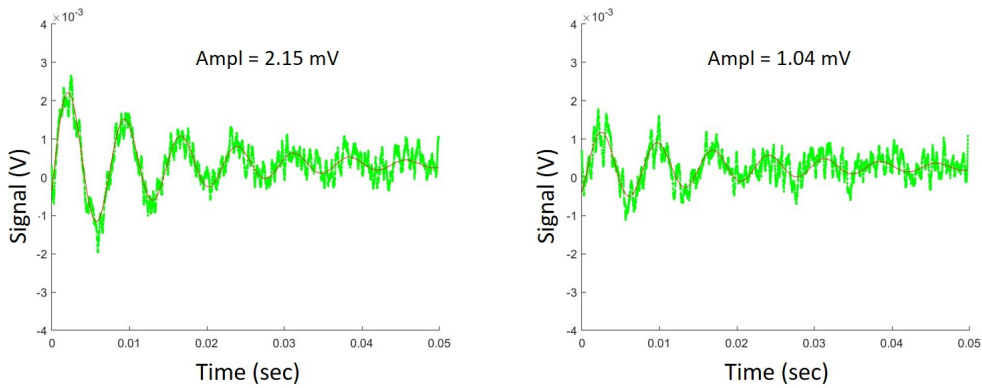
- discharge at 6 MHz,
- laser absorption line: f_2^- or f_4^- for various studies
- laser power: 2 W

- gas polarized for 2-5 min

The goal of the first few studies was to find optimal parameters to maximize the signal size and stability. These included using different absorption lines for MEOP, changing sample cells to study gas pressure dependence, measuring the T_1 relaxation time (explained in Section 3.3) with different pressure cells, varying the polarization time, and varying the amplitude of the NMR pulse.

A study reported in reference [40] showed that different absorption lines of the ^3He gas spectrum can yield higher or lower polarizations via MEOP. We measured the NMR signal for both absorption lines and found that the f_4^- line produced a signal amplitude higher by a factor of two than f_2^- as shown in Figure 5.10, indicating higher polarization of the gas. This study was conducted with the 2 Torr cell and the results were consistent with [40].

We then studied the pressure dependence of the signal by changing the cell used in the magnetometer. Cells with gas pressures of 2, 10, and 40 Torr were used (see Figure 5.11), where these labels are based on the nominal pressure when filling the cells at room temperature and correspond to approximately 3.5×10^{22} $^3\text{He}/\text{m}^3$ with uncertainty of ~ 1 Torr. We found that while the signal size increased with increasing pressure by a factor of 4, the transverse relaxation time T_2^* decreased by a factor of ~ 5 for the 2 and 10 Torr cells, respectively. The 10 and 40 Torr cells did not display this varying behavior. The change



(a) FID Signal after polarization at f_4^- . (b) FID Signal after polarization at f_2^- .

Figure 5.10: FID amplitude study for different laser absorption lines.

in the signal size between the 2 and 10 Torr cells was expected since the higher density of nuclei in the higher pressure cells produce a larger precession signal. However, we did not see this between 10 and 40 T cells. Since the signal size is proportional to both density and polarization in the gas, the study indicated that the achieved polarization in the 40 T cell may have been lower due to the weaker hyperfine coupling, producing a signal amplitude similar to the 10 Torr cell despite the higher density.

Additionally, the shorter T_2^* at higher pressure was also expected. In the motional narrowing regime, T_2^* has an inversely proportional relationship with the diffusion constant D of the gas, which is inversely proportional to the sample number density. As explained in section 3.3, dephasing can occur because of gradients, but the effect is reduced by diffusion since the atoms with different initial positions average nearly the same field distributions. As the pressure increases, this averaging is less effective [44], [45], leading to a decreased T_2^* :

$$\frac{1}{T_2^*} = \frac{4\gamma^2 R^2}{175D} (\vec{\nabla} B_x^2 + \vec{\nabla} B_y^2 + 2\vec{\nabla} B_z^2) = \frac{1}{2T_1} + \frac{8\gamma^2 R^2}{175D} (\vec{\nabla} B_z^2) \quad (5.6)$$

Note that the scale of T_2^* was much shorter (10s of milliseconds) than what was seen at Michigan (300 ms). This indicated that additional gradients were present in the setup since the homogeneity of the Argonne magnet was much better than the Helmholtz coils at Michigan. We were able to make some changes and improve T_2^* months later after the Umich NMR electronics were implemented (see Section 5.3). Specifically we found a magnetic cable in the setup and upon its removal observed T_2^* increase to >3 seconds for the 2 Torr cell.

Next, we conducted studies of the T_1 time, or the time it takes for the longitudinal polarization in the sample to decay once the sample is polarized via MEOP. T_1 also depends on the diffusion constant and field gradients as discussed in section 3.3:

$$\frac{1}{T_1} = \frac{8\gamma^2 R^2}{175D} [\vec{\nabla} B_x^2 + \vec{\nabla} B_y^2] \quad (5.7)$$

Note that T_1 plays a different role in proton NMR with water samples than in ^3He . In water,

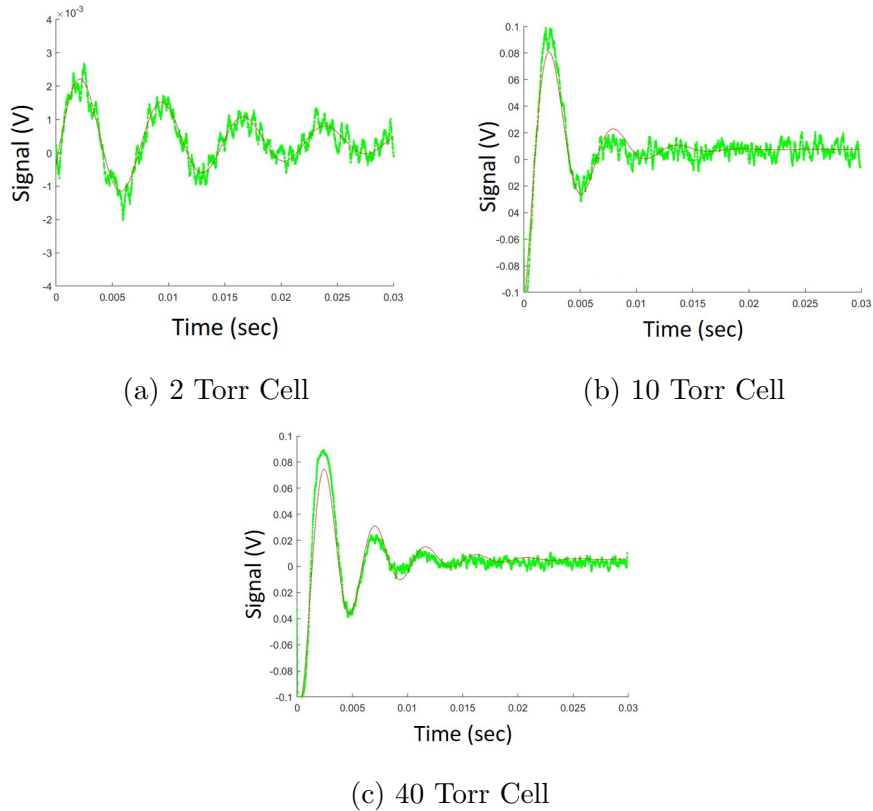


Figure 5.11: Pressure dependence study. Note that the vertical scales are different.

T_1 is a measure of the time it takes for the sample to recover equilibrium polarization P_z after the NMR pulse has rotated it, while in ^3He the polarization decays almost completely (to small nonzero equilibrium value given by Boltzmann distribution) after time T_1 without the presence of a mechanism to repolarize the sample (such as MEOP). With the UW electronics, we were able to place some limits on the length of T_1 for different gas pressures of ^3He : in the 2 Torr cell, $T_1 > 12$ min, and in the 10 and 40 Torr cells, $T_1 > 30$ min. The last two studies combined suggested that the 10 Torr cell may be the best candidate for the ^3He magnetometer since the polarization signal lasted a long time while the short T_2^* did not limit data collection.

Another study for signal optimization was to check how long MEOP needed to be performed so the gas polarization was sufficient to produce an NMR signal with a high SNR. We found that about 4 to 5 minutes of polarization time was necessary for the 2 Torr cell,

while only 2 minutes were required for the higher pressure cells. This was in agreement with the prediction as the higher pressures yield a higher collision rate for MEOP and hence the gas is polarized faster.

Next, we attempted to vary the pulse width and power but were limited by the UW electronics. The pulse width had an upper limit of 15 μs and increasing the amplitude of the pulse did not increase the amplitude B_1 field produced by the NMR coil. The B_1 field amplitude was measured by picking up the field as induced voltage on a 5-turn, 2-cm test coil placed within the NMR saddle coil. Using Faraday's law of induction for the voltage of the second coil V_{pk-pk} , we estimated the field B_{coil-1} produced by the first coil (NMR saddle coil):

$$\varepsilon_{pk} = \frac{V_{pk-pk}}{2} = \frac{N\pi r^2 B_{coil-1} (2\pi f)}{2} \quad (5.8)$$

where N and r are the number of turns and radius of the second coil and $f = 47\text{MHz}$ is the driving frequency. $B_{NMR-coil}$ was found to be $\sim 10 \mu\text{T}$. Using the equation for pulse time from section 3.3 ($t = \theta/(\gamma B_1)$), we found that a 15 μs long pulse corresponded to a maximum angle θ of 3.7° rotation of the ^3He magnetization. This study indicated that longer pulses with more power were needed.

Additionally, we used two test coils to estimate the field produced by the gas magnetization. We first drove one circular coil (3 turns) with a function generator at 47.02 MHz and 0.1 V peak-to-peak voltage. This was picked up as 40 mV pk-pk by a second test coil, circular with 2-cm radius and 5 turns. Plugging these into equation 5.8 yielded a field of ~ 0.1 mG produced by the test coil. Next, we conducted the same test using the saddle coil as the secondary coil and found the voltage picked up and amplified by the UW electronics: $V_{pk-pk} = 2$ V. Hence, a 2 V pk-pk signal picked up by the saddle coil and the UW electronics was consistent with a 0.1 mG field. Applying this ratio to the ^3He FID amplitude, ~ 8 mV, we estimated that the field produced by the precessing nuclei of the gas was $0.4 \mu\text{G}$.

Besides the signal size, T_1 , T_2^* , and pulse width, power studies and produced field studies, we performed two other tests with the UW electronics. We checked that the extracted

frequency changed accordingly when the reference frequency was increased or decreased to confirm signal validity, just as was done for low field NMR at Michigan. We changed the reference frequency by a few Hz (10s of ppb), and saw the reference frequency shift as expected. Lastly, we performed some stability studies in which a few different measurements were taken without moving the setup. We found that the frequency shifted by about 3 Hz for different measurements, which was within the ~ 3 Hz uncertainty from the FID fits. These measurements were hence consistent to 64 ppb.

5.3 NMR Studies with Umich Electronics

Due to the limitations of the UW NMR system for the ^3He probe, we designed a more versatile system that could be optimized for these studies. The important features were:

- High power, coupling to the 10 W pulse amplifier (TOMCO RF Amplifier),
- Optimized component selection to handle pulse power, width, and gating (timing),
- Longer pulse capability,
- Modular components,
- High precision timing, sync to Rb clock, and
- Noise reduction.

5.3.1 Umich NMR Pulse Controller

The electronics diagram is shown in Figure 5.12, including the Umich NMR Pulse Controller electronics in the dashed box. These consisted of two mini-circuits switches, a bandpass filter at 48 MHz to select the nominal ^3He frequency, an amplifier, a mixer, and a circuit board for converting TTL pulses to -8V to control the switches. The pulse controller box was connected to a power supply, a function generator to provide the local oscillator reference frequency

(SRS SG382), a high power RF amplifier (Tomco BT00250-Gamma) to produce powerful NMR pulses, a preamplifier (SRS SR560) to eliminate noise, and the saddle coil which behaved as the NMR pulse producer and signal receiver. Additionally, the pulse controller electronics were connected to a data acquisition system (NI X-Series 6363) controlled with LabVIEW, which determined the timing of the switches, controlled the length and number of NMR pulses, and digitized the FID signal.

The NMR pulse was generated through the following path: the local oscillator (LO) sent an RF wave at 47.014 MHz and 120 mV peak-to-peak amplitude to the TOMCO for amplification. The TOMCO was connected to the Umich pulse controller which sent this NMR pulse to the ^3He probe. The TOMCO amplifier output could be turned on and off to produce a pulse of variable length. We studied the output to our coil and determined that the pulse width could be controlled with a resolution of $0.5 \mu\text{s}$, with a minimum pulse width of $2 \mu\text{s}$. The timing of the pulse shown in Figure 5.13 was determined by three outputs from the X-series box controlled by LabVIEW:

- the preamp gate (mini-circuits ZSFWHA-1-20+) was switched off for $100 \mu\text{s}$,
- after a $2 \mu\text{s}$ delay, the probe switch (ZFSWA-2-46) connected the probe to the TOMCO for $64 \mu\text{s}$ (This SPDT switch normally connected the probe to the signal channel; for the pulse, the probe was switched to the RF pulse channel for $64 \mu\text{s}$),
- after a $24 \mu\text{s}$ delay, the Tomco was turned on for $40 \mu\text{s}$.

This last duration of the Tomco control determined the length of the NMR pulse created, nominally $40 \mu\text{s}$ for ^3He . After the pulse, the SPDT switch connected the probe (NMR coil) to the signal channel consisting of a bandpass filter (mini-circuits BPF-B48+), an amplifier (mini-circuits ZFL-500LNB+), and a mixer (mini-circuits ZX05-1L-S+) which mixed the signal frequency with the reference (LO) frequency. Typical IF frequencies - the difference of the LO and ^3He precession frequencies - were between 200-600 Hz. The mixed down signal was then filtered with a preamplifier (SRS SR560), which included a 12 dB low pass filter

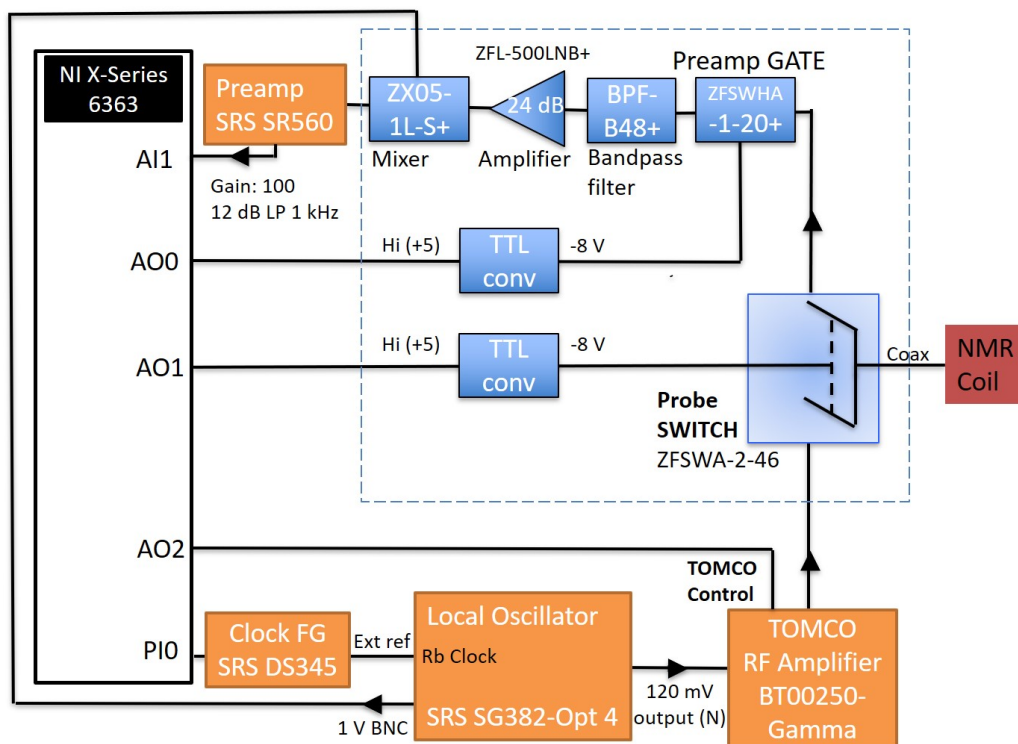


Figure 5.12: Electronics diagram for high field NMR including Umich Pulse Controller (dashed box).

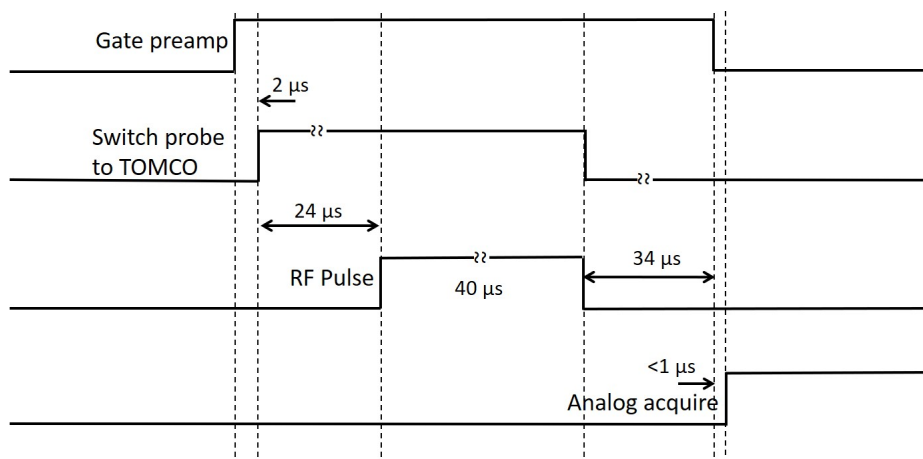


Figure 5.13: Umich NMR Pulse Controller timing diagram.

at 1 kHz to reduce noise. The preamp gain was set to 100 for further amplification of the signal, at which point the signal was input into an analog channel on the NI DAQ box and recorded with the LabVIEW program.

For each set of data, the number of pulses sent as well as the time between the pulses were controlled with the LabVIEW program which used an external clock for timing. The data rate (2-10 kHz) was determined by an external function generator (SRS DS345) which was connected to the NI DAQ clock input, and synced to the Rb clock (SRS SG382-Option 4). The LO function generator was also synced to this clock so the timing of all components used the same Rb-based reference (Stability < 0.1 ppb, Aging <1 ppb/year). The data rate for ^3He was set to 2 kHz and we collected 4000 samples over a period of 2 seconds for each pulse. Most datasets consisted of 5 total pulses so that the extracted frequency was averaged from 5 FID shots.

In addition to producing longer NMR pulses, the Umich pulse controller also generated higher power pulses than the UW electronics. To make this comparison we picked up the pulse field produced by the NMR saddle coil as an induction voltage on a circular coil (2 cm radius, 5 turns). When the pulse coil was driven with the UW electronics at 47.014 MHz and an input peak to peak voltage of 20 mV, the voltage picked up by circular coil was 4 V pk-pk. As described in the previous section, this voltage value saturated at 8 V pk-pk as the input voltage was increased so more powerful pulses could not be produced with the UW system.

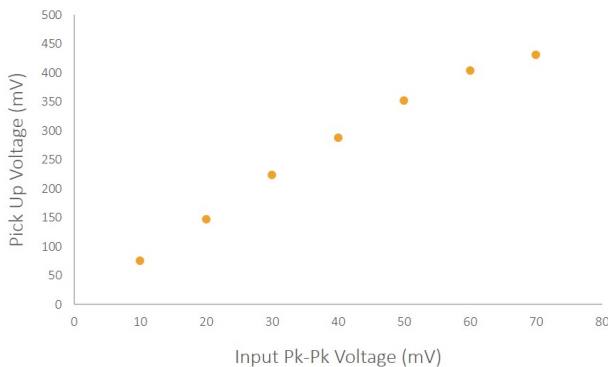
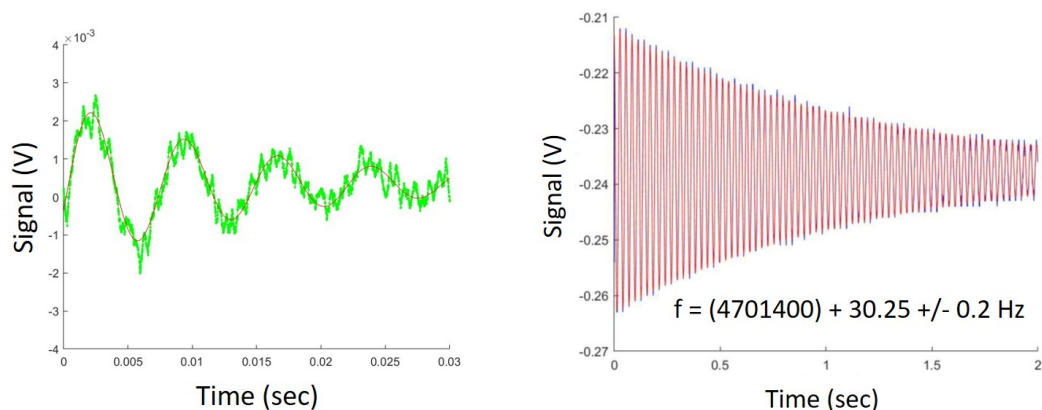


Figure 5.14: Induced voltage on a pick up coil due to field created by the saddle coil and Umich NMR pulse controller as a function of input voltage.

Driving the same saddle coil with the Umich NMR electronics (including amplification of the pulse with the TOMCO), the picked up voltage increased linearly with the input voltage as shown in Figure 5.14. While the produced pulse power also saturated with increasing voltage, we were able to produce pulses yielding a 20 V pk-pk pick up amplitude. This more powerful and longer duration pulse capability allowed for pulse angles in the entire range of 2-90°, as compared to the UW electronics which produced a maximum 3.7° angle.

The longer and more powerful pulses and noise removal with the Umich NMR system (Figure 5.12) were big improvements over the UW electronics and produced one shot FIDs eliminating the need to average over many (~ 16) pulses. Another improvement made in the apparatus at the same time as the Umich system installation was the switch from the aluminum box to copper as described in section 5.1.4. This shield accomplished both: reduced leakage of RF radiation from the discharge coils as well as the NMR saddle coil as required by Argonne safety, and also provided shielding from electrical noise for the NMR electronics. The last change made after implementation of the Umich NMR system was the replacement of a mini-coax style cable connecting the NMR coil circuit (Figure 5.7) to the pulse controller. We found this cable to be slightly magnetic and upon replacing it with



(a) FID and fit with UW electronics averaged over 16 pulses.

(b) FID and fit with Umich electronics averaged over 5 pulses.

Figure 5.15: High Field FID with (a) UW and (b) Umich electronics. Note that the data in (b) were taken after the switch to a copper shield and replacement of the magnetic cable.

another mini-coax SMA cable constructed without the use of nickel [54], the T_2^* of the signal increased from the 3-20 ms range with the UW electronics to >1 second with the Umich system as shown in Figure 5.15.

5.3.2 NMR Studies

We conducted several studies with the Umich NMR pulse controller and electronics. The first was to check the stability of the clock. For this we used a function generator (SRS SG382) as the probe input to the pulse controller, and set at a frequency 100 Hz away from the reference. Both function generators, the reference LO and the input probe, were synced with the Rb clock function generator which also controlled the DAQ timing. A total of 200 measurements were taken over a period of 1000 minutes (1 measurement every 5 minutes) and a spread of ~ 0.009 Hz was seen as shown in Figure 5.16.

Next, we checked the stability of the ^3He FID signal frequency over both long and short periods of time. Figure 5.17 shows data taken two days apart with extracted frequencies plotted as a function of the NMR pulse number. The spread is about 0.2 Hz over 20 min and up to 0.5 Hz over the two day period, indicating that the frequency drifted by 11 ppb. The next day we performed a few short time-scale studies each with 15 measurements taken over a period of 22 minutes, consisting of 3 sets of 5 pulses, with the pulses fired 1 min apart

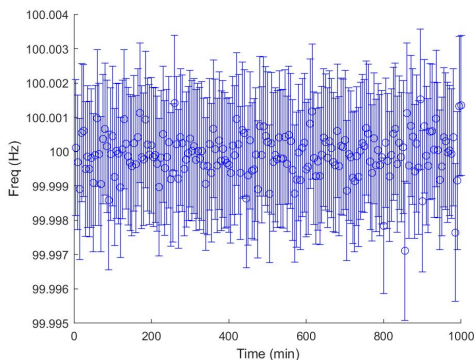


Figure 5.16: Set of 200 frequency measurements to check clock stability. The error bars are determined from the standard deviation of the measurements.

and the 3 sets separated by 5 min each. These data sets are shown in Figure 5.18, from which it is clear that the spread in each set of 5 pulses is much smaller (sub-ppb level) than the spread over the longer 22 min period. This indicated that the frequency drift was not due to the NMR electronics or the ^3He probe, but rather due to the magnetic field drift. A similar magnet drift had previously been measured by the Argonne group.

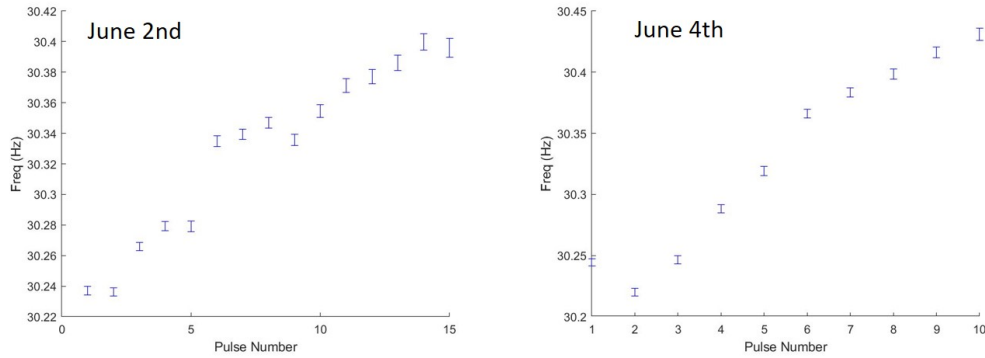


Figure 5.17: Frequency stability data for two different days. The error bars are determined from 68% confidence interval of the extracted frequencies from the Matlab fit.

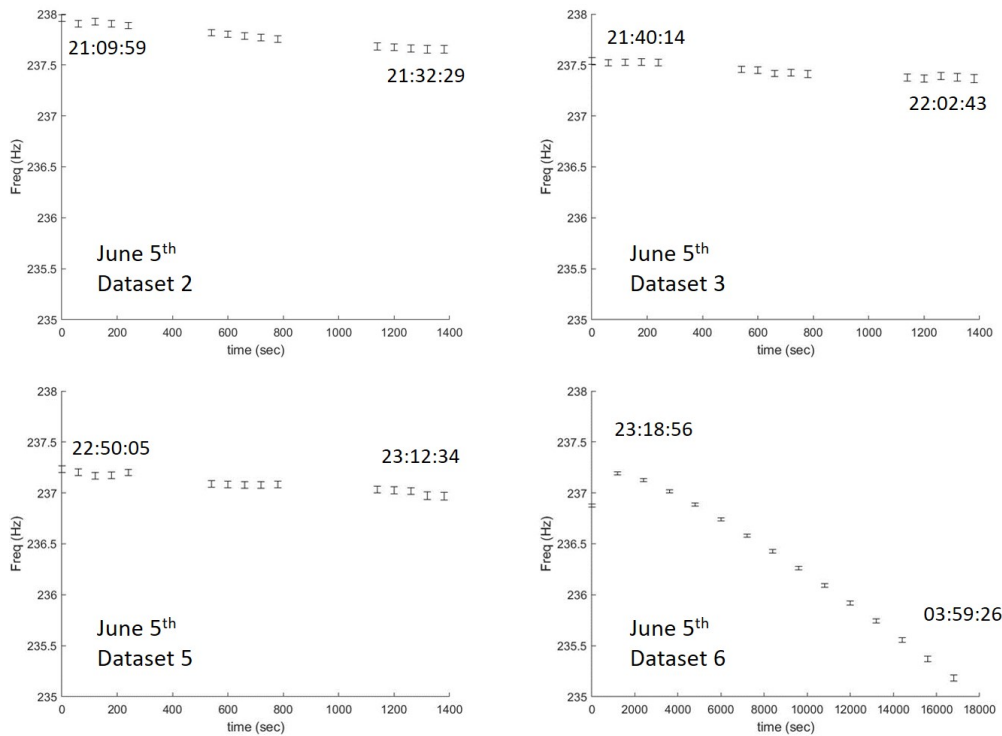


Figure 5.18: Frequency stability data for short and long timescales. The error bars are determined from 68% confidence interval of the extracted frequencies from the Matlab fit.

At the end of the day, we conducted another long timescale study by taking data overnight for a 5-hr period as shown in Figure 5.18. These four sets of data demonstrate that the magnet drifted by about 15 ppb/hr over long timescales, while the frequency extraction with the Umich NMR system was stable to 0.2 Hz (4 ppb) for short time-scales (5 minutes or less). Note that the extracted frequencies in Figures 5.17 and 5.18 are 200 Hz apart because the local oscillator frequency was changed between measurements.

We repeated the T_2^* relaxation time studies with the Umich system which had previously been conducted with the UW electronics. Figure 5.19 shows FIDs from the 2 and 10 Torr cells, where the lower pressure cell had a much longer T_2^* (~ 3 sec vs. ~ 1.25 sec) as expected. The amplitude of the 10 Torr cell was about 5 times that of the 2 Torr cell FID (~ 50 mV vs. ~ 10 mV peak-to-peak) consistent with studies with the UW system and expectation. If we assume that both cells had similar polarization levels, the higher amplitude would be expected due to the 5 times higher density (pressure) of the 10 Torr cell. While we did not actively measure the polarization before performing NMR and the 2 Torr cell was polarized for a longer period of time (5 min) than the 10 Torr cell (2.5 min) in order to attain the FIDs, the results of this study suggest that similar polarization levels were achieved in each cell despite the different times of polarization.

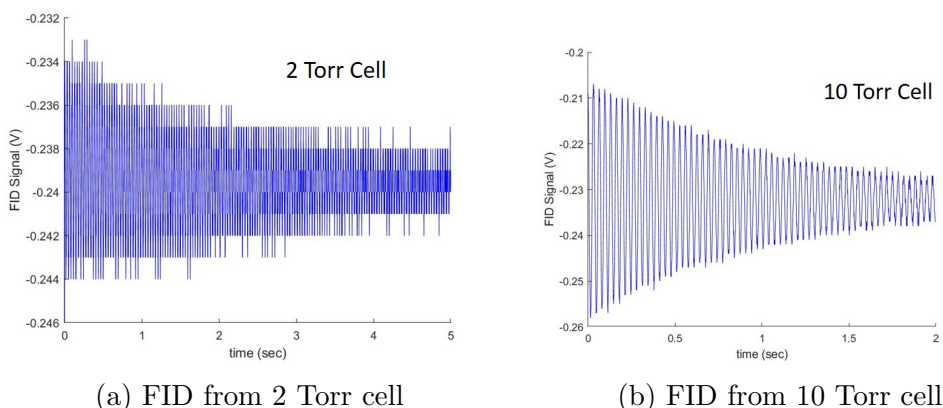
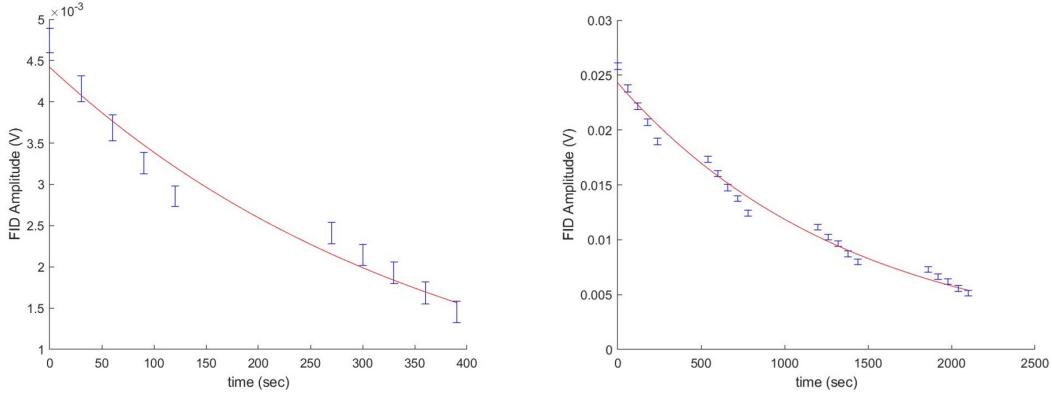


Figure 5.19: Pressure dependent study of FID signal with Umich pulse controller. Note that these studies were performed with the same electronic gain settings and the two plots have different x- and y-scales. The digital noise in (a) is due to the ~ 1 mV resolution of the data acquisition system.



(a) Signal amplitude vs. time for 2 T cell (b) Signal amplitude vs. time 10 T cell

Figure 5.20: Amplitude decay study for 2 and 10 Torr cells. The error bars are determined from 68% confidence interval of the amplitude value from the Matlab fit. Note that the decay does not follow the model due to additional time waited between each set of 5 measurements, i.e. the T_1 decay is on a longer time scale than decay due to each pulse.

Another study of interest was determining how many datasets were possible after hyperpolarization of the gas with MEOP was performed for each cell. We conducted multiple sets of NMR measurements until the polarization diminished, which was due to a combination of the amount of initial polarization in each cell and T_1 longitudinal relaxation time. We found through this test that the 2 Torr cell signal amplitude, and hence the polarization, disappeared after 2 sets of 5 pulses were sent over a period of 6.5 minutes, while the 10 Torr cell signal lasted for 24 min for 4 sets of 5 pulses, as shown in Figure 5.20. This indicated that the 10 Torr cell would be more useful for further studies and the cross-calibration of the BNL probe since it could be polarized in half the time than the 2 Torr cell and 4 times more data could be taken without needing to polarize again.

The data from Figure 5.20b were analyzed to determine the size of the NMR pulse angle. Since the initial magnetization M_0 reduces by $\cos(\theta)$ after each pulse, the magnetization after the first pulse is given by:

$$M_z = M_0 \cos(\theta) \quad (5.9)$$

Using this iteratively, we find that the magnetization after the k th pulse should be:

$$M_z(k) = M_0[\cos(\theta)]^k \quad (5.10)$$

As the magnetization is directly proportional to signal amplitude, we fit the amplitudes from each set of 5 pulses to the function ab^k , where k is the pulse number, and b is the fit parameter equivalent to $\cos(\theta)$. We found that a 40 μ s pulse length amplified with the Tomco was equivalent to a pulse with a 23° angle.

For completeness, we conducted a more detailed study of the 10 Torr cell longitudinal relaxation time T_1 . In order to measure the true T_1 , we reduced the pulse angle to $\sim 8^\circ$ and also separated the pulses over time. A total of 15 pulses were fired over a 5 hour period and the amplitudes, corrected for the pulse angle by dividing each n th amplitude value by $\cos(\theta)^n$, were fit to an exponential decay as a function of time ($\alpha e^{-t/T_1}$). The data and fit shown in Figure 5.21 yielded a T_1 of 135 minutes.

Lastly, we studied the effect of rotating the cell stem with respect to the direction of the field axis. We found that the signal frequency shifted and there was also an impact on T_2^* . Since this measurement required removing the setup from the magnet, rotating the cell by

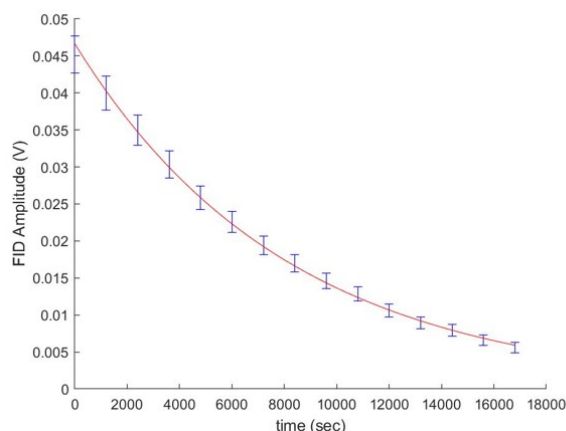


Figure 5.21: Amplitude decay of FID signal, corrected for NMR pulse angle 8° , as a function of time. Extracted $T_1 = 134$ min. The error bars are determined from 68% confidence interval of the amplitude value from the Matlab fit.

hand, and inserting the probe back into the magnet, a precise frequency shift could not be measured as the movement of the probe also caused frequency shifts. However, we repeated this study after implementing a method to place the probe repeatably back in the same position in the magnet. The details of this study are given in the next chapter.

5.4 Umich Electronics for Proton NMR

In order to cross-calibrate the BNL probe with the ^3He probe, we also built an NMR pulse controller for protons. The electronics were identical to the ^3He electronics described in the previous section, except for the bandpass filter used was appropriate for 61 MHz for proton NMR. The same local oscillator was used at a different frequency, 61.7154 MHz, and the pulse reference signal was amplified with the same Tomco amplifier by switching cables by hand.

The NMR coil used was built in to the BNL water probe - 1 cm long with 5.5 turn coil and 15 mm diameter as described in [55]. The detected signal was amplified using a separate preamplifier (same model) than the ^3He probe. The pulse timing and lengths were also different. While the same timing diagram as ^3He was used to control the electronic switches, the NMR pulse length was much shorter: 15 μs . A second SRS DS345 function generator also referenced the Rb clock to set the 10 kHz data rate. A total of 5000 samples were read for each pulse with an acquisition time of 0.5 sec. For each data set, we averaged over 5 pulses with 6 s of wait time between pulses so the rotated polarization could be recovered in between pulses. (Recall that T_1 for protons is the time it takes the magnetization of the sample to return to its equilibrium value after the first NMR pulse has rotated it. We measured this T_1 time to be 6 seconds and waited for equilibrium before firing each consecutive pulse.)

Chapter 6

Absolute Measurement and Cross-calibration

6.1 Methods

Each BNL probe, cylindrical and spherical, was cross-calibrated with the ^3He probe in the Argonne magnet field of 1.45 T. We designed a 3D printed mount, as described in section 6.1.1 below, to hold both probes for calibration purposes. Section 6.1.2 details the use of magnetic field gradients to position the two probes in the same location in the magnet and to minimize the inhomogeneity of the field. The cross-calibration campaign is described in section 6.1.3 and then the corrections for each probe are detailed. Lastly we give the final numbers with uncertainties for the absolute calibration cross-check for each probe.

6.1.1 Mounting Both Probes

In order to perform the cross-calibration efficiently, we designed a holder, 3D printed with Acrylonitrile Butadiene Styrene (ABS) plastic, in which both probes, BNL and ^3He , could be mounted simultaneously. This not only decreased the time between measurements with each probe minimizing field drift effects, but also eliminated errors that would be caused by

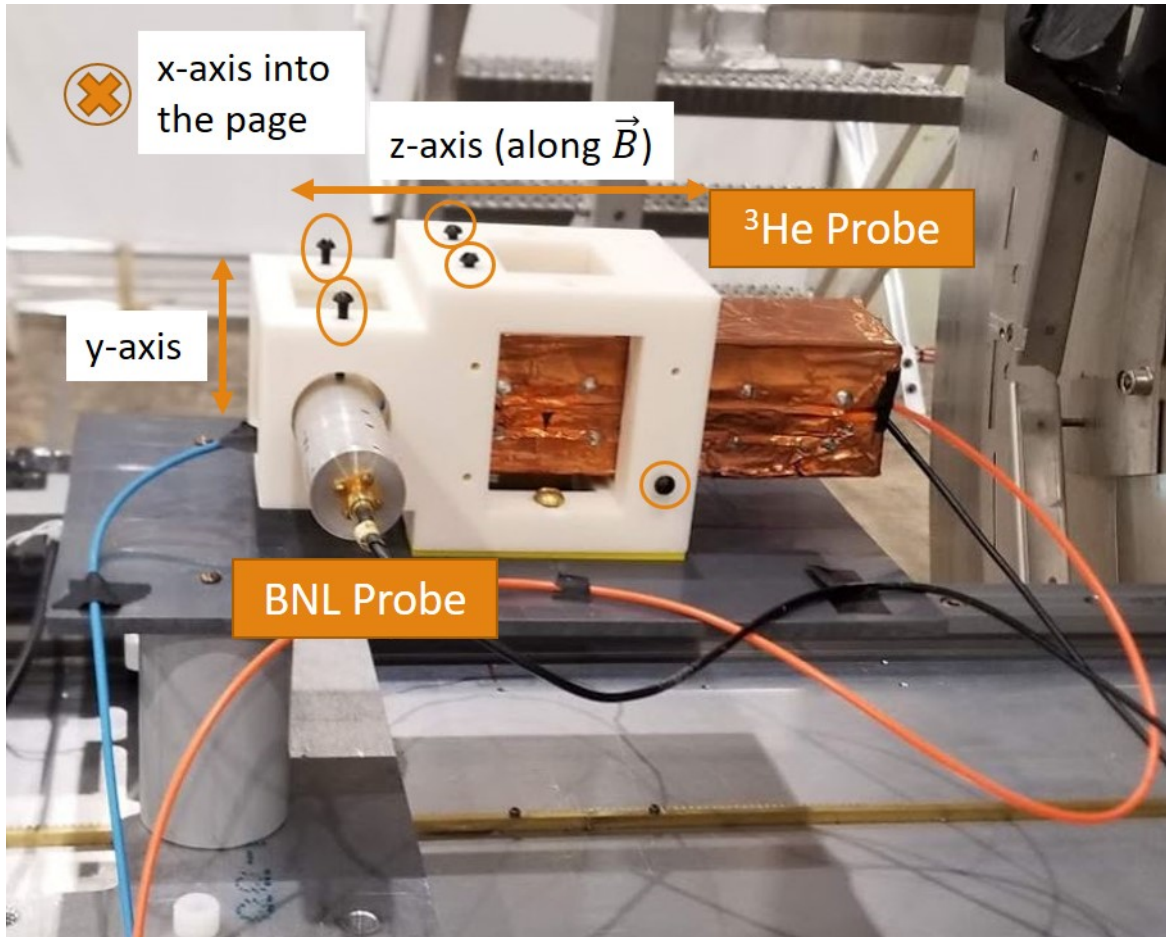


Figure 6.1: The 3D printed holder (ivory) is mounted onto the 1D stage. Both the ^3He and BNL probes are fixed inside the holder with screws (circled). The x, y, and z directions are also indicated, with the magnetic field along the z-axis.

un-mounting and remounting of the probes, such as changes in position or material effects. The holder sat on a PVC plastic diving board-shaped plate mounted on two PVC cylinders screwed on a 1D aluminum stage. The stage could travel into and out of the Argonne magnet along the magnetic field axis (z-axis) controlled by a motor. The holder was designed with slots into which each probe could be inserted, with some room for adjustment in the x and y directions. Here, y axis is along the vertical and x axis is horizontal and orthogonal to the magnetic field axis (z-axis). Figure 6.1 shows the holder mounted on the stage with both probes inserted and indicates the x, y, and z axes orientations.

The BNL probe slid into the mount with its axis along the x-direction, and both the x

and y positions of the probe could be adjusted with 4 nylotron screws, 2 on top (circled in the figure) and 2 on bottom. There was ~ 6 cm of adjustment room in the x-direction, and about ~ 2 cm room in y. The ^3He probe sat in the holder with its axis, the optical pumping beam axis, in the z-direction along the magnetic field. There was about 1 cm allowance for positioning the probe in the x-direction using nylotron screws mounted on either side of the holder. The y-position of the ^3He probe could be adjusted by about 2 cm, in increments of 0.2 cm using 3D printed (PLA plastic) shims which sit either between the probe and holder or between the holder and the diving board.

Once the center of the active volumes of the two probes, i.e. the areas of the samples accessible by the NMR coil, were aligned in x and y by using the adjustment screws and shims, the only free movement allowed was in the z-axis, controlled with the 1D stage. The stage could be translated along z to place the "center of magnetic sensitivity" of the two probes at the same position in x, y, and z, and therefore, in the absence of drifts, at the same magnetic field and gradient. This placement of each probe was determined using the $\Delta B = 0$ method.

6.1.2 Delta B Method

The cross-calibration effort required that both probes measured the same field in the same location of the magnet. This was challenging because the probe frequencies could not be compared to each other to verify that they measure the same field for two reasons: 1. Each probe measures an NMR frequency shifted from the actual value due to shielding effects from the materials surrounding the water or ^3He sample, and 2. Each measured frequency is multiplied by a different proportionality factor to calculate the magnetic field since the gyromagnetic ratios for water and ^3He are different. Additionally, measuring the field at the same location with each probe required attention as spatial gradients in the magnet had been previously measured to be ~ 5 ppb/mm by the Argonne group. Since the goal of this work was to cross-calibrate with less than 30 ppb uncertainty, the probes needed to be positioned

repeatably at the same location to sub-mm precision with minimal gradients present using a method independent of shifts caused by material effects and the different gyromagnetic ratios. This goal was achieved with the $\Delta B = 0$ method.

The method utilized the active shim coils of the magnet, which are capable of producing a known spatial linear gradient along each axis. The produced gradient could be controlled remotely with a computer program by changing the current in the shim coils, which were shown to be stable for \sim few hours and produced gradients repeatable to ~ 0.02 A, as measured by the Argonne group. The $\Delta B = 0$ method was performed using the gradients through the following steps (for simplicity we only outline the procedure for the z-axis, but it is applicable to x and y axes as well):

- Apply a linear gradient using a current value ($I_1 = 0.25$ Amps) in shim coil for the z-direction
- scan the z-axis of the magnet with a probe (^3He or BNL) taking multiple field measurements at different z-locations while keeping the x- and y- positions unchanged
- Apply the opposite gradient (or any different gradient) with shim coil current ($I_2 = -0.25$ Amps) along the z-axis
- Conduct the same scan in z-axis using the same probe
- Plot each frequency scan as a function of position, fit each to a line, and find the unique point where the two lines cross

This point at which

$$\Delta B = B(I_1) - B(I_2) = 0 \tag{6.1}$$

as measured by a probe is a unique location in the magnet. By finding this $\Delta B = 0$ point with each probe in the z-direction, we were able to place the probes in the same location in z. For the z-scan, the probes were mounted on a motorized stage, and the position of the stage was controlled by a rotary motor. The position of the motor/stage was recorded in

bits as it was moved from point to point. A sample scan with the ^3He probe conducted for three currents in the z-direction, 0.25 A, -0.25 A, and 0 A, is shown in Figure 6.2. The point of intersection given by $\Delta B = 0$ indicates that the active volume of the probe is positioned uniquely in the magnet.

This process could be repeated for x- and y- axes. Since the stage used for the cross-calibration only moved in the z direction, the x and y movements had to be conducted by hand. For example, for the ^3He probe, we measured a ΔB value with two y-axis gradients at one position, and if the value was non-zero, we moved the probe up or down. We repeated this procedure until $\Delta B = 0$ was measured with an uncertainty of less than ± 0.5 Hz. This program was repeated for the x-axis for ^3He and then for both x and y for the BNL probe.

The advantage of using this method is that if the probe materials produce a gradient that is proportional to the field at the ppm level, both $B(I_1)$ and $B(I_2)$ also get shifted by this gradient, but taking the difference of the two frequencies for the two current values cancels out this shift. If we had not used this method, we would have to address this complication even though it is small because the material susceptibilities are on the ppm level. Lastly, the reason $\Delta B = 0$ is so powerful is that it gives the additional benefit that we need not worry about the different gyromagnetic ratios of the two samples used, water and ^3He , because when the frequency difference is 0, the magnetic field difference is also 0 independent of the gyromagnetic ratio:

$$\begin{aligned}\omega &= \gamma B \rightarrow \Delta\omega = \gamma\Delta B \\ \Delta\omega &= 0 \rightarrow \Delta B = 0\end{aligned}\tag{6.2}$$

After employing the $\Delta B = 0$ method to position each probe uniquely in the magnet, aligning the active volumes of both ^3He and BNL, we checked that each probe came back to the same position when the stage was moved into and out of the magnet. The position repeatability of the stage was good to sub-mm resolution, as indicated by several back and forth scans along the z-direction with the ^3He probe (Figures 6.3a and 6.3b), which gives

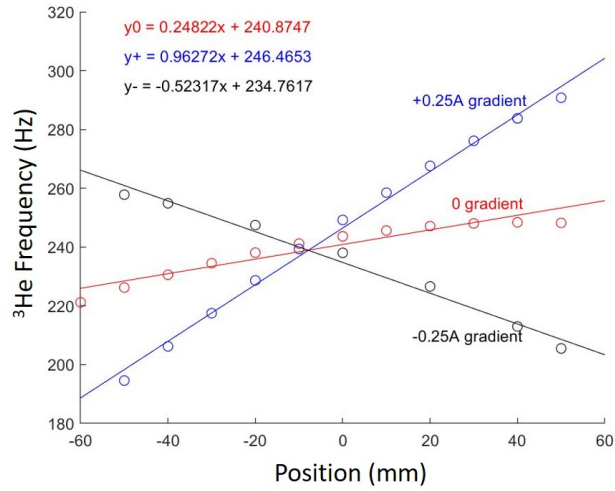
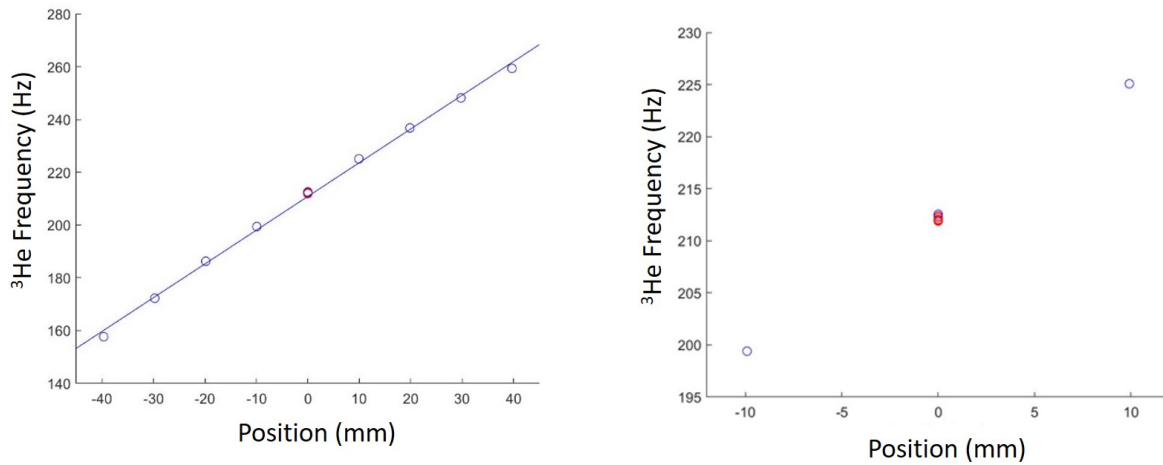


Figure 6.2: Scans of ^3He probe along z-axis with the z-gradient set to three current values. The point of intersection is where $\Delta B = 0$, indicating that the probe active volume is uniquely positioned in the magnet.

an uncertainty of less than 5 ppb on the frequency measurements. The method was used to check both probe positions throughout the cross-calibration effort.



(a) Frequency vs. position in z-axis measured with ^3He

(b) Zoomed in frequency vs. position

Figure 6.3: Position repeatability along z-axis

6.1.3 Cross-calibration Campaign

Before conducting the cross-calibration, we improved the homogeneity of the field around the $\Delta B = 0$ point using the shim coil gradients in all three directions. We also imposed a blinding scheme to offset the ^3He probe frequency from the true measured value throughout the calibration effort to remove bias. We then measured the frequency with each probe using what we call the A-B-A scheme.

As seen in Fig. 6.2, setting the z gradient to 0 Amps, does not produce a horizontal line, indicating that the field changes along the axis. This gradient (~ 0.25 Hz/mm) was previously measured by the Argonne group and was present in the magnet despite the passive shims. We used the active shims to reduce this gradient by applying a negative gradient based on the slope of the line which fits the 0 Amp-current data plotted in blue circles in Figure 6.4. We applied the correcting current to the active coils (-0.08 Amps) and took another scan to check the homogeneity, data plotted as red plus signs. The x- and y- gradients were not measured for this cross-calibration (see section 6.7). We instead used the values: 0 Amps for x-axis and 0.25 Amps for y-axis based on rough gradient measurements performed with a UW NMR probe. These currents were used throughout the cross-calibration to minimize gradients around the probe active volumes.

Before the cross-calibration was performed, we blinded the ^3He extracted frequency in

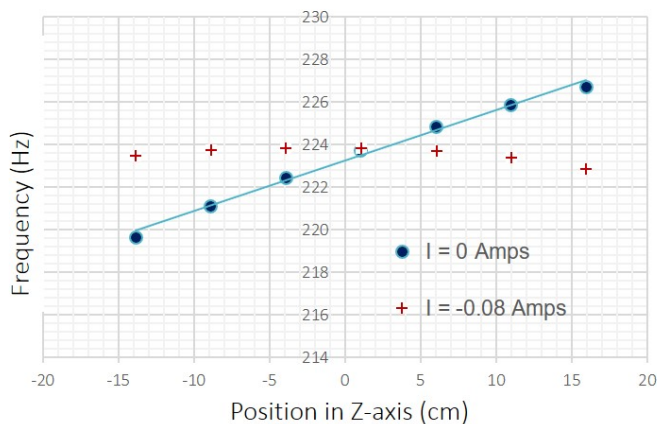


Figure 6.4: Caption

order to ensure that we cross-check the two probes without bias. A random number between ± 15 Hz was generated using Matlab and saved as a binary file hidden from the user. This file was called each time the LabVIEW program was run and the blind was added to the extracted ^3He frequency. Hence the resulting frequency displayed by the program was:

$$f_{disp} = f_{extracted} + f_{blind} \quad (6.3)$$

The BNL probe frequency remained unblinded as the cross-calibration was relative.

The cross-calibration of the ^3He probe with the cylindrical BNL probe was conducted over a 5 hour period using a series of three measurement sets alternating ^3He and BNL probes by translating along the z-axis (magnet axis). We called this measurement scheme A-B-A, which consisted of the following steps:

1. Move ^3He probe to measurement position,
2. Use $\Delta B = 0$ to verify position in x, y, and z,
3. Acquire 5 ^3He FIDs 2 seconds apart and record average frequency (A),
4. Move the stage in z to place BNL probe in measurement position,
5. Confirm position with $\Delta B = 0$ for all three axes,
6. Acquire five BNL FIDs 6 seconds apart (B),
7. Move the stage to position ^3He probe in measurement position,
8. Acquire five ^3He FIDs 2 seconds apart and record average frequency (A), and finally
9. Confirm position with $\Delta B = 0$ for all three axes.

The additional $\Delta B = 0$ measurements were performed to ensure that the probes were coming back to the same location. For ^3He , since the NMR pulse angle was much smaller than $\pi/2$, it was possible to pulse several times without having to repolarize via MEOP. Recall

from Chapters 3 and 5 that we must use a small angle pulse since there is no polarization present in ^3He at equilibrium so a true $\pi/2$ pulse would destroy the polarization in the sample. For water, the pulses were 6 seconds apart ($> T_1$) to allow the polarization to fully recover to equilibrium after the $\pi/2$ pulse rotated it into the transverse plane. All (unblinded) data for both the cylindrical and spherical BNL probe cross-calibration campaigns with ^3He are tabulated in Appendix A, while the final results averaged over all data sets after making corrections are provided in this Chapter.

6.2 Corrections Overview

As explained in Chapter 3, the precession frequency of the sample gas or water is measured with pulsed NMR, which yields the magnetic field:

$$\omega = \gamma_{3,p}B_0, \tag{6.4}$$

where the subscripts 3 and p denote ^3He and protons, respectively. Ideally the NMR measurements for the two samples should be performed in the same magnetic field B_0 . This is not the case in practice due to a number of effects:

- position in the magnet
- drift of the magnetic field
- shielding of the magnetic field due to materials surrounding the sample and the bulk susceptibility/magnetization of the sample
- Resonant effects due to the precessing magnetization and the current induced in the NMR coil (radiation damping)

Additionally the temperature-dependent diamagnetic shielding of the nuclear moments in the ^3He atoms and H_2O molecules must be accounted for. Therefore we must make

corrections to ω for both probes to find the absolute frequencies before they can be cross-checked. Once the positions of the probes are aligned and the magnet drift is accounted for, from Fei [55] the corrections for the water probe would be:

$$\omega_p^{probe} = [1 - \sigma(\text{water}, T) - \delta^{bulk} - \delta^{mat} - \delta^{other}] \omega_p^{free}, \quad (6.5)$$

while the corrections for ^3He probe, different from the water probe, would be:

$$\omega_3^{probe} = [1 - \sigma(^3\text{He}, T) - \delta^{mag-dep} - \delta^{glass} - \delta^{mat} - \delta^{other}] \omega_3^{free} \quad (6.6)$$

In both equations σ is the temperature-dependent diamagnetic shielding factor. Since neither the protons in water nor the Helium-3 nuclei are free but instead surrounded by electrons which shield the nucleus, the magnetic field seen by the protons and ^3He nuclei is shifted. This shift is corrected with σ , which is $\sigma_3 = 59.96743(10) \times 10^{-6}$ for ^3He gas [56] and $\sigma_p = 25.680(\pm 2.5) \times 10^{-6}$ for protons in water at 25°C [57].

The second term in equation 6.5, δ^{bulk} , corrects for the bulk magnetism of the sample. For the BNL probes this effect arises for the cylindrical holder and is 0 for the spherical sample. In the case of ^3He , the magnetization dependent effect, $\delta^{mag-dep}$, includes contributions from the bulk magnetization of the sample and radiation damping of the NMR coil. We separate the total material effects for ^3He into δ^{glass} and δ^{mat} , which correct for the glass cell and all other materials that make up the probe and surround the cell, respectively. δ^{other} are all other corrections. Each of these corrections will be given in detail in the next two sections.

The approach to the cross-calibration is to make these corrections and find ω_{free} using equations 6.5 and 6.6 for each probe, calculate the magnetic field measured by each using equation 6.4 and then compare the two. However, due to the uncertainties on the gyromagnetic ratios discussed in Section 2.2.4 and the fact that the ^3He gyromagnetic ratio is known with respect to protons, we decided on an alternative method for the cross-check. As explained above, σ converts the shielded proton or ^3He nuclei frequency to the unshielded

value. This is the value needed in equation 6.4 when using $\gamma_{3,p}$ for free protons and nuclei. However, Flowers et al. [27] provide the ratio of the shielded water gyromagnetic ratio to the shielded ^3He nuclei gyromagnetic ratio, γ'_p/γ'_3 , to 4.3 ppb as mentioned in Section 2.2.4. We can therefore use this ratio to compare the two frequencies of the shielded protons and nuclei without making the diamagnetic shielding correction (using σ) and cross-calibrate with more precision.

The latter method is employed for the cross-calibration performed for this work, in which we first make all the corrections except σ to find the shielded frequency of each probe, and then use γ'_p/γ'_3 to compare them:

$$\omega_p^{probe} = [1 - \delta^{bulk} - \delta^{mat} - \delta^{other}]\omega'_p \quad (6.7)$$

$$\omega_3^{probe} = [1 - \delta^{mag-dep} - \delta^{glass} - \delta^{mat} - \delta^{other}]\omega'_3 \quad (6.8)$$

$$\omega'_p = \frac{\gamma'_p}{\gamma'_3}\omega'_3 \quad (6.9)$$

where the prime denotes shielded frequencies for protons in water and ^3He gas, respectively.

6.3 BNL Corrections (Cylindrical Probe)

We first correct the BNL probe measured frequencies for the linear field drift of the magnet. This is followed by corrections due to the bulk magnetism of the sample, the probe materials, all other materials surrounding the probe, and a temperature correction.

6.3.1 Drift Correction for BNL Probe

Each cross-calibration data set [A-B-A] consisted of an average of 5 ^3He frequency measurements at time t_1 , followed by an average of 5 BNL measurements at time t_2 , and then another set of 5 frequency measurements with the ^3He probe at time t_3 . The times between t_1 , t_2 , and t_3 were less than 15 minutes for each data set, which allowed for movement of each

probe to the same location in the magnet and verification of this position with the $\Delta B = 0$ method. While the field of the Argonne magnet was quite stable, a small linear drift had previously been measured over time.

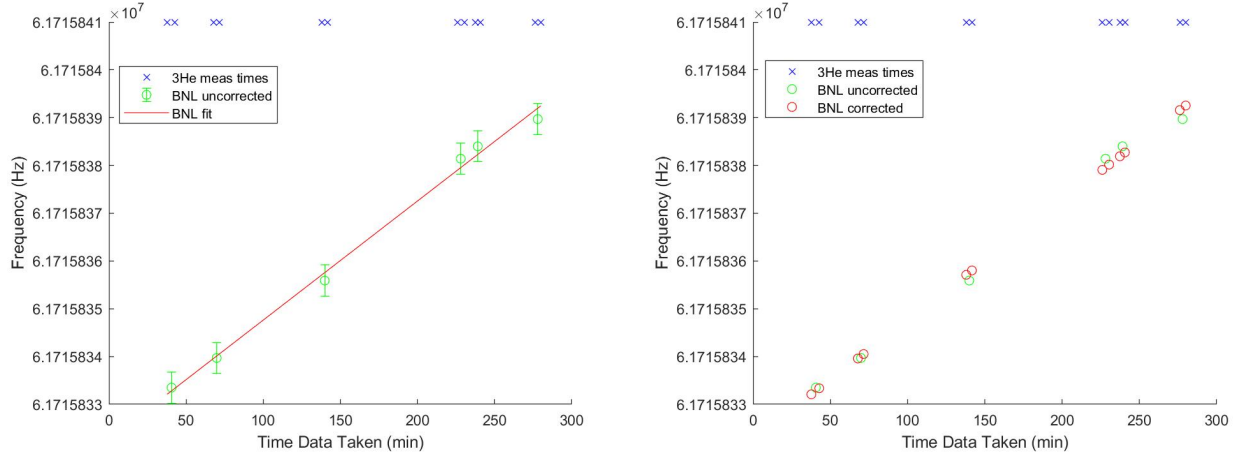
To correct for this drift, we plotted the BNL measurements as a function of time (t_2) and imposed a linear fit. The data and fit are shown in Figure 6.5a where the blue x's indicate the times t_1 and t_3 of the ^3He measurements. The slope and intercept from the uncorrected BNL measurements, 0.024 ± 0.002 Hz/min and 61715832.08 ± 0.34 Hz, respectively, are used to compute BNL frequency values at times t_1 and t_3 when the ^3He probe measurements were made. These values shown in Figure 6.5b are effectively what the BNL probe would measure if the BNL and ^3He measurements were performed simultaneously. Using these corrected values thus eliminates the effects of linear drift over the course of the cross-calibration – about 5 hours. The error on this correction is $\sigma_{lin-drift} = 0.34$ Hz (5.5 ppb) given by:

$$\sigma_{lin-drift} = \frac{1}{N} \left[\sum_{i=1}^N \sigma_{slope} * t_i \right]^2 + \sigma_{intercept}^2 \quad (6.10)$$

where N is the number of BNL measurements, t_i is the time of each measurement, and σ_{slope} and $\sigma_{intercept}$ are the errors on the extracted slope and intercept, respectively. Note that all measurement and fit errors on the uncorrected BNL frequencies get propagated here to yield the uncertainty on the corrected values.

6.3.2 BNL Bulk Correction

The bulk correction for the BNL probe accounts for the shape of the water sample holder and has the form $\delta^{bulk} = (\varepsilon - 4\pi/3)\chi_p$, where $\chi_p = -0.720(2) \times 10^{-6}$ is the susceptibility of water [58] [55]. The factor $\varepsilon - 4\pi/3$ is a measure of the sphericity of the sample holder and is $\varepsilon = 2\pi$ for an infinite cylinder with its axis perpendicular to the field. This gives the correction for the cylindrical BNL probe $\delta^{bulk} = -1508 \pm 4.2$ ppb. A cross-calibration of the cylindrical and spherical BNL probes conducted by Fei et al. [55] listed an experimental



(a) Frequency measurements with BNL probe as a function of time. (b) BNL probe frequencies corrected to ^3He frequency times

Figure 6.5: BNL probe measurements before and after linear drift correction. The blue x's mark the ^3He measurement times. The error bars of 0.2 Hz (not shown in (b)) are from the fit model dependence of the frequencies, as described in section 6.5.1.

uncertainty of 10 ppb on this correction based on their measurements with each probe. However, we use the theoretical correction and uncertainty here to keep the cross-calibrations of the two water probes with the ^3He probe independent of one another since the experimental uncertainty reported was dependent on both BNL probes. Additionally, χ has a small temperature dependence ~ 0.02 Hz (0.3 ppb) [59], [60], negligible for this work.

6.3.3 BNL Materials Correction

We make two materials corrections to the BNL measurement, one for the materials that make up the probe itself, and another for all surrounding materials not part of the probe. The probe materials correction is taken directly from Fei [55], the group that built the probe: $\delta^{probe-mat} = 47 \pm 10$ ppb. This includes perturbations from the copper NMR coil, the probe case, and the glass container (cylindrical in this case). The group also found that rotation of the probe about its axis caused frequency shifts due to the asymmetry of the probe materials. This introduced an additional uncertainty of 20 ppb [55].

For materials surrounding the probe, i.e. the ^3He probe and translation stage (platform),

we employed another NMR probe constructed by the UW group for E989 and based on protons in petroleum jelly. This probe was useful due to its small size (0.8 cm diameter and 10 cm cylinder length). Keeping the entire cross-calibration setup (probes holder on diving board on 1D stage) unchanged, we first removed the BNL probe while keeping the ^3He probe mounted. We then moved the 1D stage to the position where measurements with BNL were made. Next, the UW NMR probe, mounted vertically on a motorized stage movable in all 3 dimensions, was moved to the location where the BNL probe sat during the cross-calibration, as shown in Figure 6.6. We checked that the active volume of the NMR probe was in the same position as the BNL active volume by using the $\Delta B=0$ method in all three directions. Once the position was confirmed, a measurement of the field value with the optimal currents described in section 6.1.2 was taken.

The 1D stage was then moved out and the field of the magnet was measured with the UW NMR probe in the same position as the measurement with the 1D stage (as verified by $\Delta B=0$ again). The difference between the frequency of the NMR probe placed in the BNL position in the cross-calibration setup and the frequency of the NMR probe in the ambient magnetic field gave the perturbation due to all the materials not part of the BNL probe:

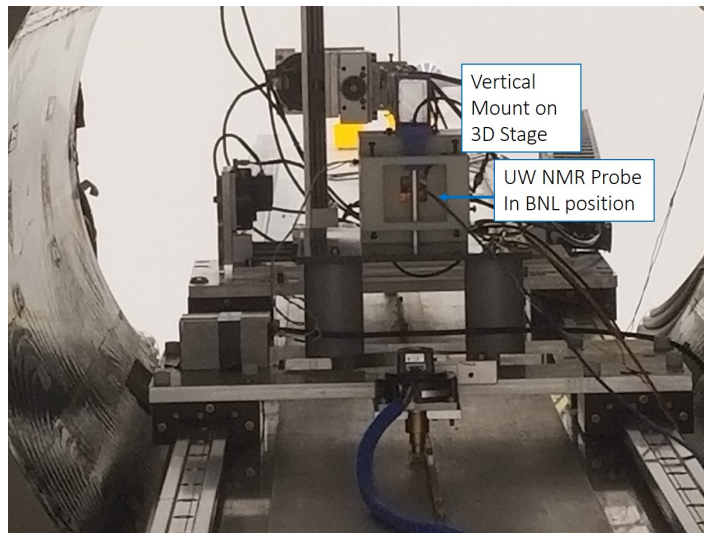


Figure 6.6: UW NMR probe mounted on 3D stage and inserted into cross-calibration setup with active volume in BNL nominal position.

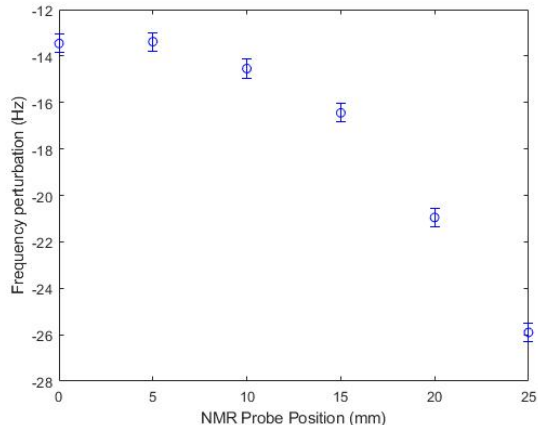


Figure 6.7: Perturbation due to materials shown as a function of y-position. 0 mm marks the position of the BNL probe active volume and gives the $\delta^{other-mat}$ correction. The error bars are due to frequency changes resulting from position uncertainty.

$\delta^{other-mat} = 224 + / - 8$ ppb, where 8 ppb is the uncertainty, $\sigma_{other-mat}$ from three different measurements. We also performed a y-axis scan with the NMR probe within the probes holder to study how the material perturbation changed around the area where the BNL probe active volume was nominally positioned. The same scan was conducted with the materials removed from the magnet and the difference between the two scans (the perturbations from the materials) are shown in Figure 6.7) as a function of position in y.

6.3.4 Other BNL Corrections

Since the shielded γ ratio in equation 6.9 is measured with water at 25°C, we must make a correction for temperature changes. We monitored the temperature of the BNL probe with a temperature sensor, PT1000 [61], which remained at 23.0 +/- 0.2°C throughout the cross-calibration effort. This gave a temperature correction of $\delta^{temp} = a\Delta T = -20.72 + / - 2.1$ ppb, where a is -10.36 +/- 0.30 from [62].

The last effect we considered was radiation damping caused by induction current produced due to the detuning of the NMR coil. Fei et al. [55] saw no radiation damping correction. We conducted a separate study with the cylindrical BNL probe, similar to the ^3He magnetization dependence study in Section 6.4.1, and found this effect to be negligible.

6.4 ^3He Corrections

The corrections made for the ^3He probe include a magnetization dependent correction, a glass correction, and frequency shifts from all materials besides the glass. It is important to note here that the bulk correction (due to the bulk magnetism of the sample) is not made by itself but instead is part of the magnetization dependent effect. If the same approach as the BNL probe were used for ^3He , we would have (using $\varepsilon = 4\pi/3$ for a sphere) a correction of $\delta^{bulk} = (\varepsilon - 4\pi/3)\chi_3 = 0$ for a spherical cell. However, the ^3He gas container is not a perfect sphere and has a stem, so the effect is nonzero. Since the effective susceptibility which includes perturbations is $\chi^{eff} = \mu_0 M/B_0$, the bulk effect directly contributes to the magnetization M . Hence we studied frequency shifts caused by the magnetization of the sample, $\delta^{mag-dep}$, which include shifts from the bulk effect, instead of conducting a separate bulk effect study (or using 0 from the theoretical prediction). The correction $\delta^{mag-dep}$ also includes shifts due to effects of the oscillating current induced in the NMR coil, an effect known as radiation damping.

6.4.1 ^3He Magnetization Dependent Effect Correction

Since the ^3He NMR signal is created by the precessing nuclei, the FID amplitude is directly proportional to the magnetization in the sample. Specifically, the amplitude of the signal produced after the $(k+1)$ th NMR pulse is proportional to the magnetization in the sample just prior to this pulse, or at the time of the k th pulse. Hence to obtain a relationship between frequency and magnetization we must compare the FID amplitude produced after the $(k+1)$ th pulse with the frequency of the FID measured for the k th pulse:

$$f^k \sim M_z^k \sim A^{k+1} \quad (6.11)$$

For this study, we analyzed 5 FIDs from each A-data set with 12 total sets from the 6 ABA campaigns (2 A-sets per ABA). Since these 5 FID signals are produced after the same

initial polarization of the sample, the amplitude decays after each pulse as it is proportional to the sample polarization and hence magnetization. Additionally, the probe remains in the same position for these five measurements so we need not take frequency differences due to position into account. Of the 12 A datasets, we only analyzed those for which the amplitudes decayed with respect to pulse number to ensure consistency with the model. Due to this, 10 of the 12 sets were analyzed (dataset numbers 2-4, 8-9 listed in Table A.1 in Appendix A). We fit the frequencies(k) as a linear function of the (k+1)th amplitudes as shown in Figure 6.8a for one of the data sets. The correction is given by:

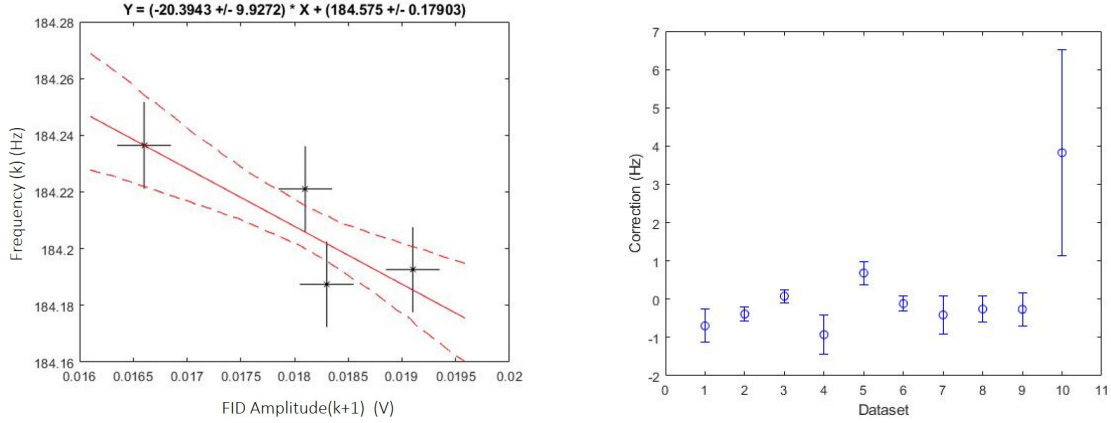
$$\Delta f = m_{fit}A_{max}, \quad (6.12)$$

where m_{fit} is the slope of the fit and A_{max} is the maximum amplitude of the FID signals (generally the maximum amplitude corresponds to the k=1 pulse). Since the slope of the fit is a measure of how the frequency shifts as the amplitude (or the magnetization) changes, this equation corrects to the value of the frequency which would be measured if there were no magnetization in the sample.

A weighted average of this correction for all data sets (given in Figure 6.8b) showed that the frequency shifted by $\Delta f_{avg} = -0.12 \pm 0.12$ Hz due to sample polarization. This may be consistent with ≈ 0 , which is expected. We provide a calculation in Appendix B to estimate this effect to be 0.2 mHz (ppt level). Additionally, our University of Michigan HeXe EDM group found this effect to be on the sub-ppb scale using similar cells [47]. Since the frequency shift from the ABA data is negative, we must add its absolute value back to the measured frequency to make the correction: $\delta^{mag-dep} = +2.6 \pm 2.6$ ppb. The uncertainty is calculated using:

$$\sigma_{mag-dep} = \sigma_m(A_{max} + \sigma_A), \quad (6.13)$$

where σ_m is the error on the slope from the linear fit and σ_A is the uncertainty on the amplitude from the FID fit.



(a) Magnetization dependence of the frequency for one dataset. The error bars are determined from 68% confidence interval of the extracted frequency and amplitude values from the Matlab fit.

(b) Magnetization dependent correction and error for all 10 datasets. The error bars are determined by propagating errors from each fit, such as the one shown in (a), using equation 6.13.

Figure 6.8: Magnetization dependent study (a) and corrections (b)

The 6 ABA data sets analyzed above were conducted with the cell stem oriented vertically in the $+y$ direction in the magnet. While these data sets were taken for the cross-calibration, we additionally performed two separate ABA campaigns with the stem pointing along the magnetic field ($+z$ direction) to study any effect caused by the rotation. Two of these 4 ABA datasets (6A and 6A' listed in Table A.1 in Appendix A) were also analyzed to determine the magnetization effect which was found to be: $\Delta f_{z-axis} = 0.5 \pm 0.4$ Hz, which is also close to 0. The theoretical prediction in Appendix B predicts the same (almost 0) effect for both stem orientations. The discrepancy in the measured values could be due to detuning of the NMR coil in between measurements since the effect includes contributions from radiation damping. Note that while we used both magnetization dependent corrections – stem in y and stem in z – in the next section before studying the glass effect, we only made the y -orientation correction for the cross-calibration as this was the stem orientation used during the calibration campaign.

6.4.2 ^3He Glass Correction

The asphericity of the glass cell holding the ^3He gas, the stem of the cell, and the glass itself all give rise to material effects which we correct for with δ^{glass} . Since glass is diamagnetic, the cell creates a shielding effect proportional to χ^2 which is very small for a perfect sphere when $\chi \ll 1$ [55], [63] (see calculation in Appendix B). Since the cell is not a perfect sphere, we study these effects empirically by rotating the cell about different axes and observing the frequency changes. To do this, we first correct the frequencies from each study to zero polarization (magnetization) using results from the previous section so the observed frequency changes can only be attributed to the glass. Note that the spherical BNL probe (discussed in section 6.7) also contained a thin stem but due to the geometry of the probe, the stem rotation study we outline for ^3He in this section was not done by Fei and the rotation of the entire BNL probe was studied [55] instead.

Since the glass stem is diamagnetic, we hypothesize that the stem behaves as a dipole with the induced magnetic dipole field aligned opposite \vec{B}_0 . We predict that this induced dipole field impacts the measured field value so that the ^3He frequency measured is proportional to the difference $B_0 - B_{dip}$. A first sign of this effect was seen when different T_2^* values were measured with the stem aligned parallel and perpendicular to the field. We know that a dipole aligned with the field would cause larger gradients than one aligned perpendicular to the field since the field of a dipole is given by $P_2(\cos\theta)$, where θ is the angle between the magnet's field and the dipole. In the motional narrowing regime (Chapter 3), a gradient along the B-field direction causes T_2^* to decrease for a sphere:

$$\frac{1}{T_2^*} = \frac{1}{2T_1} + \frac{8\gamma^2 R^4}{175D} |\nabla_z B_z|^2 \quad (6.14)$$

Hence, if the stem creates a dipole field as we predict, the T_2^* of the FID signal should be shorter when the stem is aligned with the field than the T_2^* measured when it is perpendicular to the field. We indeed measured a much shorter T_2^* , 0.75 s vs. 1.5 s, as shown in Figure 6.9.

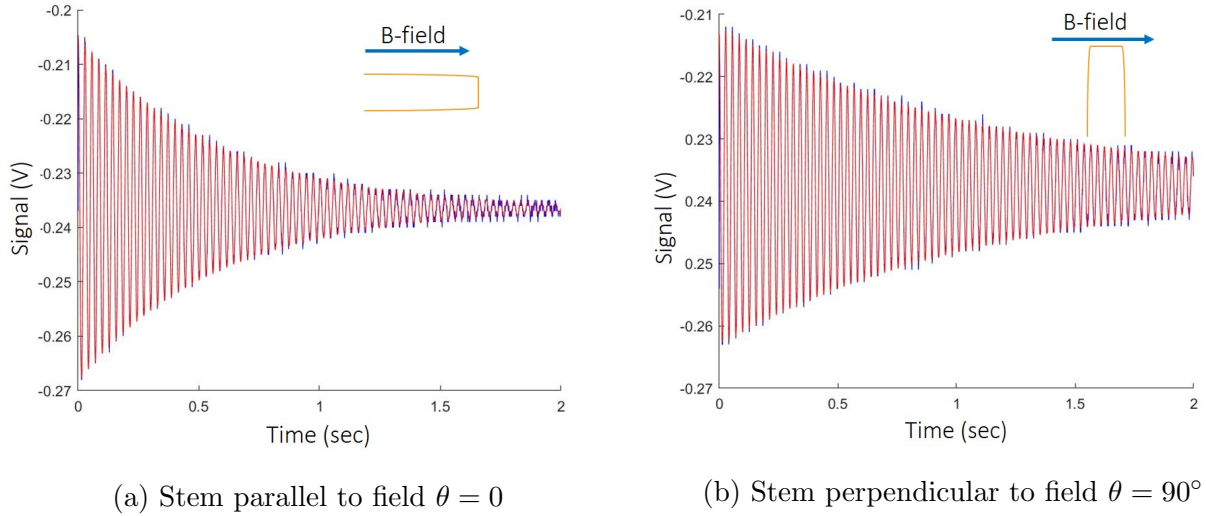
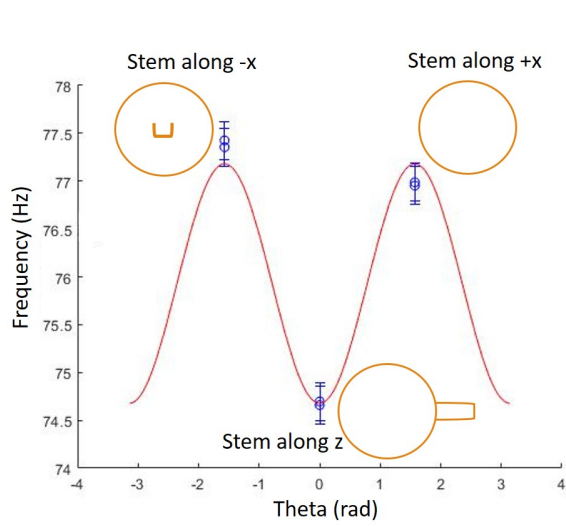


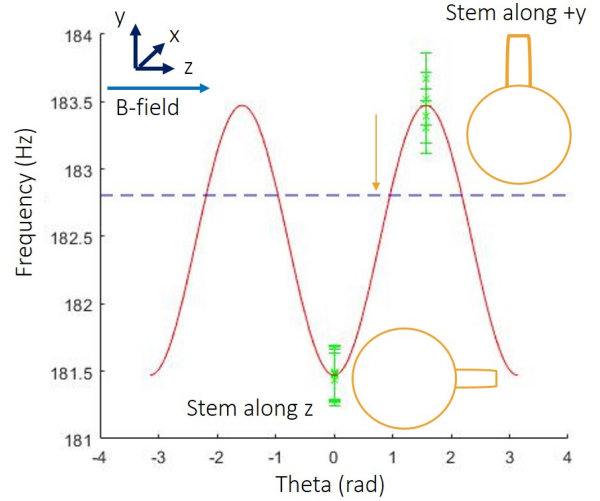
Figure 6.9: Shorter T_2^* measured with stem parallel to field than when it is perpendicular.

We model the stem as a dipole to determine its effect on the frequency by varying the angle θ between the stem (the dipole) and the magnetic field, and fitting the data to $P_2(\cos\theta)$, which is the field caused by a dipole. Ideally, we would have liked to study this effect with at least three measurements, or three different θ values, in the y-z plane since our cross-calibration is performed with the stem in the +y direction and the magnetic field is in the +z direction. However, while the positions with the stem pointing along the field ($\theta = 0$, +z direction) and perpendicular to the field ($\theta = 90^\circ$, +y direction) were achievable (Figure 6.11b), the stem pointing in a direction opposite to either of these ($-z$: $\theta = 180^\circ$ or $-y$: $\theta = 270^\circ$) were not. Pointing the cell stem along $-z$ would block the optical pumping beam and prevent hyperpolarization, making it impossible to measure the field in this orientation, and the design of the ^3He mount (Figure 5.4) did not allow enough room to point the stem in the $-y$ direction.

Instead, three θ positions were experimentally viable in the x-z plane, so we conducted a study separate from the cross-calibration campaign with the stem pointing in +x ($\theta = 90^\circ$), +z ($\theta = 0$) and $-x$ ($\theta = 270^\circ$). This study is also a test of our model since the stem aligned in +z (or +x) would give a measure of the dipole aligned with the field (or perpendicular to the field). We fit the extracted frequencies from these measurements to $P_2(\cos\theta) = 3\cos^2(\theta) - 1$



(a) Stem rotation in xz plane.



(b) Stem rotation in yz plane with data corrected to zero polarization. The arrow indicates the resulting glass correction.

Figure 6.10: $P_2(\cos\theta)$ fit of stem rotation about field in (a) x-z and (b) y-z planes. Note that the frequency offset in (a) between the two x-positions is due to magnet drift and accommodated for by the error bars. The error bars in both (a) and (b) are due to the frequency spread from the uncertainty in positioning the angle of the stem. The y-scales are different for the two figures.

as shown in Figure 6.10a, which shows consistency with our model of the stem as a dipole. The amplitude from the fit is 0.8 ± 0.3 Hz. We only used three data points here as it was not practical to measure other angles to further confirm the P_2 dependence.

Once the model was verified, we could go back to our measurements in the y-z plane, stem pointing in +z and then +y, taken during the cross-calibration campaign. Before analyzing this data, we first corrected for the magnetization dependent effect to ensure that the only effect measured in this study would be due to the stem. Hence we first added the $\Delta f_{y,z}$ from the previous section to the frequencies taken with stem in the +y and +z directions, and then fit with a P_2 as shown in Figure 6.10b.

According to the model, there exists a unique angle θ between the stem and the field at which the dipole contribution/effect on the field is 0. The amplitude of the fit in Figure 6.10b gives the frequency offset from this “0” position caused by the stem when it is oriented along the y-direction ($\theta = 90^\circ$). Since this is the orientation used for the cross-calibration,

the fit amplitude and uncertainty give the glass correction: -0.6 ± 0.2 Hz ($\delta^{glass} = -13 \pm 4.3$ ppb). Note that the sign of the frequency shift is negative due to the negative susceptibility of glass. Alternatively, if the cross-calibration was performed with the stem pointed along the magnetic field ($\theta = 0$), the shift would be twice as large and in the opposite direction since the offset from the “0” point to the $\theta = 0$ position is two times the fit amplitude ($3\cos^2(\theta) - 1 = 2$ for $\theta = 0$).

Additionally, we note that the amplitude from the y-z rotation (0.6 ± 0.2 Hz) is consistent with the amplitude from the x-z rotation study (0.8 ± 0.3 Hz) even though no magnetization dependent correction was made for the latter. This is because the NMR coil tuning, which contributes to the magnetization dependent effect, was different when the x-z rotation was conducted and the frequencies showed no magnetization dependence when plotted against the amplitude (proportional to magnetization), while a dependence was seen for the cross-calibration data. As a double check, another y-z rotation study was conducted when no magnetization dependence was seen. This data was fit to a P_2 without any correction for the magnetization and yielded an amplitude of 0.6 ± 0.1 Hz, again consistent with the other two studies. The three studies confirm that the measured glass correction is valid and also show that the magnetization dependence effect arises mostly from the coil detuning.

In addition to measuring the dipole effect of the stem by rotating the cell to align the stem along different axes, we also studied the effect of rotating the cell around the z and the y axes while keeping the stem stable (pointed in the same direction - the axis of rotation). One set of measurements was conducted with the stem pointing along the magnetic field direction (+z) and rotating the cell about the z-axis. The measured frequencies were plotted against the four angles used in the rotation and provided the scale of the effect due to the shape and materials of the cell. For example, any asymmetry in the sphericity of the cell can cause the frequency to shift. Additionally, if there is a small lump on one side of the cell it could cause a perturbation much like the observed dipole effect of the stem. Lastly, there was a piece of scotch tape on the cell for identification purposes, which could also behave as

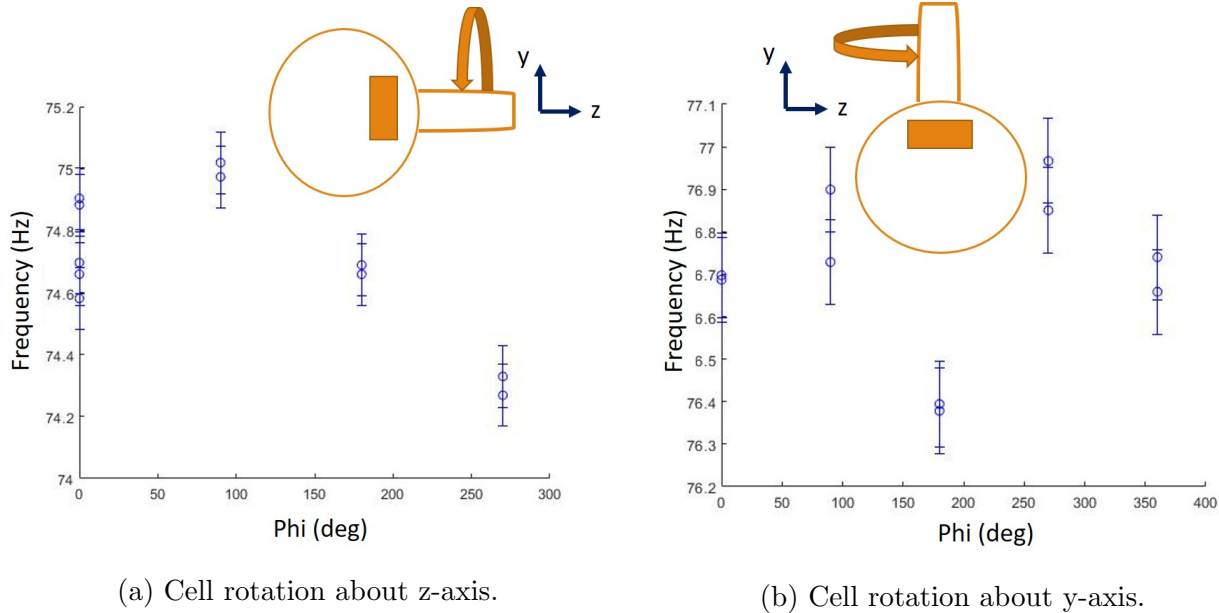


Figure 6.11: Frequency spread when cell rotated with stem held fixed. The error bars in both (a) and (b) are due to the frequency spread from the uncertainty in positioning the angle of the stem. Note the y-scales are different for the two figures.

a dipole and contribute to the changes in frequency seen.

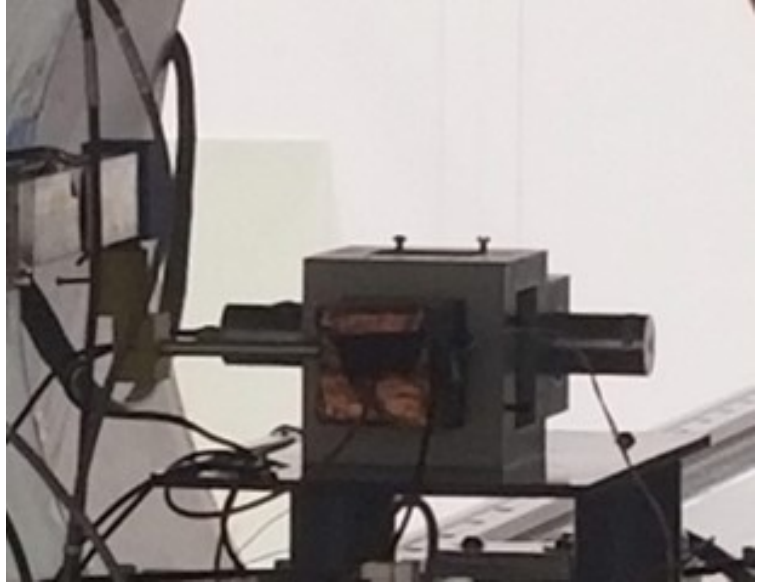
We then performed a set of measurements with the stem pointed in $+y$ while rotating the cell about the y -axis, and saw a smaller change in the frequency values. Since $+y$ was the orientation of the stem used during the cross-calibration, this last study provided the uncertainty on the frequency measurement due to shape, materials, and asphericity of the glass cell: ± 0.35 Hz (7.4 ppb), half of the maximum (peak-peak) variations 0.7 Hz.

6.4.3 ^3He Material Corrections

Since the glass correction is accounted for in the previous section, the materials correction for ^3He did not include the glass cell. The perturbation due to the remaining materials within and outside the probe were measured with the UW NMR probe and the $\Delta B=0$ method, just as was done for materials outside the BNL probe. The ^3He mount was designed with this goal specifically in mind and contained slots on either side of the mount through which the NMR probe could be slid in and placed where the ^3He cell nominally sits. After finishing



(a) UW NMR Probe mounted on 3D stage using one-sided mount.



(b) UW NMR Probe being inserted into ^3He mount.

Figure 6.12: Apparatus for measuring ^3He materials perturbations.

the cross-calibration campaign, we removed the sample cell from the mount, and placed the mount back in the same position in the ivory probes holder sitting on the 1D stage. The stage was moved back to the position used for ^3He measurements.

The NMR probe was mounted on the 3D stage with a different mount than used for BNL materials measurement. Here we used a 3D printed mount designed specifically to hold the probe from one side so that the other side of the probe hung free (see Figure 6.12a). The 3D stage was controlled to slide the NMR probe into the position of the ^3He cell within the ^3He mount. Figure 6.12b shows the probe being inserted. We tried to position the NMR probe active volume in the same location as the nominal ^3He cell position using the $\Delta B = 0$ method. Due to the geometry of the setup, the saddle coil wires prevented the NMR probe from being placed exactly in the position where the cell center sits. Hence we were unable to measure the perturbation due to the materials at that spot. However, we scanned the NMR probe near that area (< 4 mm away) for various y-positions over a range of 5 mm. We then slid out the 1D stage and scanned the field of the magnet with the NMR probe in the same range (this was verified with $\Delta B=0$). The difference between the two frequency ranges, 31

Hz, gave the perturbation due to the probe and other materials for ^3He . Based on these scans and the known gradients in the magnet, the material perturbations were found to be $\delta^{mat} = 502 \pm 24$ ppb. The uncertainty here is large compared to all other corrections due to the position offset of this measurement.

6.4.4 Other ^3He Corrections

The temperature dependence of the ^3He susceptibility is much smaller than water, hence we need not take this correction into account.

6.5 Other Errors

Table 6.1 lists all the individual BNL and ^3He probe corrections from the previous two sections, as well as the global corrections. The global errors are those that are the same for each frequency measured by a probe, including the measurement uncertainty due to statistics, the precision of the DAQ clock, and position repeatability of the probes, all explained below. Lastly, we list the uncertainty on the ratio of the shielded γ 's used to compare the BNL frequency to the ^3He frequency [27].

6.5.1 Uncertainty from Frequency Extraction and Statistics

Each set of five measurements for an ABA data set exhibited some frequency spread. The standard deviation of this spread for each measurement provided a statistical uncertainty on the measured frequency value. For the BNL probe this was 0.05 Hz (0.8 ppb with respect to proton NMR frequency 61.7 MHz), while for the ^3He probe, this was 0.06 Hz (1.3 ppb with respect to Helium-3 NMR frequency 47 MHz). Additionally, the BNL probe extracted frequencies were found to be dependent on the fit model while the ^3He frequencies were not. Based on this dependence detailed in Appendix A, we assigned an uncertainty to our frequency extraction method for the BNL probe $\sigma_{freq-extr} = 0.3$ Hz (4.9 ppb). This

Effect	Correction (ppb)	Uncertainty (ppb)
BNL Probe		
Linear Drift	few ppb	5.5
Bulk effect	-1509	4.2 [58]
Probe materials	47	10 [55]
Probe rotation	–	20 [55]
Other materials	224	8
Temperature	-20.72	2.1
Radiation Damping	–	small
Frequency Extraction	–	4.9
Frequency Statistical	–	0.8
Position Repeatability	–	4.1
BNL Probe Total Uncertainty: 24.8 ppb		
³ He Probe		
Magnetization Dependence	2.6	2.6
Glass correction (stem)	-13	4.3
Glass correction (rot)	–	7.5
Materials	502	24
Frequency Statistical	–	1.3
Position Repeatability	–	4.1
³ He Probe Total Uncertainty: 26 ppb		
Clock stability	–	0.2
Gamma ratio γ'_3/γ'_p	0.7617861313	4.3 [27]
Cross Calibration Total Uncertainty: 36.4 ppb		

Table 6.1: Cylindrical BNL probe cross-calibration with ³He probe: all corrections and uncertainties. The final error of 36 ppb results from adding the uncertainties in quadrature as described in Sec. 6.6 and is with respect to proton NMR frequency 61.7 MHz.

discrepancy is due to the fact that the BNL signal is not a true exponential decay. Due to the pressure broadening in hyperpolarized ³He gas, the FID can be modeled as an exponentially decaying sinusoid and hence this effect only arises for the BNL probe.

6.5.2 DAQ Clock

The NMR DAQ frequencies, both outgoing (NMR pulse) and incoming (FID Signal), were synced using an external function generator (SRS SG382 - Option 4) with an internal Rubidium clock. We measured the uncertainty due to this clock by sending a known signal to

the DAQ, 100 Hz away from the Local Oscillator frequency as described in section 5.3.2. The frequency of this signal was measured through the DAQ on LabVIEW, just as the NMR FID signals from either probe. Over a set of 200 measurements, we found that the frequency values changed by 0.009 Hz (0.2 ppb) peak to peak, hence this error, σ_{clock} , is negligible.

6.5.3 Position Uncertainty

The uncertainty in the positioning of both probes must be taken into account as they were both moved during the cross-calibration campaign as explained in the ABA measurements section. This uncertainty was found by measuring the repeatability of the positions with the 1D stage for the z-direction, and the precision of the $\Delta B=0$ measurements for the x and y directions. As explained in section 6.1.2, the position repeatability was good to 0.2 mm, which combined with the gradient dB_z/dz , resulted in an uncertainty of $\sigma_{pos} = 4.1$ ppb for the frequency measurements.

6.6 Cross-Check and Error Propagation

All ABA data for the cross-calibration are listed in Appendix A. Here we give the final averaged results after all corrections are made.

6.6.1 Error propagation for BNL

Each BNL frequency measurement has some uncertainty from the DAQ clock, uncertainty from the position measurement and uncertainty from the fit due to frequency extraction as well as statistical frequency fluctuations. The measured frequency for each measurement i is:

$$\omega_{p,i}^{meas} = 2\pi(f_{extracted} + 61715400) \quad (6.15)$$

with a combined error of:

$$\sigma_{\omega_{p,i}^{meas}} = \sqrt{\sigma_{clock}^2 + \sigma_{freq-extr}^2 + \sigma_{freq-stat}^2 + \sigma_{pos}^2}, \quad (6.16)$$

where σ_{clock} is negligible. The $\omega_{p,i}^{meas}$ frequency values are then used to find the linear drift of the magnet and correct for it as explained in section 6.3.1, producing the corrected frequency values $\omega_{p,i}^{lin-drift}$. As the above error on each frequency $\sigma_{\omega_{p,i}^{meas}}$ is used in the fit, the error given by the fit on the fit parameters (slope and intercept) is correlated with $\sigma_{\omega_{p,i}^{meas}}$. Hence, we need not propagate these errors into $\sigma_{\omega_{p,i}^{lin-drift}}$, which is calculated by combining the errors from the fit parameters σ_{slope} and $\sigma_{intercept}$:

$$\sigma_{\omega_{p,i}^{lin-drift}} = \frac{1}{N} \left[\sum_i^N (t_i \sigma_{slope}) \right]^2 + \sigma_{intercept}^2 \quad (6.17)$$

where t_i are the times at which we compute the new frequency values, and N is the number of t_i 's. Once the linear drift has been accounted for, we can make the rest of the corrections from section 6.3: bulk correction, perturbation due to materials (both within and outside the probe), temperature correction and radiation damping:

$$\omega'_{p,i} = \frac{\omega_{p,i}^{lin-drift}}{1 - \delta_{corrections}} = \frac{\omega_{p,i}^{lin-drift}}{1 - \delta_{bulk} - \delta_{probe-mat} - \delta_{other-mat} - \delta_{temp} - \delta_{rad-damp}} \quad (6.18)$$

where the prime denotes that the value is corrected to the shielded proton measurement.

The error $\sigma_{\omega'_{p,i}}$ on this value is given by:

$$\sigma_{\omega'_{p,i}}^2 = \left[\frac{\omega'_{p,i}}{\omega_{p,i}^{lin-drift}} \right]^2 \sigma_{\omega_{p,i}^{lin-drift}}^2 + \left[\frac{\omega'_{p,i}}{1 - \delta_{corrections}} \right]^2 [\sigma_{bulk}^2 + \sigma_{probe-mat}^2 + \sigma_{other-mat}^2 + \sigma_{temp}^2 + \sigma_{rad-damp}^2] \quad (6.19)$$

After making these corrections for each frequency measurement of the BNL probe, we average the measurements to find a final value with an uncertainty 24.8 ppb:

$$\omega'_p = 61715758.45 \pm 1.53 \text{ Hz} \quad (6.20)$$

6.6.2 Error propagation for ^3He

Since we take the magnet drift into account and correct the BNL frequencies for ^3He measurement times, there is no linear drift correction for ^3He probe frequencies. Thus, the error propagation is much simpler. We start by adding the extracted frequency to the Local Oscillator frequency:

$$\omega_{3,i}^{meas} = 2\pi(f_{extr} + 47014000) \quad (6.21)$$

We then make each of the corrections explained in section 6.4:

$$\omega'_{3,i} = \frac{\omega_{3,i}^{meas}}{1 - \delta_{corrections}} = \frac{\omega_{3,i}^{meas}}{1 - \delta_{mag-dep} - \delta_{glass} - \delta_{mat}} \quad (6.22)$$

The combined error on this value is then given by:

$$\sigma_{\omega'_3} = \left[\frac{\omega'_{3,i}}{\omega_{3,i}^{meas}} \right]^2 [\sigma_{\omega_3^{freq-stat}}^2 + \sigma_{\omega_3^{pos}}^2 + \sigma_{cell-rot}^2] + \left[\frac{\omega'_{3,i}}{1 - \delta_{corrections}} \right]^2 [\sigma_{mag-dep}^2 + \sigma_{glass}^2 + \sigma_{mat}^2] \quad (6.23)$$

The result of the ^3He probe measurement is:

$$\omega'_3 = 47014209.57 \pm 1.22 \text{ Hz} \quad (6.24)$$

corresponding to an uncertainty of 26 ppb.

6.6.3 Combining Errors for a final number

Now that we have values for ^3He and BNL probe absolute frequencies, we can compare the two using the ratio of the shielded γ 's. We predict the BNL probe frequency using the ^3He measured frequency and compare it to the measured BNL value.

$$\omega_p'^{\text{predicted}} = \frac{\gamma_p'}{\gamma_3'} \omega_3' = 61715759.37 \text{ Hz} \quad (6.25)$$

with an error of

$$\sigma_{\omega_p'^{\text{predicted}}} = \sqrt{\left[\frac{\omega_p'^{\text{predicted}}}{\omega_3'} \sigma_{\omega_3'}\right]^2 + \left[\frac{\omega_p'^{\text{predicted}}}{\gamma'} \sigma_{\gamma'}\right]^2} = \pm 1.64 \text{ Hz} \quad (6.26)$$

The final number for the cross-calibration is then the difference between the predicted BNL value and the actual BNL value:

$$\omega_p' - \omega_p'^{\text{predicted}} = 0.92 \pm 2.23 \text{ Hz} \quad (6.27)$$

This corresponds to a cross-calibration of the two probes to 36.4 ppb with respect to the proton NMR frequency of ~ 61.7 MHz.

6.7 Spherical Probe Cross Calibration

The spherical BNL probe based on water was cross-calibrated with the ^3He probe using the same techniques described for the cylindrical probe calibration. Since the methods were given in detail earlier in this chapter, we only provide brief descriptions here except for when differences need to be pointed out.

In between the two cross-calibration campaigns, the field of the Argonne magnet was ramped up to 4 T for a different experiment and then back down to 1.45 T. Consequently, the currents which shimmed the passive coils to improve magnetic field homogeneity had to

be remeasured. We conducted magnetic field scans with a UW NMR probe, since it could be mounted on a 3D stage and moved in all three axes. Magnetic field scans were performed as a function of position (motor encoder bits) along the x, y, and z axes for two different current values. Based on these scans, the $\Delta B = 0$ positions were found in all three directions, as well as the currents to make the field at this point more uniform. The new current values were: $I_x = -0.14$ A, $I_y = 0.16$ A, and $I_z = -0.15$ A. The spherical probe cross-calibration campaign was carried out using these current values for the passive coils.

In order to perform the analysis for each cross-calibration separately, a new blind was implemented, this time for the BNL data. Another binary file with a random number between ± 8 Hz was generated using Matlab. This range was about half the size of the blinding implemented for the cylindrical probe calibration. The blind offset was added to each BNL frequency in both online and offline analyses, while the offset itself was kept hidden from the user. This time, the ^3He probe frequencies remained unblinded for the relative cross-calibration.

Both the spherical BNL probe and the ^3He probe were mounted in the same ivory 3D printed holder described in section 6.1.1. A new ^3He mount (top half) was used with wider slots on each side so the NMR probe could more easily measure the materials perturbation. However, the saddle coil wires were still an obstacle and the measurement uncertainty remained large (see below). The $\Delta B = 0$ positions were found for each probe and the probes were held fixed in these locations for x and y, while the movement in the z-axis was controlled with the 1D stage. Due to limited access to the magnet, 3 sets of measurements were taken for the cross-calibration over a period of 1.5 hours. An ABBA scheme was chosen as opposed to ABA in an effort to minimize linear drift effects in between measurements:

- Position ^3He probe at measurement location,
- Verify position with $\Delta B = 0$,
- (A) Measure 5 FIDs with ^3He probe,

- Move BNL probe to measurement location,
- (B) Measure 5 FIDs with BNL probe,
- Check BNL position with $\Delta B = 0$,
- (B) Measure 5 FIDs with BNL again,
- Move ^3He probe to measurement location,
- (A) Measure 5 FIDs with ^3He probe, and finally
- Verify position with $\Delta B = 0$.

The corrections for each probe, spherical BNL and ^3He , as well as the global corrections and all uncertainties are listed in Table 6.2. The corrections and uncertainties are explained in detail in the next two sections and the final result of this cross-calibration is provided.

6.7.1 BNL Probe Corrections

The same corrections, some with different values and uncertainties, were made for the spherical BNL probe as the cylindrical one. Due to the new ABBA method with less time between measurements, the linear drift of the frequencies was small and hence the correction and uncertainty were also smaller for this calibration: $\sigma_{lin-drift} = 2\text{ppb}$ (0.12 Hz). No bulk correction was necessary for the spherical water sample since $\varepsilon = 4\pi/3$ for a sphere so the bulk correction is $\delta^{bulk} = (\varepsilon - 4\pi/3)\chi_p = 0$. The correction due to materials making up the probe were again from Fei [55]: 44 ± 18 ppb. Next, the perturbation due to the materials outside the probe was measured with the UW NMR probe and the correction was found to be $\delta^{other-mat} = 178 \pm 8$ ppb. Lastly, the monitored temperature of the probe was $24.2 \pm 0.2^\circ\text{C}$, which gave a correction of $\delta^{temp} = -7.8 \pm 2.1$ ppb. All other corrections remained the same. The final BNL probe result with the above corrections is (unblinded):

$$\omega'_p = 61710229.90 \pm 1.48 \text{ Hz} \tag{6.28}$$

with a total uncertainty of 24 ppb.

6.7.2 ^3He Probe Corrections

For the ^3He probe, the gas magnetization effect was again found by checking the frequency dependence on the amplitudes for each data set A. The weighted average from all six data sets showed that the frequency shifted by $\Delta f = 0 \pm 0.2$ Hz on average. Hence we did not make a magnetization dependent correction in this case but used the uncertainty: $\sigma_{mag-dep} = \pm 4.3$ ppb. We were not able to perform any cell stem rotation studies during this cross calibration campaign due to time limitations, and instead relied on previous data for the glass correction. Since we found a consistent value for the glass stem correction from three different studies as explained in section 6.4.2, we used the same glass correction and uncertainties for this cross-calibration: $\delta^{glass-stem} = -13 \pm 4.3$ ppm and $\sigma_{cell-rot} = 7.5$ ppb.

Perturbations due to materials within and around the probe (minus the glass cell) were again measured using an NMR probe. The top half of the ^3He mount had been replaced for this cross-calibration, hence we expected the materials correction to change. The correction was found to be $\delta^{mat} = 424 \pm 26$ ppb. Again the uncertainty is due to the fact that the NMR probe could not be placed exactly at the center of the ^3He cell location, and we instead performed a scan near the area. The remaining uncertainties are the same as the previous cross-calibration. Using these, the final corrected ^3He frequency is:

$$\omega'_3 = 47009998.24 \pm 1.3 \text{ Hz} \quad (6.29)$$

with an uncertainty of 27.8 ppb with respect to Helium-3 NMR frequency.

6.7.3 Final Result for Spherical Probe Cross Calibration

All ABBA data for this cross-calibration are listed in Appendix A. Here we give the final averaged results after all corrections are made. Following the method of the cylindrical probe

Effect	Correction (ppb)	Uncertainty (ppb)
BNL Probe		
Linear Drift	few ppb	2
Bulk effect	–	–
Probe materials	44	10 [55]
Probe rotation	–	20 [55]
Other materials	172	8
Temperature	-7.8	2.1
Radiation Damping	–	small
Frequency Extraction	–	4.9
Frequency Statistical	–	0.8
Position Repeatability	–	4.1
BNL Probe Total Uncertainty: 24 ppb		
³ He Probe		
Magnetization Dependence	–	4.3
Glass correction (stem)	-13	4.3
Glass correction (rot)	–	7.5
Materials	454	26
Frequency Statistical	–	1.3
Position Repeatability	–	4.1
³ He Probe Total Uncertainty: 27.8 ppb		
Clock stability	–	2
Gamma ratio γ'_3/γ'_p	0.7617861313	4.3 [27]
Cross Calibration Total Uncertainty: 37.2 ppb		

Table 6.2: Spherical BNL probe cross-calibration with ³He probe: all corrections and uncertainties. The final error of 37 ppb results from adding the uncertainties in quadrature as described in Sec. 6.6 and is with respect to proton NMR frequency 61.7 MHz.

cross-calibration, we first predict a BNL probe measurement with the ³He probe by using

γ'_p/γ'_3 :

$$\omega'_p{}^{predicted} = \frac{\gamma'_p}{\gamma'_3} \omega'_3 = 61710231.14 \pm 1.75 \text{ Hz} \quad (6.30)$$

Finally the difference between the predicted BNL value and the measured BNL value, i.e. the result of the cross calibration is:

$$\omega'_p - \omega'_p{}^{predicted} = 1.24 \pm 2.29 \text{ Hz} \quad (6.31)$$

Hence, we cross-calibrate the spherical probe with an uncertainty of 37.2 ppb.

Chapter 7

Conclusion and Looking Forward

7.1 Summary

We have described the construction and function of a magnetometer based on ^3He gas. Studies at both low magnetic fields (10s of Gauss) and high magnetic field (1.45 Tesla) have been reported. The high field was measured absolutely in terms of the helion frequency (not free ^3He nuclei) to 26 ppb total achieved uncertainty. While Nikiel et al. have reported tracking of magnetic field changes $\delta B/B$ to 10^{-12} at high fields (>0.1 T) [64], to our knowledge the field measurement presented in this work sets a new standard on ^3He magnetometry. Additionally, the ^3He probe was used to cross-calibrate two water-based probes previously employed for the absolute calibration of the Brookhaven National Lab muon $g-2$ experiment (E821) [18]. The purpose of the cross-calibrations was to check the error on the BNL absolute probes which contributed to the uncertainty on the measured muon magnetic moment anomaly a_μ , which differed from the SM prediction by $>3\sigma$.

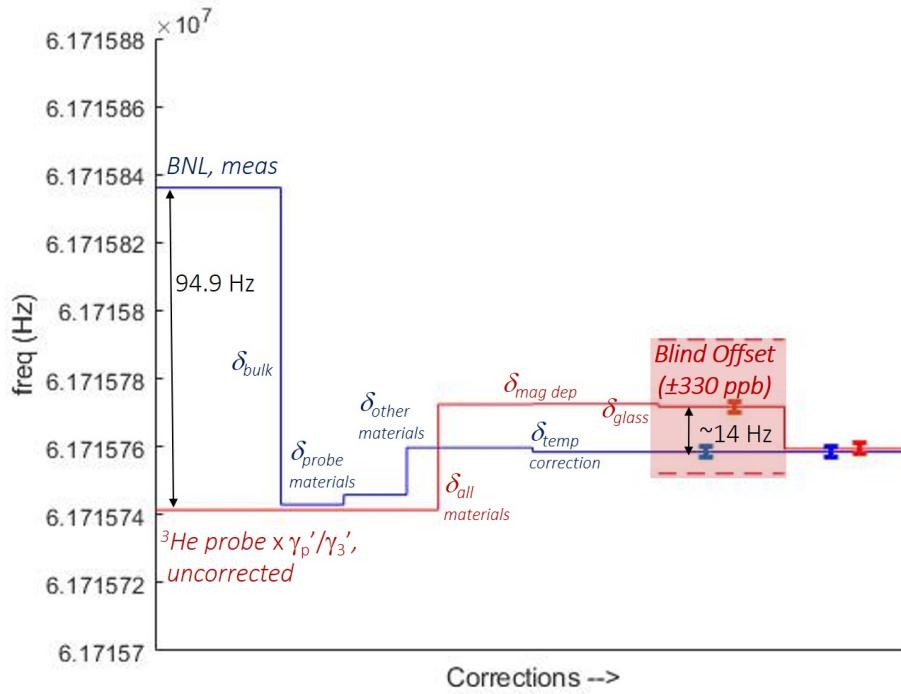
Both the cylindrical and spherical BNL probes were cross-calibrated with ^3He in a 1.45 T field by measuring the field value with each probe in the same location of the magnet with these locations found using a precise method ($\Delta B = 0$). Each of the two cross-calibration campaign was performed within a few hours (5 and 3 hours) in order to minimize field drift

effects, avoid un-mounting and remounting of the probes which could introduce material perturbations, and prevent larger magnetization dependent effects from different coil tuning. The BNL measurements were corrected to compensate for the (small) magnetic field drift and then corrected to the standard of shielded protons in water. The ^3He probe measurements were corrected to the shielded helion and then the ratio γ'_3/γ'_p was used to predict a BNL value with the ^3He measurement and compare it with the corrected BNL measurement.

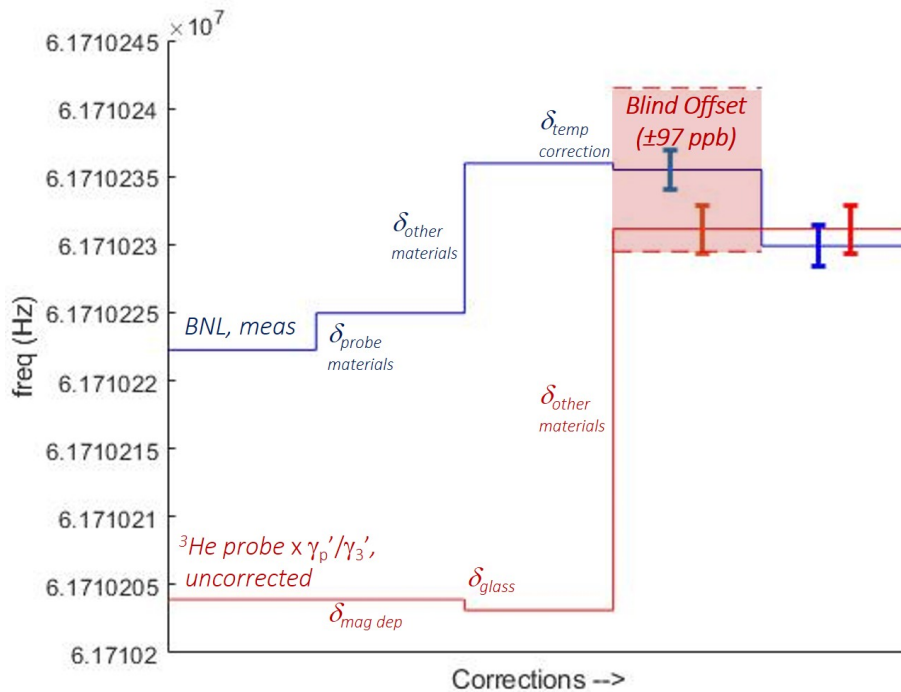
After we were confident in each value of all corrections, we unblinded the previously blinded ^3He and BNL data before the corrections were made. Figures 7.1a and 7.1b show a schematic of the corrections (not necessarily made in the order shown). The cylindrical and spherical BNL probes were successfully cross-calibrated to 36 and 37 ppb, respectively. The ^3He frequency measurements were in agreement with both probes within error and therefore we can definitively say that the discrepancy between the measured value and SM prediction of a_μ was not caused by error due to the absolute calibration in E821.

7.2 Suggestions for Future Improvements

While the cross-calibrations were performed to very high precision, it is possible to reduce some of the uncertainties in the future. The largest correction and uncertainty were due to the materials that made up and surrounded the ^3He probe. These can be reduced by 3D printing another iteration of the probe mount with a lower fill (less dense mount). The same could be done for the 3D printed holder in which both probes were mounted for the cross-calibration. These changes would reduce the ^3He materials correction. A study of different types of materials used for 3D printing could also lead to a smaller perturbation. For example, we found during some preliminary material studies that the copper shield and the PLA plastic used to 3D print the ^3He mount perturbed the field in opposite directions. A more rigorous study of these perturbations could lead to a mount design with a much lower overall materials correction from the canceling effect between copper and plastic.



(a) Schematic of corrections made for cylindrical BNL probe cross-calibration with ^3He probe with final uncertainties.



(b) Schematic of corrections made for spherical BNL probe cross-calibration with ^3He probe with final uncertainties.

Figure 7.1: Cross-calibration corrections schematics.

The large uncertainty (26 ppb) of the materials correction resulted from the fact that an NMR probe could not be placed at the position of the ^3He sample cell due to the geometry of the mount. We attempted to slide the NMR probe horizontally into the ^3He cell position using slots on either side of the mount. Alternatively, a new iteration could contain slots on the top and bottom of the mount across from the position of the sample cell, through which the NMR probe could be inserted vertically and measure at the position of the cell more precisely without interference from the saddle coil.

Another potential benefit of adding through holes on the top and bottom parts of the mount for the NMR probe is that the cell stem would be able to fit in this slot. This would make another cell stem orientation achievable which could then be used to perform a more rigorous stem rotation study, which was not possible with the current mount geometry. In general, it would also be beneficial to conduct further rotation studies in all three planes x-y, y-z, and x-z, which were not carried out for this work. Given more time, these measurements could be performed for more than just three angles of the stem, which would increase the confidence level in the dipole model of the cell stem.

Lastly, while this dissertation work only used one ^3He sample cell for the cross-calibrations due to time restraints, it would be advantageous to employ more cells. The next iteration of cells could be constructed more carefully to have a more spherical shape, which would reduce the uncertainty from the glass rotation. As described in Chapter 2, each cell would give rise to a different set of systematic errors, such as the stem rotation effect, which would increase the level of confidence in the cross-calibrations.

7.3 Future Measurements Scope

In addition to providing better cross-calibrations of the BNL water probes, an improved ^3He magnetometer (as well as the current one) could be used to cross-calibrate the water probes (made by University of Massachusetts group) currently employed for the absolute

calibration effort of the muon g-2 experiment at Fermilab (E989). While the E989 goal for the field measurement calibration was proposed to be 34 ppb [24], the probes have been shown to measure the field with even smaller errors. Hence, a cross-calibration with an independent system would be extremely useful for an experiment planning to measure the muon magnetic moment anomaly to highest precision yet. If any discrepancies continue to be seen with theoretical predictions, the proposed cross-calibration of the water probes with the ^3He probes would be essential.

The cross-calibration reported in this work relied on the shielded proton to shielded helion ratio (γ'_3/γ'_p) from [27]. Future possible measurements of the unshielded helion gyromagnetic ratio to a few ppb as proposed in [65] and [66] could provide an absolute calibration of the magnetic field measurement for E989. Alternatively, the cross-calibration with the water probes from this work could yield a measurement of the helion gyromagnetic ratio by using the unshielded proton magnetic moment standard.

Appendix A

NMR Fitting and Tabulated Cross-Calibration Data

The function used to fit the ^3He NMR FID data in Matlab was an exponentially decaying sinusoid (as given in Chapter 4):

$$V(t) = A + B\cos(\omega t + \phi)\exp(-t/T_2^*) \quad (\text{A.1})$$

where A is an offset, B is the signal amplitude, $\omega = 2\pi f$ is the mixed down frequency, ϕ is the phase, and T_2^* is the transverse relaxation time discussed in Section 3.3. The weights for the data points used for fitting were determined from the average noise level, which was measured by acquiring data with the NMR electronics without polarizing the gas or sending an NMR pulse. Figure A.1 shows an example of a high-field FID fit with residuals – the difference between fit function and the data. The small values of the residual points distributed randomly about 0 validate this fit model as does the value of χ^2 per degree of freedom = 0.9.

In a cell of ^3He gas, the atoms move around and sample different parts of the cell and hence experience different magnetic fields. Due to this pressure broadening effect, the T_2^* relaxation times for higher pressure gases can be longer [45]. Since the probability of this

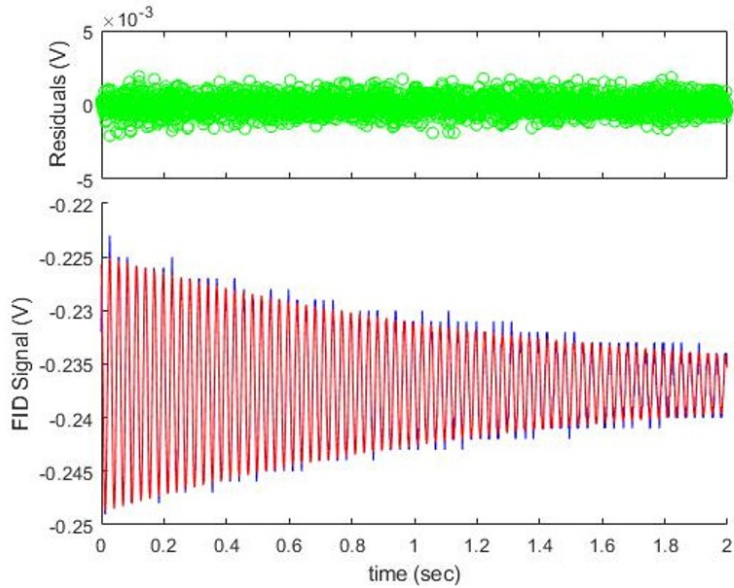
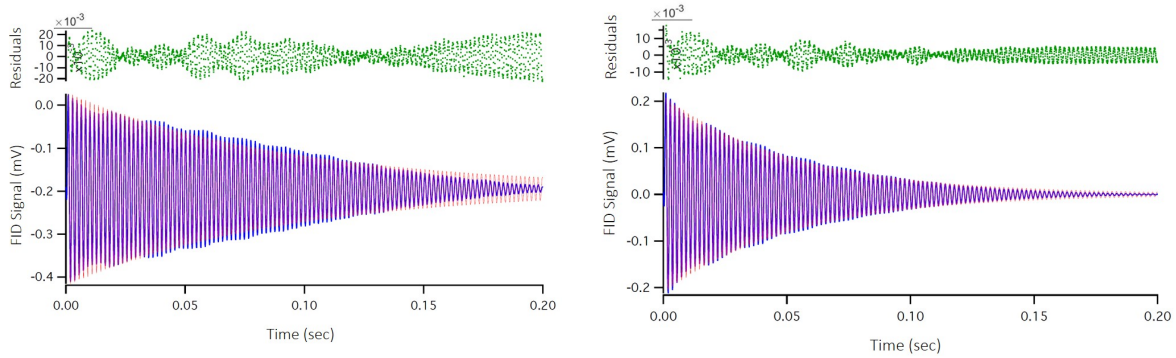


Figure A.1: High field FID data (plotted in blue), fit (red), and residuals (green).

diffusion of the nuclei is exponential in time, the ^3He precession signal is an exponentially decaying sinusoid. The water magnetization, on the other hand, does not exhibit the same behavior since the water molecules are stationary. Hence the NMR signals are not accurately exponential decays. Thus, using the function in A.1 to fit the water data does not work very well. We show an example fit in Figure A.2a with a $\chi^2/dof = 3.8$. Note the χ^2 calculation



(a) Raw BNL probe data (blue) analyzed using equation A.1 (red). The residuals are plotted in green.

(b) BNL data multiplied by envelope function (blue) and then fit to A.1 (red). The residuals are plotted in green.

Figure A.2: BNL data fit using two methods. Note that there is 60 Hz noise which causes the shape of the residuals. The fit amplitude does not change.

assumed uniform voltage noise on the signal of 0.048 V for the fits shown.

Since our FID fit model from Equation A.1 is not accurate for water FIDs, we multiplied the signal by a damping factor $e^{-t/T_{damp}}$ after removing the offset, found by averaging the y-data points. Here we used T_{damp} shorter than the extracted T_2^* value from the first fit attempt from Figure A.2a to ensure that the amplitude decay is dominated by the damping exponential. We then analyzed the new data with the same fit function from A.1 as shown in Figure A.2b which resulted in a much better fit: $\chi^2/dof = 0.6$. These new extracted frequency values were used for the cross-calibration and a fit model dependent uncertainty of 0.3 Hz was used due to frequency shifts seen between the two fitting methods.

The extracted fit parameters – the (unblinded) frequency, T_2^* , and amplitude – of each FID cross-calibration dataset are tabulated below. The uncertainty from the fit on each parameter is also listed. Table A.1 lists all the ^3He data from the cylindrical probe cross-calibration. Each ABA cross-calibration consisted of 5 FIDs. The table lists fit parameters for each of these 5 FIDs for each dataset where the prime (such as 2A') denotes the second 'A' in 'ABA.' Datasets numbered 2-4 and 7-9 (total 12) were taken with the cell stem oriented along the y-axis and were directly used for the cross-calibration. Datasets 5-6 (total 4) were taken with the stem oriented along the z-axis (magnetic field direction) and were only studied to determine the polarization dependence and glass corrections. Table A.2 similarly lists all the data for the 'B' measurements in 'ABA' numbered 2-4 and 7-9 (total 8).

The spherical probe cross-calibration data is then listed in Tables A.3 and A.4 for the ^3He and spherical BNL probes. Since an ABBA cross-calibration scheme was employed, the tables list the A, A', B, and B' fit parameters and uncertainties. All ^3He data was taken with the stem oriented along the y-axis. Lastly, note that all data listed for both the cylindrical and spherical BNL probes was fit using the damping envelope function model discussed earlier in this appendix.

Dataset	Freq (Hz)	σ_{freq} (Hz)	T_2^* (s)	$\sigma_{T_2^*}$ (s)	Ampl (V)	σ_{Ampl} (V)
2A	183.9546	0.029	0.3162	0.0182	0.0247	0.0006
	184.0337	0.0287	0.3576	0.023	0.023	0.0006
	184.0165	0.0298	0.3579	0.0239	0.022	0.0006
	183.9794	0.0292	0.3779	0.0261	0.021	0.0005
	184.011	0.0295	0.3387	0.0213	0.0212	0.0005
2A'	184.1926	0.03	0.342	0.022	0.0194	0.0005
	184.1874	0.0301	0.3311	0.0207	0.0191	0.0005
	184.2211	0.0301	0.3458	0.0226	0.0183	0.0005
	184.2364	0.0306	0.3375	0.0218	0.0181	0.0005
	184.1629	0.0314	0.3639	0.026	0.0166	0.0005
3A	184.5614	0.0286	0.3426	0.021	0.0241	0.0006
	184.5906	0.0285	0.3355	0.0201	0.024	0.0006
	184.5649	0.0289	0.3566	0.0231	0.022	0.0006
	184.5443	0.0293	0.3338	0.0205	0.0222	0.0006
	184.5464	0.0291	0.3454	0.0217	0.0209	0.0005
3A'	184.6789	0.0304	0.3312	0.0209	0.0202	0.0005
	184.7092	0.0304	0.3353	0.0214	0.0201	0.0005
	184.7559	0.0303	0.3443	0.0225	0.0191	0.0005
	184.6946	0.0304	0.3419	0.0223	0.0187	0.0005
	184.701	0.0303	0.3308	0.0208	0.0186	0.0005
4A	185.8362	0.0293	0.3511	0.0227	0.0238	0.0006
	185.8392	0.0296	0.3464	0.0223	0.0231	0.0006
	185.8152	0.0299	0.3023	0.0171	0.0239	0.0006
	185.7885	0.0304	0.3365	0.0216	0.0227	0.0006
	185.8201	0.0299	0.3237	0.0197	0.0219	0.0006
4A'	185.9568	0.0309	0.3498	0.0237	0.0206	0.0006
	185.9794	0.0314	0.3527	0.0245	0.0194	0.0005
	186.0036	0.0314	0.3058	0.0184	0.02	0.0005
	185.9799	0.0315	0.3483	0.024	0.0185	0.0005
	185.9989	0.0325	0.3547	0.0256	0.0174	0.0005
7A	187.775	0.0419	0.3162	0.0263	0.0082	0.0003
	187.8073	0.0449	0.3122	0.0274	0.008	0.0003
	187.7588	0.0479	0.2871	0.0248	0.0081	0.0003
	187.7319	0.0499	0.3093	0.0299	0.0072	0.0003
	187.8714	0.0493	0.3071	0.0292	0.0073	0.0003
7A'	187.7181	0.0549	0.2686	0.0248	0.008	0.0004
	187.807	0.0538	0.3736	0.0471	0.0066	0.0003
	187.7289	0.0576	0.2534	0.0232	0.0076	0.0003
	187.8048	0.0555	0.3253	0.0368	0.0066	0.0003
	187.7966	0.0569	0.2976	0.0316	0.0069	0.0003

Table A.1: ^3He data from cylindrical probe ABA cross-calibration (continued on next page).

8A	187.7382	0.0324	0.2883	0.0169	0.0199	0.0005
	187.7297	0.0319	0.2908	0.0169	0.0196	0.0005
	187.7756	0.0327	0.2985	0.0183	0.0184	0.0005
	187.7653	0.033	0.2793	0.0161	0.0185	0.0005
	187.7671	0.034	0.2745	0.0161	0.0182	0.0005
8A'	187.9095	0.0349	0.2796	0.0171	0.0175	0.0005
	187.9222	0.0351	0.2879	0.0182	0.0167	0.0005
	187.9398	0.0352	0.3066	0.0207	0.0157	0.0005
	187.9243	0.0359	0.2985	0.02	0.0155	0.0005
	187.9401	0.0357	0.2948	0.0194	0.0153	0.0005
9A	188.3027	0.0294	0.4826	0.043	0.0181	0.0005
	188.3368	0.0299	0.474	0.0422	0.0177	0.0005
	188.2869	0.0308	0.4597	0.0409	0.0171	0.0005
	188.3324	0.0306	0.4885	0.0458	0.0161	0.0005
	188.3281	0.0318	0.4968	0.0493	0.0156	0.0005
9A'	188.3474	0.0325	0.4786	0.0467	0.0145	0.0004
	188.3739	0.0325	0.4691	0.0448	0.0142	0.0004
	188.3266	0.0325	0.5114	0.0533	0.0133	0.0004
	188.3631	0.0331	0.5019	0.0523	0.013	0.0004
	188.3789	0.0333	0.5559	0.0646	0.0124	0.0004
5A	185.5298	0.035	0.3987	0.0351	0.0106	0.0003
	185.5789	0.0349	0.3624	0.0289	0.0107	0.0003
	185.5437	0.0357	0.3944	0.035	0.0103	0.0003
	185.5195	0.0362	0.307	0.0215	0.0113	0.0003
	185.4826	0.0359	0.3613	0.0295	0.0105	0.0003
5A'	185.7877	0.0436	0.3113	0.0266	0.0101	0.0004
	185.7256	0.0443	0.2967	0.0246	0.01	0.0004
	185.7126	0.0435	0.3849	0.0406	0.009	0.0003
	185.6214	0.041	0.3598	0.0335	0.0093	0.0003
	185.6433	0.0453	0.3207	0.0294	0.0094	0.0004
6A	186.0181	0.0319	0.3063	0.0188	0.0168	0.0004
	186.0757	0.0304	0.3658	0.0255	0.0153	0.0004
	186.0933	0.0314	0.3425	0.0232	0.0151	0.0004
	185.992	0.0307	0.4009	0.031	0.0142	0.0004
	186.1131	0.0323	0.3586	0.0261	0.0141	0.0004
6A'	186.1693	0.0323	0.3156	0.0202	0.0146	0.0004
	186.2154	0.0328	0.3616	0.027	0.0134	0.0004
	186.1185	0.0329	0.2948	0.018	0.0144	0.0004
	186.1369	0.0319	0.3809	0.0291	0.0127	0.0004
	186.2124	0.033	0.3455	0.0247	0.0128	0.0004

Dataset	Freq (Hz)	σ_{freq} (Hz)	T_2^* (s)	$\sigma_{T_2^*}$ (s)	Ampl (V)	σ_{Ampl} (V)
2B	433.1021	0.3265	0.0667	0.0088	0.2736	0.0242
	433.1009	0.3275	0.0664	0.0088	0.2608	0.0231
	433.1493	0.3284	0.0677	0.009	0.2553	0.0225
	433.1733	0.3268	0.0669	0.0089	0.2577	0.0228
	433.2493	0.3268	0.066	0.0088	0.2609	0.0233
3B	433.6672	0.3286	0.0671	0.0089	0.2711	0.0241
	433.7635	0.3286	0.0674	0.009	0.2569	0.0228
	433.764	0.3281	0.067	0.0088	0.2568	0.0227
	433.7727	0.3296	0.0672	0.009	0.2558	0.0228
	433.7278	0.329	0.0667	0.0088	0.2573	0.0227
4B	435.3793	0.3333	0.0659	0.0088	0.2718	0.0244
	435.2542	0.3366	0.0663	0.009	0.256	0.0231
	435.2344	0.3367	0.0667	0.0091	0.2534	0.0229
	435.2197	0.3373	0.0661	0.0089	0.2558	0.023
	435.2995	0.3349	0.0659	0.0088	0.2561	0.023
7B	437.7493	0.3547	0.0645	0.0087	0.2468	0.0226
	437.8658	0.3541	0.0644	0.0087	0.2508	0.023
	437.8126	0.3549	0.0647	0.0088	0.2513	0.0231
	437.8377	0.3548	0.0642	0.0088	0.2521	0.0234
	437.7621	0.3555	0.0645	0.0088	0.251	0.0232
8B	438.029	0.354	0.0644	0.0087	0.2675	0.0245
	438.0526	0.3535	0.0648	0.0088	0.252	0.0231
	438.0983	0.3543	0.0648	0.0089	0.2507	0.0231
	438.079	0.3539	0.0647	0.0088	0.2516	0.0231
	437.9955	0.3542	0.0645	0.0087	0.2518	0.0231
9B	438.5842	0.3578	0.0632	0.0085	0.2673	0.0246
	438.6449	0.3572	0.0634	0.0086	0.2527	0.0233
	438.6447	0.3567	0.0636	0.0086	0.2515	0.0231
	438.6558	0.3549	0.0635	0.0085	0.2514	0.0229
	438.5125	0.3554	0.0636	0.0085	0.2514	0.0229

Table A.2: Cylindrical BNL probe data for ABA cross-calibration with ^3He probe.

Dataset	Freq (Hz)	σ_{freq} (Hz)	T_2^* (s)	$\sigma_{T_2^*}$ (s)	Ampl (V)	σ_{Ampl} (V)
1A	177.7317	0.0917	0.373	0.0799	0.0018	0.0001
	177.8314	0.0873	0.5065	0.1401	0.0018	0.0001
	177.9051	0.0886	0.4737	0.1243	0.0018	0.0001
	177.427	0.0988	2.4211	3.6347	0.0014	0.0001
	177.8043	0.0929	0.4688	0.1277	0.0017	0.0001
1A'	177.8144	0.0515	0.5634	0.1022	0.0043	0.0001
	177.6413	0.0525	0.8225	0.2227	0.0039	0.0001
	177.7666	0.0519	0.5048	0.0828	0.0043	0.0001
	177.7446	0.0539	0.4733	0.0755	0.0043	0.0001
	177.704	0.0532	0.4488	0.067	0.0043	0.0001
2A	177.3368	0.0499	0.4505	0.0636	0.0049	0.0002
	177.3734	0.0521	0.4345	0.0617	0.0048	0.0002
	177.4402	0.0496	0.653	0.1326	0.0046	0.0002
	177.3149	0.051	0.568	0.1033	0.0046	0.0002
	177.3494	0.0512	0.5325	0.0912	0.0047	0.0002
2A'	177.5227	0.0942	0.3694	0.0806	0.0018	0.0001
	177.3087	0.0899	0.8061	0.3671	0.0015	0.0001
	177.524	0.0895	1.5129	1.2846	0.0015	0.0001
	177.5521	0.0915	0.3224	0.0597	0.0019	0.0001
	177.3795	0.0947	0.3998	0.095	0.0016	0.0001
3A	177.3277	0.0517	0.6434	0.1344	0.0037	0.0001
	177.4031	0.053	0.4697	0.0734	0.004	0.0001
	177.4696	0.052	0.7397	0.1783	0.0037	0.0001
	177.3532	0.0538	0.4471	0.0675	0.0039	0.0001
	177.4333	0.0512	0.4999	0.0803	0.0039	0.0001
3A'	177.344	0.0555	0.4269	0.0635	0.0037	0.0001
	177.2751	0.0565	0.4381	0.0681	0.0035	0.0001
	177.447	0.0523	0.781	0.2001	0.0034	0.0001
	177.444	0.0539	0.5426	0.0996	0.0035	0.0001
	177.3795	0.0532	0.9771	0.3188	0.0032	0.0001

Table A.3: ^3He data from spherical probe ABBA cross-calibration.

Dataset	Freq (Hz)	σ_{freq} (Hz)	T_2^* (s)	$\sigma_{T_2^*}$ (s)	Ampl (V)	σ_{Ampl} (V)
1B	316.7919	0.5117	0.0501	0.008	0.1385	0.0165
	316.6488	0.5004	0.0504	0.008	0.1375	0.0164
	316.7469	0.5028	0.0486	0.0075	0.1423	0.0168
	316.8624	0.5098	0.0495	0.0078	0.1393	0.0165
	316.7871	0.509	0.0492	0.0077	0.1393	0.0165
1B'	316.7419	0.5084	0.0487	0.0076	0.1423	0.0168
	316.7272	0.5018	0.0506	0.008	0.1363	0.0162
	316.8205	0.5096	0.0493	0.0077	0.1398	0.0166
	316.6187	0.4966	0.0501	0.0079	0.1371	0.0162
	316.7746	0.5097	0.0505	0.0081	0.135	0.0161
2B	316.5969	0.4975	0.049	0.0076	0.1426	0.0168
	316.7842	0.5064	0.0507	0.0081	0.1372	0.0163
	316.6855	0.5028	0.0486	0.0076	0.143	0.0169
	316.6795	0.5056	0.0483	0.0075	0.1437	0.0169
	316.8187	0.4977	0.05	0.0079	0.1388	0.0165
2B'	316.7686	0.5085	0.0502	0.0079	0.1382	0.0164
	316.6088	0.4984	0.049	0.0076	0.1417	0.0167
	316.7152	0.509	0.0504	0.008	0.1373	0.0163
	316.6295	0.4988	0.0499	0.0079	0.139	0.0165
	316.8592	0.5097	0.0489	0.0077	0.1419	0.0168
3B	316.6279	0.5099	0.0497	0.0078	0.1265	0.015
	316.5062	0.5033	0.0501	0.0079	0.1201	0.0143
	316.5597	0.5032	0.0484	0.0075	0.126	0.0149
	316.5896	0.5015	0.0487	0.0076	0.1234	0.0146
	316.6324	0.51	0.0503	0.008	0.1192	0.0142
3B'	316.4443	0.4997	0.0496	0.0078	0.1242	0.0147
	316.5179	0.5009	0.0484	0.0075	0.1291	0.0152
	316.3221	0.5306	0.0492	0.008	0.1234	0.0152
	316.559	0.4979	0.0489	0.0076	0.1271	0.015
	316.5599	0.5041	0.0504	0.008	0.1232	0.0147

Table A.4: Spherical BNL probe data for ABBA cross-calibration with ^3He probe.

Appendix B

Calculations

We provide two calculations in this Appendix. The first is a theoretical calculation to supplement the experimental measurement of the magnetization dependence of the ^3He probe measured frequencies in Section 6.4.1. The second calculation shows that the magnetic field shielding inside a spherical shell is proportional to the square of the shell material susceptibility, which is relevant to the discussion in Section 6.4.2.

B.1 Magnetization Dependence of ^3He Frequencies

As detailed in Section 6.4.1, we observed the magnetization dependence of the ^3He probe frequencies to be -0.12 ± 0.12 Hz when the cell stem pointed orthogonal to the magnetic field and 0.5 ± 0.4 Hz with the stem parallel to the field. While both of these effects are nearly consistent with 0, due to the large uncertainties and the opposite signs of the corrections, we provide a calculation to estimate this effect as a check on the measurement. The magnetic moment due to the polarized ^3He nuclei within the cell stem would be:

$$\mu = Pn\mu_3V, \tag{B.1}$$

where $P \approx 0.4$ is the polarization of the gas, n is the number density at 10 Torr ($n = (10/760)2.68 \times 10^{25} \text{ m}^{-3}$), $\mu_3 = 1 \times 10^{-26} \text{ J/T}$ is the ^3He magnetic moment, and V is the volume of the gas in the stem. We model the stem as a cylinder with an estimated length of 10 mm and radius of 2 mm. Plugging these into B.1, we find the magnetic field created by the polarization of the nuclei in the stem:

$$B = \frac{\mu_0 \mu}{4\pi r^3} \approx 5 \times 10^{-12} \text{ T} \quad (\text{B.2})$$

at a distance $r = 1 \text{ cm}$ away. Hence the perturbation to the field due to the polarization of the gas in the stem would be on the part-per-trillion scale, equivalent to a frequency shift of $\Delta\omega/(2\pi) = (1/2\pi)\gamma_3 B \approx 0.2 \text{ mHz}$. This shift is independent of the stem orientation, indicating that the shifts measured due to this effect must also be consistent with 0 for both stem orientations.

B.2 Magnetic Field Inside a Spherical Shell

Combining Jackson's Section 5.12, Eqs. 5.118 and 5.121, the ratio of magnetic field within a spherical shell of permeable material with susceptibility χ can be written [63]:

$$\frac{B_{in}}{B_0} = \frac{9(1 + \chi)}{(3 + 2\chi)(3 + \chi) - 2\frac{a^2}{b^2}\chi^2}, \quad (\text{B.3})$$

where B_{in} is the field inside the shell, B_0 is the field outside the shell (different from B_{in} due to shielding), χ is the susceptibility of the shell material, and a and b are the inner and outer radii of the shell, respectively. Multiplying out the terms and refactoring, we obtain:

$$\frac{B_{in}}{B_0} = \frac{9 + 9\chi}{9 + 9\chi + 2(1 - \frac{a^2}{b^2})\chi^2} = \frac{1}{1 + \frac{2(1 - \frac{a^2}{b^2})\chi^2}{9(1 + \chi)}} = \left[1 + \frac{2(1 - \frac{a^2}{b^2})\chi^2}{9(1 + \chi)} \right]^{-1} \quad (\text{B.4})$$

Since typical values of χ are small ($\sim 10^{-6}$), we can apply the binomial expansion $(1+x)^m \approx 1+mx$ to find:

$$\frac{B_{in}}{B_0} \approx 1 - \frac{2}{9} \left(1 - \frac{a^2}{b^2}\right) \frac{1}{1+\chi} \chi^2 \quad (\text{B.5})$$

Here, we can apply the binomial expansion again to the $1/(1+\chi)$ term, which yields:

$$\frac{B_{in}}{B_0} \approx 1 - \frac{2}{9} \left(1 - \frac{a^2}{b^2}\right) (1-\chi) \chi^2 = 1 - \frac{2}{9} \left(1 - \frac{a^2}{b^2}\right) \chi^2 + O(\chi^3) \quad (\text{B.6})$$

This shows that the shielding of the magnetic field inside a spherical shell is proportional to the square of the shell susceptibility: χ^2 .

Bibliography

- [1] G. Collier, *Metastability Exchange Optical Pumping (MEOP) of ^3He in situ*. PhD dissertation, Jagiellonian University, 2011.
- [2] T. Blum, A. Denig, I. Logashenko, E. de Rafael, B. L. Roberts, T. Teubner, and G. Venanzoni, *The Muon ($g-2$) Theory Value: Present and Future*, [arXiv:1311.2198](https://arxiv.org/abs/1311.2198).
- [3] J. Schwinger, *On quantum-electrodynamics and the magnetic moment of the electron*, *Phys. Rev.* **73** (Feb, 1948) 416–417.
- [4] T. Aoyama, M. Hayakawa, T. Kinoshita, and M. Nio, *Tenth-order qed contribution to the electron $g-2$ and an improved value of the fine structure constant*, *Phys. Rev. Lett.* **109** (Sep, 2012) 111807.
- [5] A. Czarnecki, B. Krause, and W. J. Marciano, *Electroweak corrections to the muon anomalous magnetic moment*, *Phys. Rev. Lett.* **76** (Apr, 1996) 3267–3270.
- [6] T. Gribouk and A. Czarnecki, *Electroweak interactions and the muon $g - 2$: Bosonic two-loop effects*, *Phys. Rev. D* **72** (Sep, 2005) 053016.
- [7] I. Bars and M. Yoshimura, *Muon magnetic moment in a finite theory of weak and electromagnetic interactions*, *Phys. Rev. D* **6** (Jul, 1972) 374–376.
- [8] K. Fujikawa, B. W. Lee, and A. I. Sanda, *Generalized renormalizable gauge formulation of spontaneously broken gauge theories*, *Phys. Rev. D* **6** (Nov, 1972) 2923–2943.
- [9] W. A. Bardeen, R. Gastmans, and B. E. Lautrup, *Static quantities in Weinberg’s model of weak and electromagnetic interactions*, *Nucl. Phys.* **B46** (1972) 319–331.
- [10] G. Altarelli, N. Cabibbo, and L. Maiani, *The drell-hearn sum rule and the lepton magnetic moment in the weinberg model of weak and electromagnetic interactions*, *Physics Letters B* **40** (1972), no. 3 415 – 419.
- [11] S. Heinemeyer, D. Stckinger, and G. Weiglein, *Electroweak and supersymmetric two-loop corrections to ($g2$)*, *Nuclear Physics B* **699** (2004), no. 1 103 – 123.
- [12] M. Davier, A. Hoecker, B. Malaescu, and Z. Zhang, *Reevaluation of the hadronic contributions to the muon $g2$ and to $\alpha(m_z^2)$* , *The European Physical Journal C* **71** (Jan, 2011) 1515. Erratum-ibid. [13].

- [13] M. Davier, A. Hoecker, B. Malaescu, and Z. Zhang *The European Physical Journal C* **72** (2012), no. 2 1874.
- [14] K. Hagiwara, R. Liao, A. D. Martin, D. Nomura, and T. Teubner *Phys. G: Nucl. Part. Phys.* **38** (2011), no. 085003.
- [15] J. Prades, E. de Rafael, and A. Vainshtein, *The Hadronic Light-by-Light Scattering Contribution to the Muon and Electron Anomalous Magnetic Moments*, *Adv. Ser. Direct. High Energy Phys.* **20** (2009) 303–317, [[arXiv:0901.0306](https://arxiv.org/abs/0901.0306)].
- [16] R. Jackiw and S. Weinberg, *Weak-interaction corrections to the muon magnetic moment and to muonic-atom energy levels*, *Phys. Rev. D* **5** (May, 1972) 2396–2398.
- [17] D. Hanneke, S. Fogwell, and G. Gabrielse, *New measurement of the electron magnetic moment and the fine structure constant*, *Phys. Rev. Lett.* **100** (Mar, 2008) 120801.
- [18] **Muon g-2 Collaboration** Collaboration, G. W. Bennett, B. Bousquet, H. N. Brown, G. Bunce, R. M. Carey, P. Cushman, G. T. Danby, P. T. Debevec, M. Deile, H. Deng, W. Deninger, S. K. Dhawan, V. P. Druzhinin, L. Duong, E. Efstathiadis, F. J. M. Farley, G. V. Fedotovitch, S. Giron, F. E. Gray, D. Grigoriev, M. Grosse-Perdekamp, A. Grossmann, M. F. Hare, D. W. Hertzog, X. Huang, V. W. Hughes, M. Iwasaki, K. Jungmann, D. Kawall, M. Kawamura, B. I. Khazin, J. Kindem, F. Krienen, I. Kronkvist, A. Lam, R. Larsen, Y. Y. Lee, I. Logashenko, R. McNabb, W. Meng, J. Mi, J. P. Miller, Y. Mizumachi, W. M. Morse, D. Nikas, C. J. G. Onderwater, Y. Orlov, C. S. Özben, J. M. Paley, Q. Peng, C. C. Polly, J. Pretz, R. Prigl, G. zu Puttlitz, T. Qian, S. I. Redin, O. Rind, B. L. Roberts, N. Ryskulov, S. Sedykh, Y. K. Semertzidis, P. Shagin, Y. M. Shatunov, E. P. Sichtermann, E. Solodov, M. Sossong, A. Steinmetz, L. R. Sulak, C. Timmermans, A. Trofimov, D. Urner, P. von Walter, D. Warburton, D. Winn, A. Yamamoto, and D. Zimmerman, *Final report of the e821 muon anomalous magnetic moment measurement at bnl*, *Phys. Rev. D* **73** (Apr, 2006) 072003.
- [19] J. P. Miller, E. de Rafael, and B. L. Roberts, *Muon ($g-2$): Experiment and theory*, *Rept. Prog. Phys.* **70** (2007) 795, [[hep-ph/0703049](https://arxiv.org/abs/hep-ph/0703049)].
- [20] G. Charpak, F. J. M. Farley, R. L. Garwin, T. Muller, J. C. Sens, V. L. Telegdi, and A. Zichichi, *Measurement of the anomalous magnetic moment of the muon*, *Phys. Rev. Lett.* **6** (Feb, 1961) 128–132.
- [21] G. Charpak, F. Farley, R. Garwin, T. Muller, J. Sens, and A. Zichichi, *A new measurement of the anomalous magnetic moment of the muon*, *Physics Letters* **1** (1962), no. 1 16 – 20.
- [22] J. Bailey, W. Bartl, G. V. Bochmann, R. Brown, F. Farley, H. Jstlein, E. Picasso, and R. Williams, *Precision measurement of the anomalous magnetic moment of the muon*, *Physics Letters B* **28** (1968), no. 4 287 – 290.

- [23] J. Bailey, K. Borer, F. Combley, H. Drumm, C. Eck, F. Farley, J. Field, W. Flegel, P. Hattersley, F. Krienen, F. Lange, G. Lebe, E. McMillan, G. Petrucci, E. Picasso, O. Rnolfsson, W. von Rden, R. Williams, and S. Wojcicki, *Final report on the cern muon storage ring including the anomalous magnetic moment and the electric dipole moment of the muon, and a direct test of relativistic time dilation*, *Nuclear Physics B* **150** (1979) 1 – 75.
- [24] **Muon g-2** Collaboration, J. Grange et al., *Muon (g-2) Technical Design Report*, [arXiv:1501.06858](https://arxiv.org/abs/1501.06858).
- [25] P. J. Mohr, D. B. Newell, and B. N. Taylor, *Codata recommended values of the fundamental physical constants: 2014**, *Journal of Physical and Chemical Reference Data* **45** (2016), no. 043102.
- [26] V. L. Williams and V. W. Hughes, *Magnetic moment and hfs anomaly for he^3* , *Physical Review* **185** (1969), no. 4 1251–1255.
- [27] J. L. Flowers, B. W. Petley, and M. G. Richards, *A measurement of the nuclear magnetic moment of the helium-3 atom in terms of that of the proton*, *Metrologia* **30** (jan, 1993) 75–87.
- [28] Y. Neronov and N. Seregin, *High precision evaluation of the magnetic moment of the helion*, *Journal of Experimental and Theoretical Physics* **115** (2012), no. 5 777781.
- [29] M. A. Bouchiat, T. R. Carver, and C. M. Varnum, *Nuclear polarization in he^3 gas induced by optical pumping and dipolar exchange*, *Phys. Rev. Lett.* **5** (Oct, 1960) 373–375.
- [30] R. L. Gamblin and T. R. Carver, *Polarization and relaxation processes in he^3 gas*, *Phys. Rev.* **138** (May, 1965) A946–A960.
- [31] F. Colegrove, L. Schearer, and G. Walters, *Polarization of 3He gas by Optical Pumping*, *Phys. Rev.* **132** (1963) 2561–2572.
- [32] W. Fitzsimmons, L. Tankersly, and G. Walters., *Nature of Surface-Induced Nuclear-Spin Relaxation of Gaseous 3He* , *Phys. Rev.* **179** (1969) 156–165.
- [33] P. Nacher, M. Leduc, J. Trenec, and F. Laloe, *Polarisation nucléaire de 3He gazeux par pompage optique laser*, *J. Physique Lett.* **43** (1982) 525–529.
- [34] P. Nacher and M. Leduc, *Optical Pumping in 3He with a Laser*, *Journal de Physique* **46** (1985) 2057–2073.
- [35] E. Courtade, F. Marion, P. Nacher, G. Tastevin, K. Kiersnowski, and T. Dohnalik, *Magnetic field effects on 1083 nm atomic line of helium*, *Eur. Phys. J. D* **21** (2002) 25–55.
- [36] M. Pavlovic and Laloe, *Etude d'une nouvelle methode permettant d'orienter, par pompage optique, des niveaux atomiques excites. application a la mesure de la structure hyperne de niveaux 1d de 3he* , *Journal de Physique* **31** (2-3) (1970) 173–194.

- [37] J. Maxwell, C. Epstein, and R. Milner, *Liquid crystal polarimetry for metastability exchange optical pumping of ^3He* , *Nuclear Instruments and Methods in Physics Research Section A Accelerators Spectrometers Detectors and Associated Equipment* **764** (215-219) 2014.
- [38] W. Lorenzon, T. Gentile, H. Gao, and R. McKeown, *NMR calibration of optical measurement of nuclear polarization in ^3He* , *Phys. Rev. A* **47** (1) (1993) 468–479.
- [39] M. Abboud, A. Sinatra, X. Maitre, G. Tastevin, and P. Nacher, *High nuclear polarization of ^3He at low and high pressure by metastability exchange optical pumping at 1.5 tesla*, *Europhys. Lett.* **68** (4) (2004) 480–486.
- [40] M. Abboud, A. Sinatra, G. Tastevin, P. Nacher, and X. Maitre, *Metastability Exchange Optical Pumping of Helium-3 at High Pressures and 1.5 T: Comparison of two Optical Pumping Transitions*, *Laser Physics, MAIK Nauka/Interperiodica* **15** (4) (2005) .475–479.
- [41] A. Abragam, *Principles of Nuclear Magnetism (International Series of Monographs on Physics)*. Oxford University Press, New York, 1961.
- [42] C. P. Slichter, *Principles of Magnetic Resonance (Springer Series in Solid-State Sciences) (v.1)*. Springer-Verlag, Berlin, Heidelberg, New York, 1996.
- [43] L. D. Schearer and G. K. Walters, *Nuclear spin-lattice relaxation in the presence of magnetic-field gradients*, *Phys. Rev.* **139** (Aug, 1965) A1398–A1402.
- [44] G. D. Cates, S. R. Schaefer, and W. Happer, *Relaxation of spins due to field inhomogeneities in gaseous samples at low magnetic fields and low pressures*, *Phys. Rev. A* **37** (Apr, 1988) 2877–2885.
- [45] D. D. McGregor, *Transverse relaxation of spin-polarized ^3He gas due to a magnetic field gradient*, *Phys. Rev. A* **41** (Mar, 1990) 2631–2635.
- [46] A. Kramida, Yu. Ralchenko, J. Reader, and NIST ASD Team. NIST Atomic Spectra Database (ver. 5.6.1), [Online]. Available: <https://physics.nist.gov/asd>. National Institute of Standards and Technology, Gaithersburg, MD., 2018.
- [47] N. Sachdeva et al., *A new measurement of the permanent electric dipole moment of ^{129}Xe using ^3He comagnetometry and SQUID detection*, [arXiv:1902.02864](https://arxiv.org/abs/1902.02864).
- [48] ENI RF power amplifier, Bell Electronics, 1150 Raymond Avenue SW Renton, Washington 98057-3125 U.S.A.
<https://www.bellnw.com/manufacture/ENI/240L.htm>.
- [49] Keopsys, 2 rue Paul Sabatier, Lannion, France 22300
<https://www.keopsys.com/portfolio/cw-ytterbium-fiber-laser-giga-series/>.
- [50] HighFinesse GmbH, Wöhrdstraße 4 72072 Tübingen, Germany,
<https://www.highfinesse.com/en/wavelengthmeter/>.

- [51] SOLIDWORKS, 175 Wyman Street Waltham, MA 02451
<https://www.solidworks.com/>.
- [52] D. M. Ginsberg and M. J. Melchner, *Optimum geometry of saddle shaped coils for generating a uniform magnetic field*, *Review of Scientific Instruments* **41** (1970) 122.
- [53] D. D. Wheeler and M. S. Conradi, *Practical exercises for learning to construct nmr/mri probe circuits*, *Concepts in Magnetic Resonance Part A* **40A** (2012), no. 1 1–13, [<https://onlinelibrary.wiley.com/doi/pdf/10.1002/cmr.a.21221>].
- [54] HUBER+SUHNER, Tumbelenstrasse 20 8330 Pfäffikon ZH
<https://www.hubersuhner.com/en/products/radio-frequency/cables/flexible-low-loss-rf-cables/spuma>.
- [55] X. Fei, V. Hughes, and R. Prigl, *Precision measurement of the magnetic field in terms of the free-proton nmr frequency*, *Nuclear Instruments and Methods in Physics Research Section A: Accelerators, Spectrometers, Detectors and Associated Equipment* **394** (1997), no. 3 349 – 356.
- [56] A. Rudziski, M. Puchalski, and K. Pachucki, *Relativistic, qed, and nuclear mass effects in the magnetic shielding of ^3He* , *The Journal of Chemical Physics* **130** (2009), no. 24 244102, [<https://doi.org/10.1063/1.3159674>].
- [57] Y. I. Neronov and N. N. Seregin, *Precision determination of the difference in shielding by protons in water and hydrogen and an estimate of the absolute shielding by protons in water*, *Metrologia* **51** (jan, 2014) 54–60.
- [58] J. F. Schenck, *The role of magnetic susceptibility in magnetic resonance imaging: Mri magnetic compatibility of the first and second kinds*, *Medical Physics* **23** (1996), no. 6 815–850, [<https://aapm.onlinelibrary.wiley.com/doi/pdf/10.1118/1.597854>].
- [59] J. S. Philo and W. M. Fairbank, *Temperature dependence of the diamagnetism of water*, *The Journal of Chemical Physics* **72** (1980), no. 8 4429–4433.
- [60] E. P. Day, *Equation for the magnetic susceptibility of water*, *The Journal of Chemical Physics* **72** (1980), no. 8 4434–4436.
- [61] PT1000 Temperature Sensor. Datasheet available at: <https://www.datasheets360.com/part/detail/s17624pfyt40a/1024551774622713768/>.
- [62] B. Petley and R. Donaldson, *The temperature dependence of the diamagnetic shielding correction for proton NMR in water*, *Metrologia* **20** (1984), no. 3 81–83.
- [63] J. D. Jackson, *Classical Electrodynamics*. John Wiley Sons, New York, 2nd ed., 1975.
- [64] A. Nikiel, P. Blümmler, W. Heil, M. Hehn, S. Karpuk, A. Maul, E. Otten, L. M. Schreiber, and M. Terekhov, *Ultrasensitive ^3He magnetometer for measurements of high magnetic fields*, *The European Physical Journal D* **68** (Nov, 2014) 330.

- [65] A. Schneider, A. Mooser, A. Rischka, K. Blaum, S. Ulmer, and J. Walz, *A novel penning-trap design for the high-precision measurement of the ${}^3\text{He}^2+$ nuclear magnetic moment*, *Annalen der Physik* **531** (2019), no. 5 1800485, [<https://onlinelibrary.wiley.com/doi/pdf/10.1002/andp.201800485>].
- [66] A. Mooser, A. Rischka, A. Schneider, K. Blaum, S. Ulmer, and J. Walz, *A new experiment for the measurement of the g -factors of ${}^3\text{He}$ and ${}^3\text{He}^2$* , *Journal of Physics: Conference Series* **1138** (nov, 2018) 012004.